Light transport
in anisotropically scattering
and absorbing media

Ozan Akdemir

LIGHT TRANSPORT IN ANISOTROPICALLY SCATTERING AND ABSORBING MEDIA

Ozan Akdemir

LIGHT TRANSPORT IN ANISOTROPICALLY SCATTERING AND ABSORBING MEDIA

DISSERTATION

To obtain
the degree of doctor at the University of Twente,
on the authority of the rector magnificus,
prof. dr. ir. A. Veldkamp,
on account of the decision of the Doctorate Board,
to be publicly defended
on Thursday 14 September 2023 at 14:45 hours

by

Ozan Akdemir

Born on the 27th of February, 1994
in Osmangazi, Turkey.

This dissertation has been approved by: :

Promotor
prof. dr. W.L. Vos
Co-promotor
prof. dr. A. Lagendijk

GRADUATION COMMITTEE:

Chairman/secretary:	prof. dr. J.L. Herek (University of Twente)
Promotor:	prof. dr. W.L. Vos (University of Twente)
Co-promotor:	prof. dr. A. Lagendijk (University of Twente)
Committee Members:	prof. dr. A. Kienle (Universität Ulm)
	prof. dr. ir. B.J. Geurts (University of Twente)
	prof. dr. J.F. de Boer (Vrije Universiteit Amsterdam)
	dr. ir. S. Salama (University of Twente)
	dr. M.C.J.M. Vissenberg (Signify Eindhoven)

To my beloved late grandmother, Ayşe.

Contents

1 Introduction

1.1 Light

Light is essential for our existence as it allows us to perceive and interact with our environment. Without the interaction between light and matter, our planet would be an uninhabitable mass of ice and rock. Solar radiation warms the land and the oceans and provides energy for photosynthetic organisms to produce oxygen. Through optical perception, many organisms find nutrients, evade dangers, communicate with each other, and navigate their surroundings. In addition to its biological significance, light has played a pivotal role in human civilization and culture. The manipulation of light has led to significant technological advancements, including the invention of light bulbs and fiber-optic communication. To understand light transport through various media, it is crucial to study light scattering, which provides valuable insights into the optical properties of materials and how to shape the materials in a way to control the propagation of light.

1.2 Scattering of light

Let us consider plane waves of light propagating through a medium. If the medium is homogeneous, light travels without any disturbance with a speed equal to the well-known speed of light divided by the refractive index c/n. However, if there are spatial variations in the refractive index n, the direction and amplitude of light will change at the interface of these inhomogeneities. This occurs when two homogeneous media with different refractive indices have an interface (*e.g.,* refraction of light at the air-water interface) as well as when a medium contains inclusions of another material with a different refractive index n_2. Examples of the latter case are photonic scattering media, such as paint, foam, and tissue, where the incident waves are scattered and absorbed by inhomogeneities referred to as *scatterers* [1–6]. The scatterers are characterized by their scattering cross-section σ_{scat}, which is the hypothetical cross-sectional area used to normalize the total scattered intensity of light by the scatterer. In other words, the total energy scattered in all directions by the scatterer is equal to the energy incident on the area σ_{scat} [7, 8]. In this thesis, the light that is scattered in this manner is called *diffuse* light.
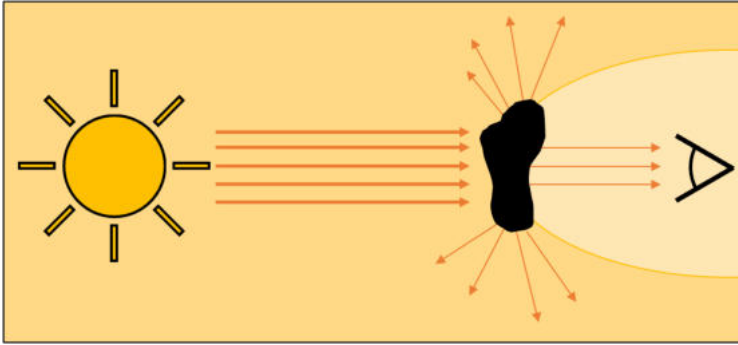
Figure 1.1: Illustration of extinction of light. An object scatters and absorbs an incoming beam of light, hence removes part of the energy from the beam that reaches the observer.

When light interacts with a scatterer, a portion of the incident electromagnetic energy can be converted through absorption into another form of energy, such as thermal or chemical energy. The absorbed energy is expressed by the absorption cross-section σ_{abs} of the scatterer, which is defined as the area in which the total absorbed intensity is normalized to the incident energy on it [7, 8].

Scattering and absorption remove electromagnetic energy from the incident beam. This attenuation is called *extinction*, and is illustrated in Fig. 1.1. Extinction can be measured by observing the source *after* light has interacted with the scatterer. Hence, the extinction cross-section σ_{ext} is the sum of scattering and absorption cross-sections:

$$\sigma_{\text{ext}} = \sigma_{\text{scat}} + \sigma_{\text{abs}}. \tag{1.1}$$

In reality, the intensity alone does not provide a complete characterization of either the incident or the scattered light. Additional information regarding *polarization* and *phase* is necessary for the complete picture of electromagnetic waves [7]. While acknowledging the importance of polarization and phase, we do not discuss them explicitly in this thesis, and place our main focus on energy densities and intensities.

1.2.1 Single scattering of light

Single scattering refers to the situation where one scattering event occurs with one scatterer[1]. There are three categories of single scattering, which are primarily dependent on the size of the scatterer: Rayleigh scattering, Mie scattering, and geometrical scattering. Rayleigh scattering describes the regime where the size of the scatterer with radius r is much smaller than the wavelength of the incident light λ: $r \ll \lambda$ [10]. In this regime, light scatters *isotropically*, that is, uniformly in every direction as shown in Fig. 1.2(a). The blue color of the sky is a popular

---

[1]The general interaction of light with one scatterer is described by the t-matrix which includes all possible scattering events, see [2, 9]

example of Rayleigh scattering, where blue light is scattered more strongly than other visible wavelengths by atmospheric molecules and aerosols. The scattering cross-section in Rayleigh scattering depends on the inverse fourth power of the wavelength of light $\sigma_{\text{scat}} \propto \frac{1}{\lambda^4}$ [11]. Geometrical scattering describes the converse case, in which the size of the scatterer is much larger than λ ($r \gg \lambda$), as with macroscopic objects like a windowpane or a bottle. In this case, reflection and refraction phenomena are adequate to explain the transport of light.
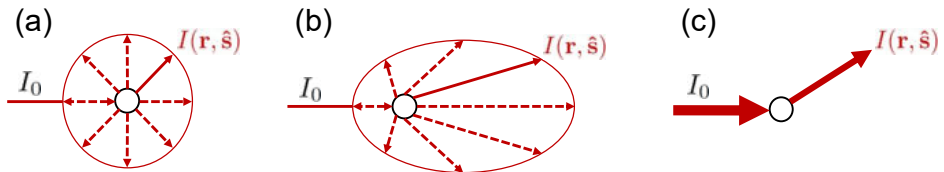
Figure 1.2: (a) An isotropic scatterer that scatters in all directions with equal probability. (b) An anisotropic scatterer that scatters more in the forward direction. (c) An absorbing scatterer, where the loss of intensity is depicted as thinner arrow after the scattering event. In (a,b) the solid arrows are incident and scattered ($\hat{\mathbf{s}}$) directions, the dashed arrows are other possible scattering directions, and the arrow lengths indicate the probability to scatter into that direction. In (a, b, c), the centers of the scattering spheres are at $\mathbf{r}$, I_0 is the incident intensity and $I(\mathbf{r}, \hat{\mathbf{s}})$ is the scattered intensity.

When the size of the scatterer is comparable to the wavelength ($r \approx \lambda$), it is considered to be in the Mie scattering regime, called after Gustav Mie [7, 12]. Mie scattering provides an excellent description of the scattering process if the scatterer is a sphere or a long cylinder. Mie scattering approaches Rayleigh and geometrical scattering in the long- and short-wavelength limits, respectively. A scatterer with a spherical shape and a size approximately equal to the wavelength of light is called a Mie sphere. Mie spheres exhibit resonances at specific wavelengths where the scattering cross-section is much larger than the physical cross-section: $\sigma_{\text{scat}} \gg \pi r^2$ [9]. The scattering by Mie spheres is generally more pronounced in the forward direction, as shown in Fig. 1.2(b), resulting in an anisotropic scattering pattern. In this thesis, the term *anisotropic scatterer* or *anisotropic sample* means the direction of light scattering is anisotropic, and it does not necessarily refer to the *shape* of the scatterer, unless stated otherwise (as in chapter 6).

Cross sections describe the scattering from individual scatterers, while mean free paths characterize a collection of scatterers [2, 3, 9, 13]. We will refer to the region with the collection of scatterers as the *sample*. The scattering mean free path ℓ_{scat} is the average distance between two consecutive scattering events, and in the independent scattering approximation it is equal to

$$\ell_{\text{scat}} = \frac{1}{\rho \sigma_{\text{scat}}}, \tag{1.2}$$

where ρ represents the density of scatterers. For samples that contain absorbing scatterers, the decay of incident light intensity is determined by the extinction

mean free path ℓ_{ext} that includes both scattering and absorption, and is equal to

$$\ell_{\text{ext}} = (\frac{1}{\ell_{\text{scat}}} + \frac{1}{\ell_{\text{abs}}})^{-1}, \tag{1.3}$$

where ℓ_{abs} is the absorption mean free path, equal to

$$\ell_{\text{abs}} = \frac{1}{\rho \sigma_{\text{abs}}}, \tag{1.4}$$

that represents the average distance light travels before being absorbed, down to a fraction $1/e$ ($\approx 36\%$).

1.2.2 Multiple scattering of light

As long as the size L of the sample is smaller than ℓ_{scat}, the single scattering regime holds. Multiple scattering occurs when the scattering mean free path is smaller than the sample size ($\ell_{\text{scat}} < L$) and light undergoes multiple changes in direction within the sample. At each scattering event, the direction of light changes according to the phase function of the scatterers, which determines the probability of the scattering direction. Details about the phase function are provided in Chapter 4. By ignoring the wave nature of light, the propagation inside a multiple scattering sample is described as a random walk with an average step size of ℓ_{scat}. The direction of light is fully randomized after a number of steps. The length scale that describes the distance over which the information of the initial direction of light is lost, is the transport mean free path ℓ_{tr} [2, 14–17], given by

$$\ell_{\text{tr}} = \frac{\ell_{\text{scat}}}{1 - \langle \cos \theta \rangle}, \tag{1.5}$$

where $\langle \cos \theta \rangle$ is the average cosine of the scattered angle. In the Rayleigh regime, the scattering is isotropic, $\langle \cos \theta \rangle = 0$, and $\ell_{\text{tr}} = \ell_{\text{scat}}$. In case the scattering is mostly in the forward direction, many scattering events are needed before the direction of light becomes completely randomized. In the forward scattering case we have $0 < \langle \cos \theta \rangle < 1$ and $\ell_{\text{tr}} > \ell_{\text{scat}}$. On the other hand, in the backscattering case the direction of scattering is mainly backwards, with $-1 < \langle \cos \theta \rangle < 0$ and $\ell_{\text{tr}} < \ell_{\text{scat}}$. Another important regime is where the transport mean free path is much smaller than the sample size $\ell_{\text{tr}} \ll L$ and even of the order or smaller than the wavelength, which is significant for light localization studies[2] [19–21].

Multiple scattering is an important optical phenomenon that affects our perception of the world around us. For instance, a glass of water is transparent, but water droplets form clouds in the sky that appear white due to multiple scattering. The color of white paint is also a result of multiple scattering caused by TiO_2 or similar nanoparticles. Biological tissue, fog, milk, and interstellar clouds are other examples of media in which multiple scattering is prominent.

An important property of light that diffuses in a photonic scattering medium is the energy density. In medical applications like photodynamic therapy (PDT), it

---

[2]Strong localization of light occurs when $\ell_{tr} \leq \lambda$ [18]

is necessary to understand the position-dependent energy density distribution inside tissue that is illuminated by a light source [22–24]. This knowledge is crucial to activate the photosensitizing agents that are placed in the tissue beforehand, to achieve the targeted treatment [25].

The understanding of light transport in multiple scattering media is also essential in the field of satellite observations of water bodies [26, 27]. This type of scattering media contain absorbing and anisotropic scatterers. Investigations of optical properties of the water bodies through satellite observations help reveal the biochemical composition of water, monitor water quality, and assess the impacts of climate change and pollution on natural water resources [28–30]. Multiple scattering is also relevant in various industrial applications, such as diffuser glasses and phosphor plates used in white light emitting diodes (LEDs).

1.3 Light scattering in the industrial regime

Understanding the transport of light in photonic scattering media is crucial for many application areas, such as atmospheric and climate sciences [31–34], oceanography [35, 36], biophysics [37–40], powder technology [16, 41, 42], printing [43], and solid-state lighting [44–47]. In the context of industrial applications that are at the basis of the FFSO program that funded this thesis, it is necessary to balance two competing properties. First, the transmission and the reflection of light should be optimized, particularly for applications where quick measurements are required, such as in wafer metrology. The maximum transmission requirement favors the use of thin samples. Conversely, light should be sufficiently diffused, particularly for even illumination of a detector, such as in an earth-observing satellite, or in lighting where the underlying LED components should not be visible to the consumer. For the lighting industry, the sample thickness L must be at least one transport mean free path ($L \geq \ell_{tr}$). These requirements are simultaneously achieved when the sample thickness is on the order of the transport mean free path ($L \approx \ell_{tr}$), a situation we refer to as scattering in the *industrial regime*. Fig. 1.3 shows an illustration of thin, thick and industrial regimes. The balance of both high transmission and diffuse light may be achieved by samples that contain anisotropic scatterers, since the length scales relate as $\ell_{scat} < L < \ell_{tr}$, hence the output is more directional than the isotropic case.

In the *thick* limit ($L \ll \ell_{abs}$, $L \gg \ell_{tr}$) of non-absorbing media, diffusion theory provides an accurate description of light transport in photonic scattering media [1, 9], notably of the energy density [48]. In principle, light transmission through thick samples can be increased by wavefront shaping [49, 50]. However, including a digital micromirror device (DMD) or a spatial light modulator (SLM) is not very practical in most industrial applications. In the *thin* limit ($L \ll \ell_{tr}$), geometrical optics accurately describes light transport and reflection. The *intermediate industrial* regime is of utmost importance for industrial applications, however, it is also the least understood as it falls into neither the thick nor the thin limit, and therefore requires further exploration. Furthermore, anisotropic

scatterers offer many control opportunities and deserve extra attention in the industrial regime.
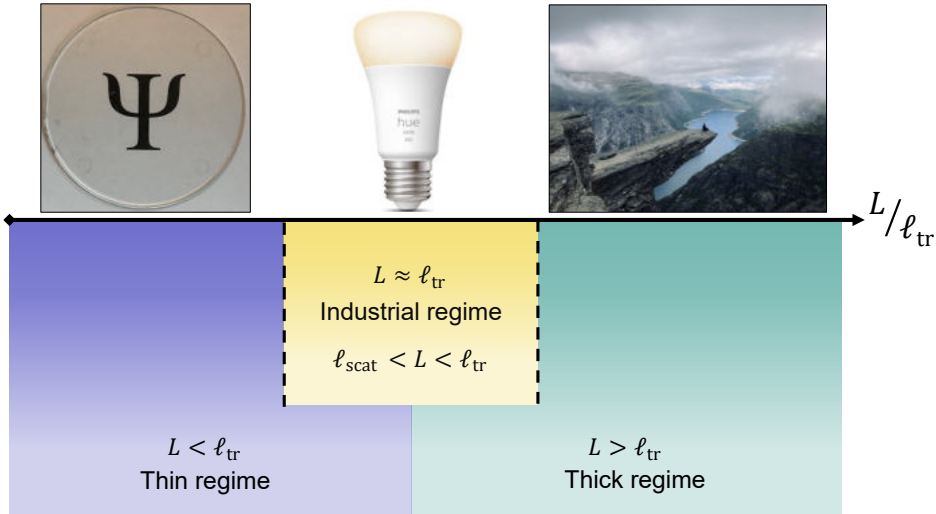
Figure 1.3: Illustration of scattering regimes as a function of the ratio of sample thickness L and the transport mean free path ℓ_{tr}. The figure showcases three examples: A transparent polymer slab, representing a sample in the thin regime and featuring a physicists' favorite symbol behind it. A Philips hue white LED bulb by Signify with a phosphor layer, representing a sample that contains a scattering medium in the industrial regime. Thick clouds on top of Trolltunga, Norway, representing scattering media in the thick regime.

The energy density is crucial to understand how light is converted in a white LED. White LEDs typically rely on a combination of a blue LED [51], and a phosphor layer that absorbs part of the blue light and re-emits in green, yellow, and red light to achieve the desired white light [44, 45, 52–54]. A good understanding of light transport in scattering media with absorbing scatterers is essential to control the properties of the phosphor layers. A nice example of these conversion layers is the so-called Lumiramic developed by Lumileds, which is based on phosphor in a ceramic material that improves thermal management [46].

The combination of a blue LED, phosphor, and possibly other scatterers is not only intended to convert colors but also to produce an even distribution of white light for outgoing directions. In many optical systems like car lighting and smart street lighting, it is essential to control the escape distribution to produce a narrower yet still diffuse cone, instead of a Lambertian, to reach a higher system efficacy and improved beam quality. A promising method to achieve this is to introduce additional anisotropic scatterers inside the phosphor layers. Therefore, understanding the light transport and energy density distribution within photonic scattering media, which contains absorbing and anisotropic scatterers, is extremely relevant for industrial applications.

1.4 Transport theory

Transport theory describes the propagation of waves in scattering media, notably in a widely-used realistic situation like a slab in three dimensions (3D), as shown in Fig. 1.4. The theory describes the transfer of intensity and neglects interference effects including diffraction [1]. For all practical purposes the transport theory is rigorous and only in exceptional cases such as the situations of very strong elastic scattering and Anderson localization of light where interference predominates, the transport shows features beyond the predictions of transport theory [2]. Even though transport theory neglects interference effects, it contains information about correlation of fields [55] and it is used to improve the understanding of interference effects, such as wavefront shaping inside scattering media [50].
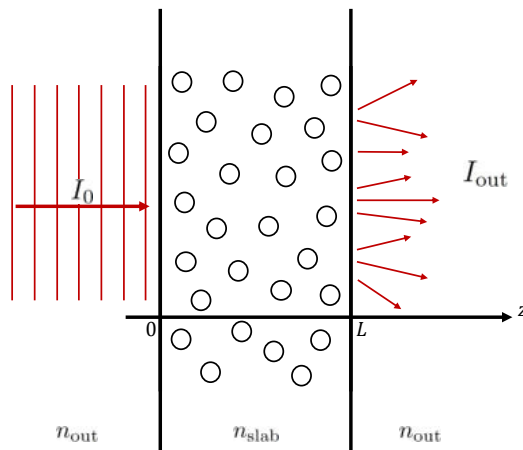
Figure 1.4: Incident plane waves with intensity I_0 are scattered by scatterers (spheres) inside a slab and leave as scattered waves with total intensity I_{out}. The refractive indices of the slab and of the medium outside are n_{slab} and n_{out}, respectively. The reflections from interfaces and the back-scattered light are neglected from the illustration.

The basic differential equation used in transport theory is the radiative transfer equation (RTE), which is equivalent to Boltzmann's equation used in the kinetic theory of gases and neutron transport [1, 56, 57]. The most fundamental quantity is the specific intensity $I(\mathbf{r}, \hat{\mathbf{s}})$ that describes the average power flux density at position $\mathbf{r}$ in a given direction $\hat{\mathbf{s}}$ within a unit solid angle and a unit frequency band [1]. Due to its dependency on both the position $\mathbf{r}$ and the direction $\hat{\mathbf{s}}$, it is challenging to solve $I(\mathbf{r}, \hat{\mathbf{s}})$ directly.

The most popular method to solve the RTE for light is the Monte Carlo simulation of light transport [58–66], a statistical method that converges to the exact solution of the RTE. To obtain a high accuracy, however, this method comes with the cost of extremely long computation times [67] and high computational power requirements with concomitant high energy consumption.

The complexity of transport theory and the slow Monte Carlo simulations have

stimulated the development of analytical approximations to the RTE [68–74]. Despite impressive advances made by graphics processing unit (GPU) based Monte Carlo simulations in terms of speed [63, 64], analytical methods are still significantly faster. Moreover, in certain configurations, such as the slab geometry, the results of these analytical approximations match the accuracy of simulations.

A widely used analytical approximation to the RTE is the P_N approximation (see subsection 4.2.1 for full solution for a slab geometry), where the dependence on both variables is separated [57] by expanding the specific intensity $I(\mathbf{r}, \hat{\mathbf{s}})$ in products of complete sets on the domains of $\mathbf{r}$ and $\hat{\mathbf{s}}$

$$I(\mathbf{r}, \hat{\mathbf{s}}) = \sum_{l=0}^{N} \sum_{m=-l}^{l} \psi_l^m(\mathbf{r}) Y_l^m(\hat{\mathbf{s}}). \tag{1.6}$$

Here, $\psi_l^m(\mathbf{r})$ are the spatial components, $Y_l^m(\hat{\mathbf{s}})$ are the directional components taken as the Laplace spherical harmonics [75, 76], and N is the order of the approximation that determines the number of terms in Eq. (1.6). The analytical P_N approximations are mostly used for simple sample geometries such as a slab and a sphere and their accuracies depend notably on (i) the order N of the approximation, (ii) on the optical properties of the medium and (iii) the scattering phase function used in the approximation. The specific intensity $I(\mathbf{r}, \hat{\mathbf{s}})$ and the scattering phase function are discussed in detail in Chapter 4. As N approaches infinity, the P_N approximation yields exact solutions. In realistic cases, such as a 3D slab, the order is rarely higher than $N = 3$ as the mathematical complexity increases rapidly with increasing N. [3] The higher order terms have little information to add for the isotropic scattering case, however, they could become significant in the anisotropic samples. Analytical solution approaches that enable higher orders ($N > 3$) exist, but generally require the numerical determination of eigenvalues and eigenvectors [78–80]. In this thesis, we focus on the first- and third-order P_N approximation and a correction to the third-order for the forward scattering case that improves the accuracy significantly.

1.5 Outline of the thesis

In this thesis, we study the light transport through photonic scattering media, specifically the position dependent energy density, by using the transport theory and experimental observations. We specifically focus on samples that consist of anisotropically scattering and absorbing scatterers, as common approximations to the radiative transfer equation fail for these samples and one is thus interested in the possible description in these regimes.

As a unification of this thesis, let us briefly consider various dimensionalities. Let us consider a general sample to have lengths (L_x, L_y, L_z) in the (x, y, z) dimensions. Let us assume that the light scattering may be described by mean

---

[3]Odd positive integers are chosen for N since odd order approximations are known to be more accurate than even orders, as in the even order approximations the angular integrands are discontinuous [77].

free paths (ℓ_x, ℓ_y, ℓ_z) that may differ depending on whether light propagates in the (x, y, z) directions. Most part of this thesis concerns the 3D situation where the mean free paths are isotropic $(\ell_x = \ell_y = \ell_z)$ typical for samples with isotropic internal structure like spherical scatterers. Moreover the samples are "industrial", hence mean free paths are comparable to the sample dimensions. We mostly study slab samples where one dimension is much less than the other two $\{L_x, L_y\} \gg L_z$, and where the light transport is in the thin dimension z, hence the transport appears to be effectively 1D (see chapters 3-5)

A second main study in this thesis concerns samples that are structurally anisotropic, namely consisting of parallel micropillars. In this class of samples the transport is in essence two-dimensional (2D) and $\{\ell_x, \ell_z\} \ll \ell_y$. Moreover the sample dimensions are such that the non-scattering direction is finite $L_y \ll \{L_x, L_z\}$, hence the transport is not strictly 2D and therefore called quasi-2D.

Chapter 2 summarizes the relevant parts of the theory of integrating spheres to our experiments. The substitution error and how double-beam measurements can reduce systematic the errors is discussed. Experimental measurements are presented to compare the single-beam and double-beam measurements, and at most 2% systematic error is found.

In Chapter 3 we study the P_1, P_3, and $P_3 + \delta E(4)$ approximations to the radiative transfer equation, to model the light transport in photonic scattering media. We defined the unphysical ranges of these analytical approximations in the parameter space albedo[4] a, anisotropy g, optical thickness b, and index contrast Δn^2. We provide the relative error maps of the approximations by comparing them to the Monte Carlo simulations of light transport, in a complete range of a and g parameters and for a realistically chosen b and Δn^2. The results presented in this chapter provide a guideline for the applicability of the P_1, P_3, and $P_3 + \delta E(4)$ approximations, to interpret experiments on light transport in photonic scattering slabs.

Chapter 4 lays out the theoretical background for Chapters 3 and 5. The key parameters in transport theory are explained and the radiative transfer equation for a slab is derived and solved using the analytical P_1, P_3, and $P_3 + \delta E(4)$ approximations. Consideration of homogeneous layers with a different refractive index, between the air-slab interface, is added to the boundary conditions and the effect of internal reflections to the source intensity is explained. Furthermore, several alternative phase functions to the Henyey-Greenstein phase function are discussed.

In Chapter 5 we present a comprehensive analysis of the experimental measurements of position-dependent energy fluence rate, which is proportional to the energy density, of samples that contain anisotropically scattering and absorbing spherical scatterers. Preparation of samples and the experimental setup are explained in detail. The experimental observations are compared to the results of the analytical approximations to the solution of the radiative transfer equation, which are discussed in Chapters 3 and 4, and the Monte Carlo simulations. A detailed account of the experimental limitations, which prevent an absolute measurement and an exact match with the models, is provided.

---

[4]In this thesis we refer to *single scattering albedo* as *albedo*, for convenience.

Chapter 6 presents the position-dependent energy density measurements on quasi-2D samples consisting of randomly positioned circular cylinders, etched on a silicon wafer. The energy density is probed by measuring the out-of-plane scattering from the top of the samples. The sample fabrication and the experimental setup is explained in detail. Initial experimental results from the setup are presented and discussed.

Finally, Chapter 7 summarizes the results of this thesis and provides an outlook to improve the experiments and the possible utilization of the results for future applications.

2 Measurements with integrating spheres

2.1 Introduction

Integrating spheres are widely used tools for the measurement of optical properties of materials and of light sources. In particular, such spheres are used to collect optical information that is angle-integrated or wave vector integrated. Therefore, the inner surfaces of these spheres are coated with a highly reflective and diffusive material, which ensures uniform distribution and collection of light. Integrating spheres have applications in various fields, such as measurements of light output and spectral characteristics of light emitting diodes (LEDs) [17, 47, 81, 82], quantum yield measurements of quantum dots [83, 84], characterization of optical properties of biological materials such as coral colonies [85], algal cell suspensions [86, 87], and food samples [88–91].

This chapter summarizes the theory of integrating spheres relevant to the experiments conducted in this thesis following the reference [92]. The chapter discusses the use of integrating spheres to conduct total transmission and total reflection measurements, to measure the optical properties of photonic scattering samples. Finally, it discusses the double-beam total transmission measurements to correct for systematic errors and compares them with single-beam measurements obtained by our setup.

2.2 Integrating sphere theory

Light incident on a diffuse surface creates a virtual light source by reflection. The light emanating from the surface is described by its intensity, or radiance, that is the flux density per unit projected solid angle

$$I = \frac{F_\mathrm{i} R_\mathrm{s}}{\pi A_\mathrm{s}} \quad \left[\frac{\mathrm{W}}{\mathrm{m^2 sr}}\right] \tag{2.1}$$

where F_i is the input flux, R_s is the reflectance from the surface, A_s is the illuminated area, and the total projected solid angle from the surface is assumed to be π. The wavelength and sample dependencies of the quantities discussed in this chapter are not explicitly written in equations for visual convenience.

For an integrating sphere, the equation to describe intensity at the inner surface of the sphere I_s must consider both multiple surface reflections and losses through the port openings. The total flux incident on the internal sphere surface is higher than the input flux F_i due to multiple reflections inside the sphere.
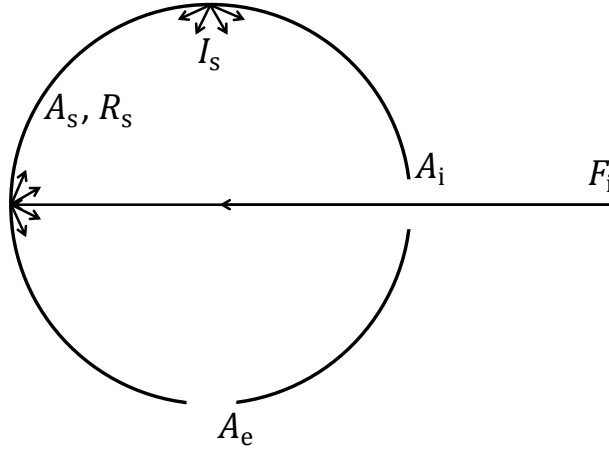
Figure 2.1: Schematic cross-section of an integrating sphere with two ports: an input port with area A_i, and an exit port with area A_e. The sphere has internal area A_s and inner wall reflectance R_s. The input flux is F_i and I_s is the intensity emanating from sphere surface due to many reflections of F_i inside the sphere.

Consider an integrating sphere, shown in Fig. 2.1, with an input port area A_i and an exit port A_e. The internal sphere surface intensity I_s is equal to

$$
\begin{aligned}
I_\mathrm{s} &= \frac{F_\mathrm{i}}{\pi A_\mathrm{s}} \times \frac{R_\mathrm{s}}{1 - R_\mathrm{s}(1 - f_\mathrm{port})} \\
&= \frac{F_\mathrm{i}}{\pi A_\mathrm{s}} \times M
\end{aligned}
\tag{2.2}
$$

where M is called the sphere multiplier, A_s is the area of the inner sphere, R_s is the reflectance of the inner walls, and f_port is the total port fraction defined as

$$
f_\mathrm{port} \equiv \frac{A_\mathrm{ports}}{A_\mathrm{s}},
\tag{2.3}
$$

where A_ports is the sum of all port areas[1], that is equal to

$$
A_\mathrm{ports} = A_\mathrm{i} + A_\mathrm{e},
\tag{2.4}
$$

for the sphere shown in Fig. 2.1. Note that the I_s decrease as A_s increases at constant input F_i.

A handy rule of thumb for integrating spheres is

$$
\begin{aligned}
0.94 &< R_\mathrm{s} < 0.99 \\
0.02 &< f_\mathrm{port} < 0.05
\end{aligned}
\tag{2.5}
$$

which defines a range for the inner wall reflectance R_s and states that no more than 5% of the sphere surface area A_s should be consumed by port openings for accurate measurements.

---

[1] A integrating sphere may have multiple ports, *e.g.*, ours has 4

Eqn. (2.2) is specific to the case where F_i is incident on the inner sphere wall through an open port, the wall reflectance is uniform and the reflectance of all port areas is zero. A more general expression of the sphere multiplier M is

$$M = \frac{R_0}{1 - R_s(1 - \sum_{i=0}^{n} f_i) - \sum_{i=0}^{n} R_i f_i},$$ (2.6)

where R_0 is the initial reflectance for the incident flux, R_i is the reflectance of port opening i, and f_i is the fractional port area of port i. For simplicity, the average reflectance $\bar{R}$ is defined as

$$\bar{R} \equiv R_s(1 - \sum_{i=0}^{n} f_i) - \sum_{i=0}^{n} R_i f_i.$$ (2.7)

Hence the sphere multiplier becomes

$$M = \frac{R_0}{1 - \bar{R}}.$$ (2.8)

There are various detection methods of measurements with integrating sphere, such as using a lens to focus the diffuse output on a photodetector or directly mounting a photodetector on the exit port of the integrating sphere. Here, we consider the situation where a fiber is attached to the exit port of the integrating sphere, as illustrated in Fig. 2.2, and where the other end of the fiber connected to a detector. The flux collected by the fiber F_{fiber} is equal to

$$F_{\text{fiber}} = I_s A_f \pi (NA)^2 (1 - R_f), \;\; [W]$$ (2.9)

where NA is the numerical aperture of the fiber, $\pi(NA)^2$ is the projected solid angle that is viewed by the fiber core, and R_f is the specular reflectance of the fiber surface that reflects part of the light back into the sphere. The fiber surface has an area A_f that depends on the core radius r_c as $A_f = \pi r_c^2$. In measurements using integrating spheres, it is crucial that the detected flux F_{fiber} does not include a portion of the incident flux F_i that is reflected only once by the sphere surface, which leads to a false response. This is prevented by the use of *baffles*, which are coated with the same diffuse material that covers the sphere walls. The purpose of the baffle is to block the detector's view of the incident flux that has not undergone at least two reflections from the sphere surface. Fig. 2.2 shows an example of an integrating sphere with a baffle. The positioning, shape and number of baffles are optimized for the specific design and requirements of the integrating sphere, as well as the detection method employed in measurements.

While in theory, the surface intensity I_s is uniform everywhere in the integrating sphere surface area, in practice that is not the case. Since different parts of the sphere wall can have different reflections, it is crucial to align the incident beam correctly before starting measurements. Fig. 2.3 shows the cross-section of an integrating sphere where a light beam is sent in through Port 1, and exits through Port 2, where the initial reflection would take place if the port would be closed. A good way to ensure reproducibility of results in case of realigning the
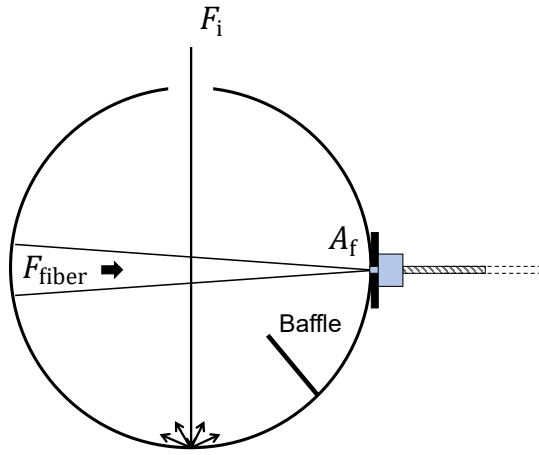
Figure 2.2: Schematic cross-section of an integrating sphere with 2 ports (entrance and exit ports), a baffle, and a fiberoptic cable attached to the exit port with fiber surface area A_f. F_i is the incident flux on the integrating sphere surface, and F_{fiber} is the flux that is collected by the fiber.

incident beam in the setup, is to make sure the beam enters through the center of Port 1, and leaves the sphere through the center of Port 2. Furthermore, the baffles are generally positioned with consideration of this central positioning of the incident beam. Having a small beam diameter compared to the port diameters also helps to reduce this systematic error.

An experiment was done to observe the effect on the detected flux F_{fiber} of the incident beam position at the entry port of an integrating sphere (Opsira uku240).
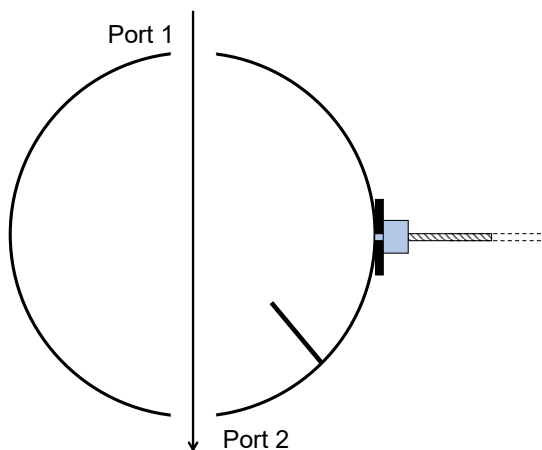

Figure 2.3: Schematic cross-section of an integrating sphere with three ports, of which Port 1 and Port 2 are open and the third has a fiber attached to it. An incident light beam enters through the center of Port 1, and exits through the center of Port 2.
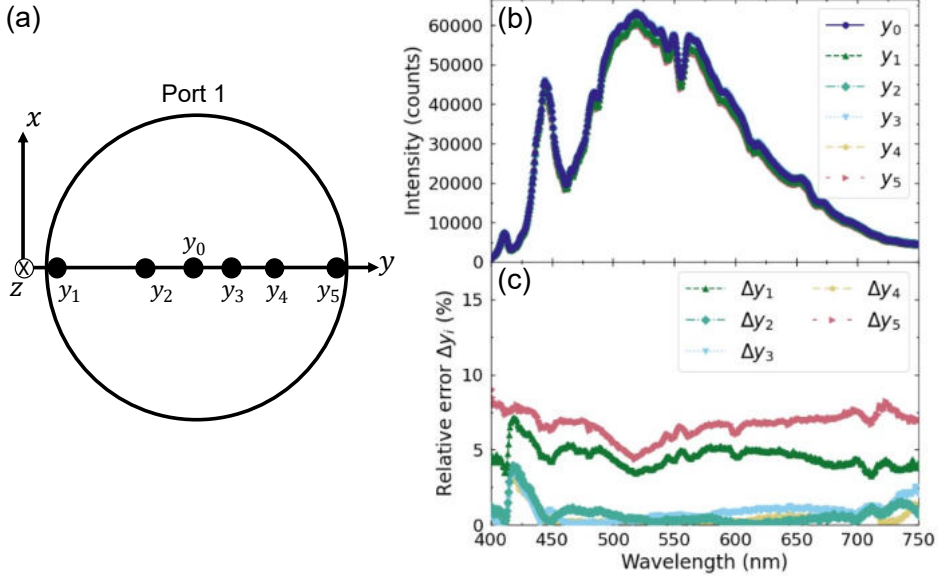
Figure 2.4: (a) Schematic of incident light beams positioned on Port 1 (entry port). y_0 is the center of the port opening, and y_1, y_2, y_3, y_4 and y_5 represent other tested positions within the port diameter $d_{\text{port}} = 20$ mm. The incident beam travels in the z-direction. (b) Measured spectra of incoming broadband beams that passed through the positions shown in (a). (c) Relative errors Δy_i of measured spectra at varied entry positions compared to the spectrum measured for central entry position y_0.

We used a broadband supercontinuum light source (Fianium SC450, 2W) with a beam diameter set to $d_{\text{beam}} = 2$ mm, and as a detector a spectrometer (Avantes Starline, AvaSpec-2048L) coupled to the integrating sphere via a fiberoptic cable. The incident beam entry position is varied along one axis, and the spectrum of the transmitted light is measured as a function of the entry position. Fig. 2.4(a) shows a representation of the positions tested in the experiment. Fig. 2.4(b) displays the measured spectra at different entry positions, and Fig. 2.4(c) shows the relative error Δy_i of measured spectra for each tested entry position with respect to the spectrum taken for the central position y_0, where Δy_i is defined as

$$\Delta y_i \equiv \sqrt{\frac{(y_i - y_0)^2}{y_0^2}}. \tag{2.10}$$

From Fig. 2.4(c), it is observed that the systematic relative error is between $4.6\% < \Delta y_{1,5} < 6.7\%$, for the entry positions that are ≈ 9 mm away from the central position y_0. For the entry positions that are within < 5 mm distance from y_0, the error is $\Delta y_{2,3,4} < 1\%$. In addition, it is observed that the fluctuation of wavelength dependency is low. It is important to note that this experiment is conducted along only one axis, and testing various positions at other axes could result in further variations.
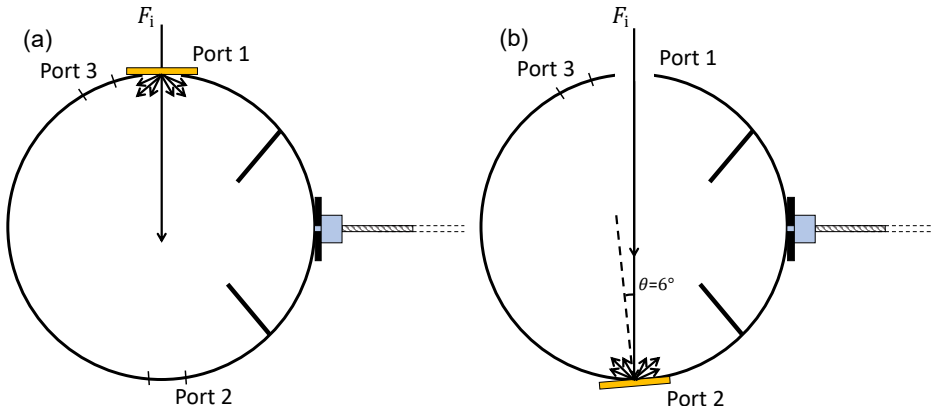
Figure 2.5: Schematic of the Opsira uku240 integrating sphere used in this thesis. (a) Total transmission and (b) total reflection configurations of the integrating sphere. The yellow rectangle represents the sample, and it is attached to (a) Port 1 for the total transmission and (b) Port 2 the total reflection configurations. There is a 6° angle between the incident beam direction and the normal to the sample surface in (b), and Port 3 is closed to measure the total transmission and the total reflection of the sample.

2.3 Total transmission and reflection measurements

Integrating spheres are commonly used for diffuse or total transmission and total reflection measurements, aimed at extracting various optical properties of samples, including spectral characteristics [47] and mean free paths [17]. The specific integrating sphere (Opsira, uku240) utilized in the experiments conducted in this thesis has four ports and employs two baffles, as shown in Fig. 2.5.

Fig. 2.5(a) shows the configuration of the total transmission measurements, where the sample is positioned at Port 1 of the integrating sphere and the total transmission TT of the sample is defined as

$$TT \equiv \frac{F_t}{F_i}, \tag{2.11}$$

where F_t is the measured total transmitted flux through the sample, and F_i is the measured incident flux without a sample[2]. This two-step measurement is often called single-beam measurement [93, 94] and it does not consider the systematic substitution error, which is discussed at the end of this section. The configuration of total reflection measurements is shown in Fig. 2.5(b), where the sample is placed at Port 2 of the integrating sphere. There is a 6° angle between the incident beam direction and the normal to the sample surface in reflectivity. The total reflection TR of the sample is defined as

$$TR \equiv \frac{F_r}{F_i}, \tag{2.12}$$

---

[2]The subtraction of dark counts is not included in eqn. (2.11) and other equations in this chapter, for simplicity. If necessary, dark counts are subtracted from all measured flux.

where F_r is the total reflected flux from the sample. The 6° angle between the incident beam direction and the normal to the sample surface in Fig. 2.5(b) serves to remove or capture the specular reflection from the sample surface by opening or closing Port 3, respectively.

A systematic error present in all integrating spheres, called the *substitution error* [93, 95], arises from alterations in the average reflectance of the sphere walls due to the presence of samples attached to the ports. This error is primarily dependent on the port fraction f_{port} of the integrating sphere, as well as the reflectance of the samples and the reflectance of the integrating sphere walls. This error is often small and neglected in practice, and approximations using lookup tables are commonly used to estimate its impact [96]. Reference [97] discusses experimental procedures to measure the substitution error in reflection measurements, using an additional reference port in the integrating sphere. The introduction of the additional reference port is not possible in our experiments. Due to the small port fraction $f_{port} < 0.7\%$ of our integrating sphere and the low reflectance $TR \leq 15\%$ of the samples used in the experiments of chapter 5, we expect a small substitution error $\Delta TR_{subs} \leq 2\%$ [92]. References [92, 96] provide additional, guidelines to further correct this error, if needed.

2.3.1 Double-beam total transmission measurements

Double-beam measurements are measurement with integrating spheres that include additional steps to correct the substitution errors [92, 96] that are present in single-beam measurements (see Fig. 2.5). Let us first examine the substitution error in single-beam measurements by taking the ratio of *detected* transmitted flux F_t^{det} and *detected* incident flux F_i^{det} using eqns. (2.2), (2.6) and (2.9) for the configuration in Fig. 2.5(a).

$$\frac{F_t^{det}}{F_i^{det}} = \frac{\frac{F_t}{\pi A_s} M_t A_f \pi (NA)^2 (1 - R_f)}{\frac{F_i}{\pi A_s} M_i A_f \pi (NA)^2 (1 - R_f)},$$

$$= \frac{F_t}{F_i} \frac{M_t}{M_i}, \tag{2.13}$$

$$= TT \frac{M_t}{M_i}.$$

Here, the sphere multiplier factor for the detected transmitted flux M_t is equal to

$$M_t = \frac{R_0}{1 - R_w(1 - f_f - f_1) - R_f f_f - R_1 f_1}, \tag{2.14}$$

where f_f is the fractional port area of the fiber port, f_1 is the fractional port area of the entry port (Port 1 in Fig. 2.5(a)), R_f is the reflectance at the fiber surface, and R_1 is the reflectance at the entry port from the surface of the sample. The sphere multiplier factor for the detected incident flux M_i is equal to

$$M_i = \frac{R_0}{1 - R_w(1 - f_f - f_1) - R_f f_f}. \tag{2.15}$$

Eqns. (2.14) and (2.15) show that M_t and M_i do not cancel out, therefore, the ratio of F_t^{det} and F_i^{det} is not equal to the total transmission of the sample, and should thus be corrected.
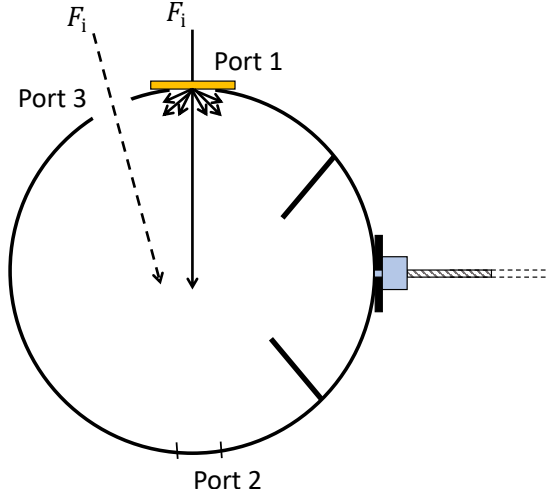
Figure 2.6: Schematic of double-beam total transmission measurement configuration of the integrating sphere. Port 3 is open during the measurements. Incident beam enters from Port 1 or Port 3 depending on the step of the measurement series, and Port 2 is always closed. The yellow rectangle represent the sample that is attached to Port 1.

The setup configuration for double-beam total transmission measurements is shown in Fig. 2.6. Port 3 is always open during double-beam measurements and incident flux F_i enters the integrating sphere either from Port 1 or Port 3, depending on the step of the measurement series. The incident beam is aligned such that the initial reflection is at the same spot on the sphere surface regardless of the port the beam enters the sphere. It should be noted that the initial reflectance from the sphere wall when the beam enters from Port 1 (R_0) is inevitably different from the initial reflectance from the sphere wall when the beam enters from Port 3 (R_0'). The double-beam method has a series of 4 steps to measure total transmission of the samples:

1. The sample is attached to Port 1, the beam is incident on the sample and enters the sphere from Port 1, to measure the transmitted flux F_t^{db}

$$F_t^{db} = \frac{F_t}{\pi A_s} M_t^{db} A_f \pi (NA)^2 (1 - R_f), \qquad (2.16)$$

where the multiplier factor M_t^{db} is equal to

$$M_t^{db} = \frac{R_0}{1 - R_w(1 - f_f - f_1 - f_2) - R_f f_f - R_1 f_1}. \qquad (2.17)$$

2. The sample is attached to Port 1 and the beam enters the sphere from Port 3, to measure the calibration flux $F_{\text{cal}}^{\text{db}}$

$$F_{\text{cal}}^{\text{db}} = \frac{F_{\text{i}}}{\pi A_{\text{s}}} M_{\text{cal}}^{\text{db}} A_{\text{f}} \pi (NA)^2 (1 - R_{\text{f}}), \tag{2.18}$$

where the multiplier factor $M_{\text{cal}}^{\text{db}}$ is equal to

$$M_{\text{cal}}^{\text{db}} = \frac{R_0'}{1 - R_{\text{w}}(1 - f_{\text{f}} - f_1 - f_2) - R_{\text{f}} f_{\text{f}} - R_1 f_1}. \tag{2.19}$$

3. Nothing is attached to Port 1 and the beam enters the sphere from Port 1, to measure the incident flux F_{i}^{db}

$$F_{\text{i}}^{\text{db}} = \frac{F_{\text{i}}}{\pi A_{\text{s}}} M_{\text{i}}^{\text{db}} A_{\text{f}} \pi (NA)^2 (1 - R_{\text{f}}), \tag{2.20}$$

where the multiplier factor M_{i}^{db} is equal to

$$M_{\text{i}}^{\text{db}} = \frac{R_0}{1 - R_{\text{w}}(1 - f_{\text{f}} - f_1 - f_2) - R_{\text{f}} f_{\text{f}}}. \tag{2.21}$$

4. Nothing is attached to Port 1 and the beam enters the sphere from Port 3, to measure the correction flux $F_{\text{cr}}^{\text{db}}$

$$F_{\text{cr}}^{\text{db}} = \frac{F_{\text{i}}}{\pi A_{\text{s}}} M_{\text{cr}}^{\text{db}} A_{\text{f}} \pi (NA)^2 (1 - R_{\text{f}}), \tag{2.22}$$

where the multiplier factor $M_{\text{cr}}^{\text{db}}$ is equal to

$$M_{\text{cr}}^{\text{db}} = \frac{R_0'}{1 - R_{\text{w}}(1 - f_{\text{f}} - f_1 - f_2) - R_{\text{f}} f_{\text{f}}}. \tag{2.23}$$

The total transmission TT is now defined to be

$$TT \equiv \frac{F_{\text{t}}^{\text{db}}}{F_{\text{i}}^{\text{db}}} \frac{F_{\text{cr}}^{\text{db}}}{F_{\text{cal}}^{\text{db}}} = \frac{F_{\text{t}}}{F_{\text{i}}}, \tag{2.24}$$

where the multiplying factors cancel out, and the effect of sample reflection is eliminated.

The comparison of single-beam and double-beam total transmission measurements with the integrating sphere used in our experiments are given in Fig. 2.7. The samples used in this comparison are polymer slabs with different concentrations of TiO_2 scatterers [17]. The sample labelled "0.0w.t.%TiO_2" is a blank polymer without any TiO_2 scatterers. The total transmission of the samples decrease with increasing scatterer density, as expected. The troughs observed around 400 and 675nm correspond to unknown polymer absorption. The comparison between the double-beam and the single-beam measurements reveals substitution errors $\Delta TT_{\text{subs}} \leq 2\%$, for all samples and wavelengths within the visible

range. Such small $\Delta TT_{\mathrm{subs}}$ are expected in our setup, as the integrating sphere is designed to have a small port fraction ($f_{\mathrm{port}} < 0.7\%$).
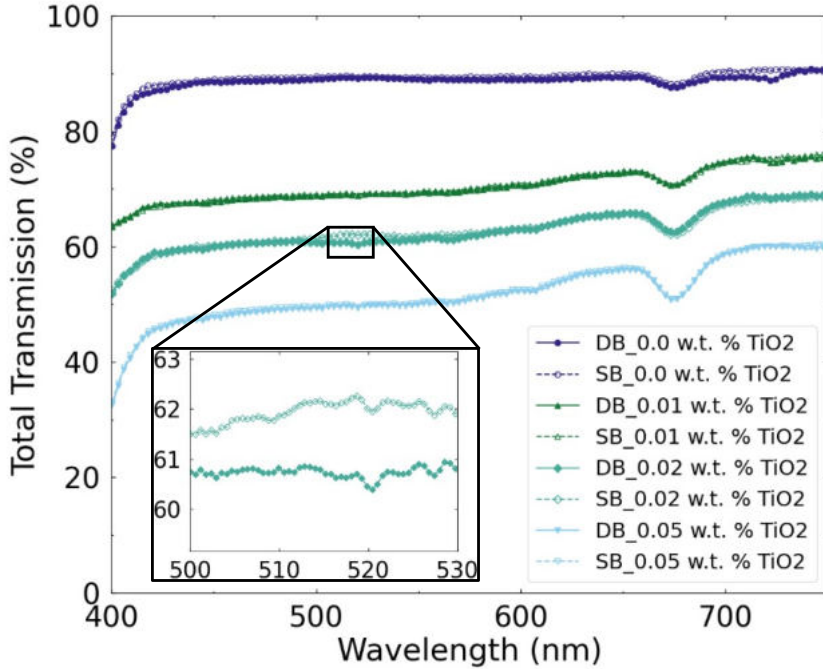

Figure 2.7: Total transmission measurements of polymer samples with different weight concentrations of TiO_2 scatterers. Double-beam (DB) measurements are represented by filled markers connected by solid lines, and single-beam (SB) measurements are represented by hollow markers connected by dashed lines. The inset highlights the small differences between measurement methods. Marker shape and color represent samples with different weighted concentrations of scatterers, as labelled in the legend.

2.4 Summary

This chapter provides an overview of the theory of integrating spheres that is relevant to the experiments conducted in this thesis. The substitution error is discussed, and the use of double-beam total transmission measurements to eliminate this error is explained. Furthermore, a comparison is presented between single-beam and double-beam total transmission measurements of scattering samples using our experimental setup. It is observed that the substitution errors, shown in Fig. 2.7, are less than 2% due to the small port fraction of the integrating sphere employed in the experiments. Since this error is much smaller than other sources of variations in our experiments, we decide to neglect it and proceed with single-beam measurements in the subsequent experiments using the same integrating sphere in this thesis.

3 Breakdown of transport models in photonic scattering slabs

3.1 Introduction

The radiative transfer equation (RTE) models the transport of light inside photonic scattering samples such as paint, foam and tissue. Analytic approximations to solve the RTE fail for samples with strong absorption and dominant anisotropic scattering and predict unphysical negative energy densities and the diffuse flux in the wrong direction. In this chapter, we thoroughly validate three popular approximations to the RTE for a slab, namely the P_1 approximation, the P_3 approximation, and a popular modification to P_3 that corrects the forward scattering in the approximation [99]. The first-order analytical approximation P_1 to transport theory is the diffusion theory [1], which is widely used to extract transport parameters from opaque media with isotropic scatterers (see Fig. 1.2(a)) and with negligible absorption. For a slab shown in Fig. 1.4, this opaque configuration amounts to the thickness L being much larger than the transport mean free path ℓ_{tr} and much smaller than the absorption mean free path ℓ_{abs}:

$$\ell_{tr} \ll L \ll \ell_{abs}. \tag{3.1}$$

If the scattering is dominantly in the forward direction, ℓ_{tr} increases (see Fig. 1.2(b)), and ℓ_{abs} decreases if the scatterers have significant absorption (see Fig. 1.2(c)). Meretska *et al.* defined a physically more informative validity range using the three-parameter space (a,g,b) spanned by the albedo a, the anisotropy g, and the optical thickness b [100]. A practically relevant parameter space also requires consideration of the internal reflection at the slab boundaries [101, 102], hence we add the refractive index contrast Δn^2 as a 4th parameter.

$$\Delta n^2 \equiv \frac{n_{slab}^2 - n_{out}^2}{2n_{slab}^2}. \tag{3.2}$$

Here, n_{slab} and n_{out} are the refractive index of the medium inside the slab that surrounds the scatterers and the index of the medium outside the slab (typically free space), respectively. Once the $(a, g, b, \Delta n^2)$ parameter set is known, the solution of the P_N approximation is fully determined.

In some parts of the $(a, g, b, \Delta n^2)$ parameter space, the P_N approximations predict unphysical behavior, such as a *negative energy density*. We call these regions *unphysical ranges*. In this chapter, we map the unphysical ranges and

---

The work presented in this chapter is published in reference [98]

the relative errors of three popular approximations to the RTE, namely, the P_1, the P_3, and the $P_3 + \delta E(4)$ approximations. The P_3 approximation is a widely used higher-order approximation to RTE [47, 82, 103, 104], especially popular in biophysics [37, 69, 71]. The $P_3 + \delta E(4)$ approximation uses a modified phase function within the P_3 approximation to increase the accuracy of the forward scattering region [37, 69, 105] (see section 4.3.3). The unphysical ranges of each approximation are found by scanning the $(a, g, b, \Delta n^2)$ parameter space and looking for the regions where the validity conditions (3.3) are violated. In addition, the relative error maps are obtained by comparing the P_N approximations to extensive Monte Carlo simulations. Our simulation code is based on the work of Prahl *et al.* [58], with the addition of multiple internal reflection similar to a Fabry-Pérot cavity [106], where only the multiply reflected intensities are considered but no interference, see Ref. [8], chapter 2.
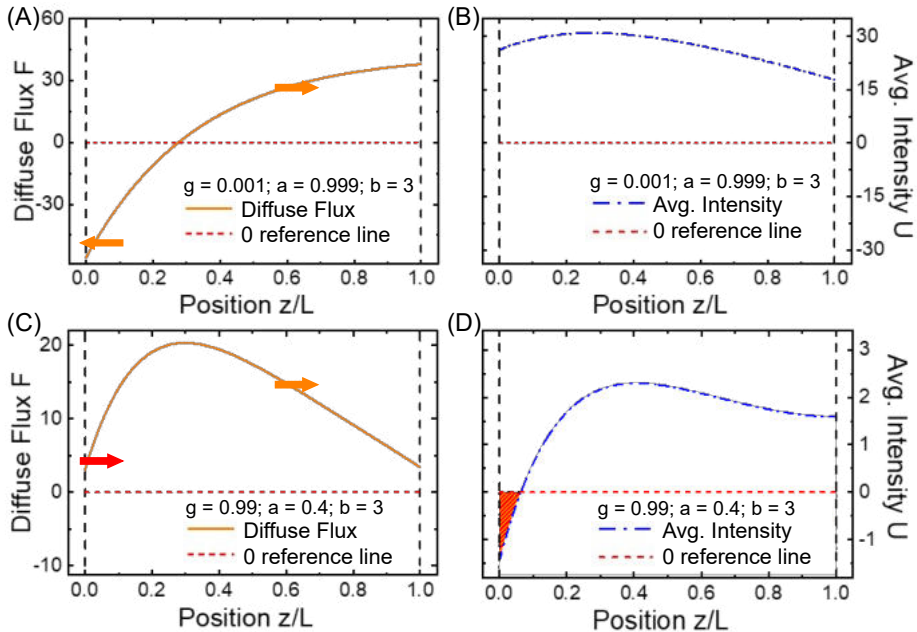
Figure 3.1: Examples of physical and unphysical results. (A) Diffuse flux F and (B) average intensity U computed with the P_1 or diffusion approximation for isotropic ($g = 0.001$) scattering with little absorption ($a = 0.999$) are physically sensible. (C) Diffuse flux F and (D) average intensity U using P_1 for anisotropic scattering ($g = 0.99$) and strong absorption ($a = 0.4$). In (C) the red arrow on the left boundary indicates the *unphysical* direction of F and in (D) the *unphysical* negative average intensity U is highlighted with red hatches. Black dashed vertical lines represent the boundaries of the slab with optical thickness $b = 3$ and $\Delta n^2 = 0.245$ typical of a polymer slab in air. The direction of F is given by the orange arrows, and the red dashed horizontal line indicates the zero level.

3.2 Unphysical ranges of P_N approximations

An example of an unphysical result of the P_1 approximation is shown in Fig. 3.1(C,D). In Fig. 3.1(D) the diffusion theory predicts an unphysical negative energy density. The diffuse flux F given in Fig. 3.1(C) is unphysical, since the theory predicts erroneously an *incident* diffuse flux F, whereas a reflected flux opposite to the incident direction of light is required at the incident boundary (left boundary in Fig. 3.1).

3.2.1 Unphysical ranges of the P_1, P_3 and $P_3 + \delta E(4)$ approximations

The physical validity conditions of the P_N approximation are expressed mathematically as [100]:

$$
\begin{aligned}
&U(z) \geq 0 \ \forall \ z \in [0, L], \\
&F(z) < 0 \ \text{at} \ z = 0, \\
&F(z) > 0 \ \text{at} \ z = L.
\end{aligned}
\tag{3.3}
$$

Here $U(z)$ is the average intensity that is directly proportional to the energy density $u(z)$ [1];

$$
U(z) \equiv \frac{c}{4\pi} u(z),
\tag{3.4}
$$

where c is the speed of light. The unphysical ranges are found by checking whether the approximations violate one or more of the conditions given in equation (3.3), for each set of parameters $(a, g, b, \Delta n^2)$. The unphysical regions given in Figs. 3.2, 3.3 and 3.4 cover all possible albedos and anisotropies in photonic scattering slabs from backscattering to forward scattering. For all figures with anisotropy-albedo maps, the limits of anisotropy are $g = -0.999999$ and $g = 0.999999$, and extreme absorption limit is $a = 0.000001$. The perfect anisotropy ($g = 1$ and $g = -1$) and complete absorption ($a = 0$) cases are not discussed here, as they are unphysical [107, 108] and thus samples with such properties can not be realized.

Fig. 3.2 shows the unphysical ranges when the optical thickness and refractive index contrast are fixed ($b = 3$; $\Delta n^2 = 0.245$, *e.g.*, a polymer slab in air). The P_3 approximation, being the higher-order approximation, is generally believed to be an improvement on the P_1 approximation [37]. Hence we expect a shrinking of the unphysical range in going from P_1 to P_N. In Fig. 3.2(b), however, the expected improvement is not observed. It is even more remarkable that parts of the physical regions of the P_1 approximation are unphysical for the P_3. As expected, the $P_3 + \delta E(4)$ approximation is entirely physical for the forward scattering region. In the dominant backscattering range around $g = -0.5$ and below, however, the approximation is primarily unphysical even without absorption, which is also reasonable since the $P_3 + \delta E(4)$ approximation is a modification to correct only the forward direction.
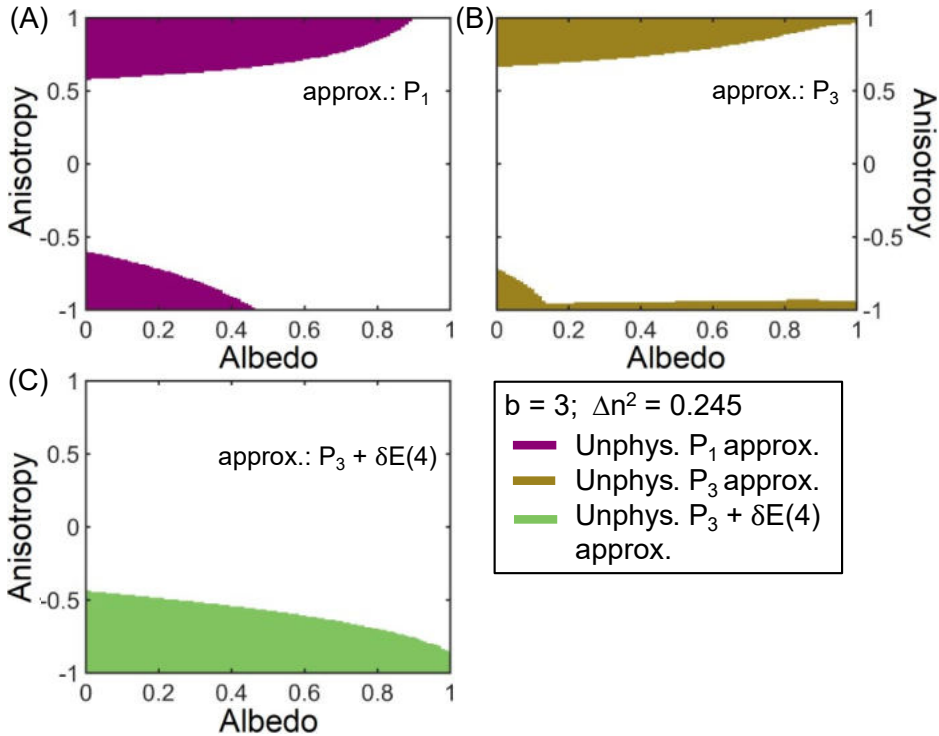
Figure 3.2: Unphysical ranges of (A) P_1 approximation, (B) P_3 approximation and (C) $P_3 + \delta E(4)$ approximation. Fixed optical thickness $b = 3$ and refractive index contrast $\Delta n^2 = 0.245$ (*e.g.*, polymer slab in air). In this figure and the following ones, the extreme anisotropy limits are $g = 0.999999$ and $g = -0.999999$, as the exact forward scattering $g = 1$ and exact backscattering $g = -1$ cases are unphysical.

The effects of varying the thickness b and the index contrast Δn^2 are presented in Fig. 3.3 and Fig. 3.4, respectively. Increasing the optical thickness from $b = 1$ to $b = 5$ (see Fig. 3.3) has more effect on the unphysical range of the P_1 approximation compared to the other methods. A clear increase is seen in the unphysical range of the P_1 approximation, from strong to weak absorption regions, and some minor expansion towards the isotropic regions with increased thickness b. For the P_3 approximation, increasing b also results in an expansion of the unphysical range, however, the change is smaller than in the P_1 approximation. In contrast, the unphysical range of the $P_3 + \delta E(4)$ approximation remains almost the same for all thicknesses.
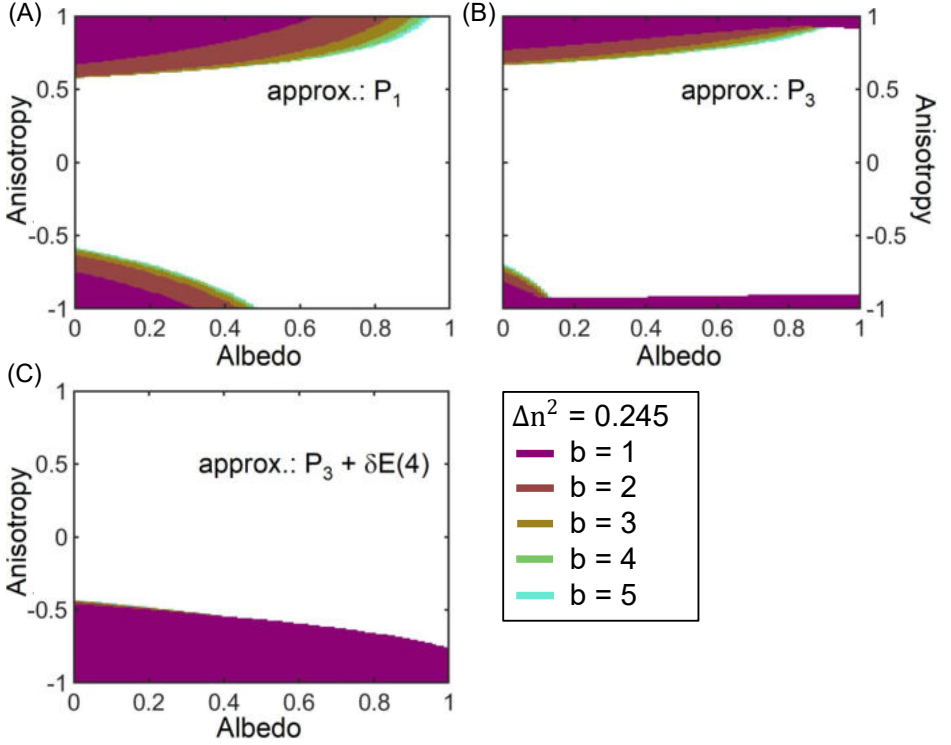
Figure 3.3: Unphysical ranges of (A) P_1 approximation, (B) P_3 approximation and (C) $P_3 + \delta E(4)$ approximation, for various optical thicknesses and for fixed refractive index contrast $\Delta n^2 = 0.245$ (*e.g.*, polymer slab in air).

In Fig. 3.4 we show the unphysical ranges when the index contrast is varied up to 0.375 at a fixed optical thickness ($b = 3$). As Δn^2 increases, the unphysical range of the P_1 approximation shrinks towards the non-absorbing region. Interestingly, for the P_3 approximation, the $\Delta n^2 = 0$ (index matching) situation has a very small unphysical range in the extreme limits of the (a,g) plane. As the index contrast increases to $\Delta n^2 = 0.245$, the unphysical range increases dramatically. However, a further increase to $\Delta n^2 = 0.375$ decreases the unphysical range. The unphysical ranges of the $P_3 + \delta E(4)$ approximation are again invariant to changes in Δn^2.

Our investigations of the unphysical ranges show that the P_1 approximation to the RTE should not be used for slabs with anisotropic scattering. The P_3 approximation is physical almost everywhere, for samples with a refractive index matching with the medium outside. Nevertheless, detailed investigations (not shown here) of the P_3 approximation for $\Delta n^2 = 0$ show that there are significant relative errors in the dominant forward scattering range ($g > 0.5$). The $P_3 + \delta E(4)$ approximation is found to be physical for the forward scattering region and invariant for the changes in b and Δn^2. It is, however, the worst approximation considered here for the backscattering region.
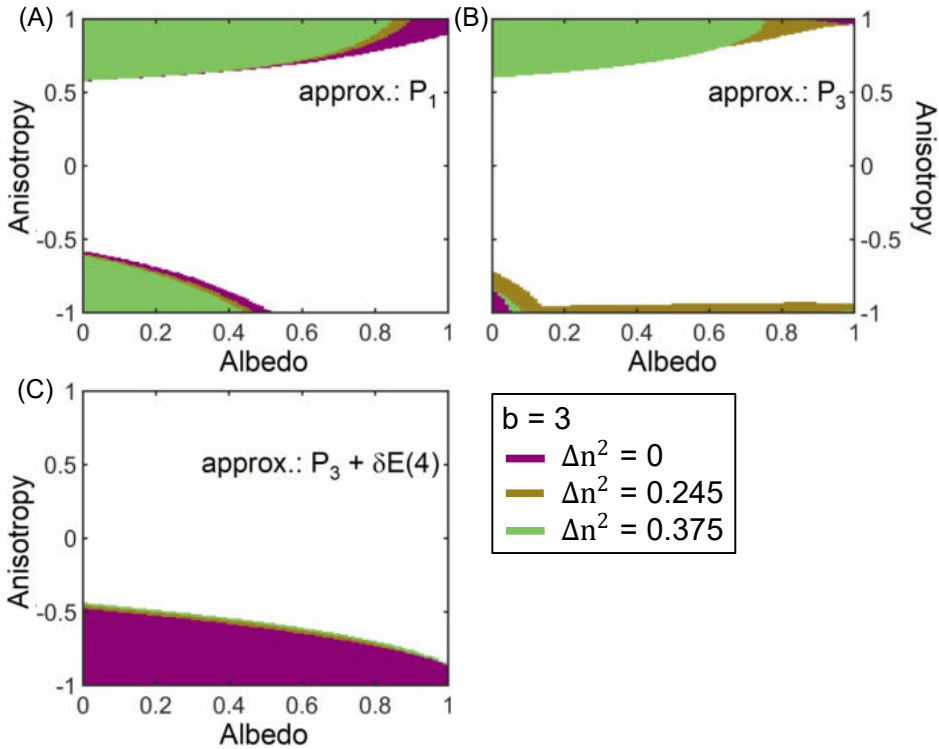
Figure 3.4: Unphysical ranges of (A) P_1 approximation, (B) P_3 approximation and (C) $P_3 + \delta E(4)$ approximation, for various refractive index contrasts and for fixed optical thickness $b = 3$.

3.3 Are the physical ranges accurate?

The unphysical ranges of the approximations show where these approximations should not be used, especially to determine the position dependent energy density inside scattering media. However, this does not mean that in the physical ranges the approximations are accurate. To check this, we compare the approximations to accurate Monte Carlo simulations.

3.3.1 Monte Carlo simulation

The Monte Carlo simulations used in this work follow the same principles as the work of Prahl et al. [58] and of Jacques [60]. In brief, one photon is repeatedly launched inside the photonic scattering slab, with a "photon weight" of 1 and initial direction $\hat{z}$. The photon moves a step length based on the probability of photon travel before getting absorbed or scattered inside the slab. After that step, a fraction of photon weight (determined by the albedo) is deposited at the local bin in that location, and the remaining weight is propagating into new direction, determined by using the Henyey-Greenstein phase function [109] for

the specified anisotropy. The propagation is continued by generating new steps until the photon escapes a boundary or its weight is below a threshold.

The main difference of our simulation code with those of Prahl *et al.* [58] and Jacques [60] is the incorporation of multiple internal reflection of photons from the boundaries of the slab (see Fig. 1.4). If an extremely long step length is generated, a fraction of the photon weight could end up internally reflecting multiple times. This situation is considered in our simulations by the addition of intensity Fabry-Perot calculations [110].

The Monte Carlo simulations are verified by comparing their results with exact calculations (and diffusion approximation for a slab with very long optical thickness $b = 100$). The comparisons are reported in Table 3.1 provided at the end of this chapter. The Lambert-Beer-Bouguer law used in Table 3.1 is

$$I_{\mathrm{u}} = I_0 e^{-\rho \sigma_{\mathrm{t}} L} \equiv I_0 e^{-b}, \tag{3.5}$$

where I_{u} is the transmitted unscattered intensity and I_0 is the incident intensity. We compare this with the case where $a = 0$, so the total transmission only has the unscattered component as the diffuse part is completely absorbed. For the purely forward scattering and non-absorbing case ($a = 1$; $g = 1$) we compared our Monte Carlo simulations to the Intensity Fabry-Pérot calculations, for which only the internal reflections from the boundaries of the slab determines the total transmission and reflection of the slab. In addition, an anisotropic case with weak absorption ($g = 0.75$; $a = 0.9$) is compared with the calculations reported by van de Hulst in Table 35 of Ref. [111]. It is clear from Table 3.1 that our Monte Carlo simulations are in good agreement with all of the compared methods, which indicates the high accuracy of our simulations.

3.3.2 Evaluating relative errors for validating models

In practice, the transport mean free path ℓ_{tr} and the absorption mean free path ℓ_{abs} are extracted from total transmission and total reflection experiments using a P_N approximation [82]. The unphysical ranges of a P_N approximation are essential to recognize for which photonic scattering slabs that particular P_N approximation should not be used for extracting these transport parameters. However, the bare acknowledgement of the unphysical ranges do not give any information on the accuracy of these methods to interpret observations on samples residing in the physical regions. Therefore, we extensively compare with Monte Carlo simulations to obtain relative error maps of transport parameters obtained by the analytical approximation methods. The optical thickness and refractive index contrast are chosen to be ($b = 3$, $\Delta n^2 = 0.245$), relevant to real samples.

Comparisons are done on the basis of the observation of both the total transmission T and total reflection R that can come from a real experiment or from Monte Carlo simulations. The comparison takes four steps:

1. We calculate T and R using Monte Carlo simulations, using a fine grid in parameter space (a, g): $T^{\mathrm{MC}}\{a, g\}$ and $R^{\mathrm{MC}}\{a, g\}$. We compare these Monte Carlo results to the P_N results obtained for all albedos and anisotropies,
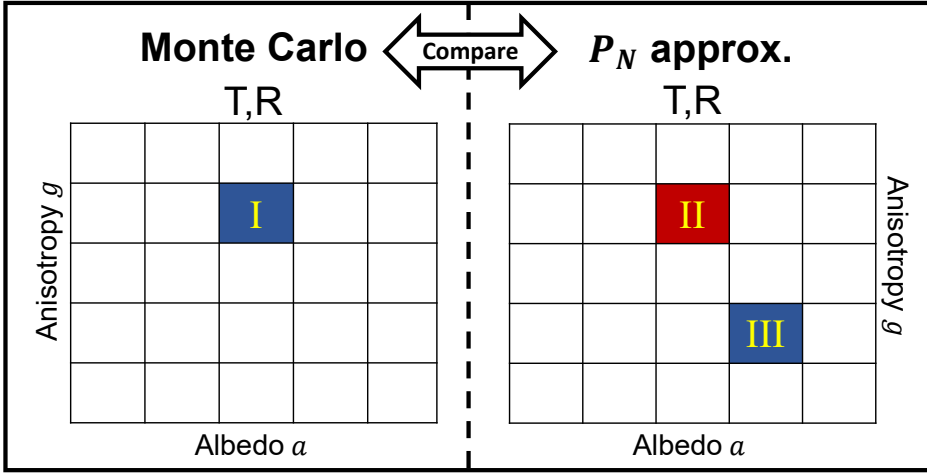
Figure 3.5: Illustration of the comparison process of the analytical methods and Monte Carlo simulations. The albedo a and anisotropy g parameters are used as coordinates for the comparisons. The data on the grids represent the total transmission and total reflection results (T,R). The grid on the left presents the results of the Monte Carlo calculations and the right one presents the results of P_N approximation. The comparison process is explained in detail in subsection 3.3.2.

using the same fine grid in parameter space (a', g'): $T^{P_N}\{a', g'\}$ and $R^{P_N}\{a', g'\}$. We define the squared relative distance between the two results

$$\delta T(a, g, a', g') \equiv \frac{\left[T^{\mathrm{MC}}(a,g) - T^{P_N}(a',g')\right]^2}{|T^{\mathrm{MC}}(a,g)|^2}, \tag{3.6}$$

$$\delta R(a, g, a', g') \equiv \frac{\left[R^{\mathrm{MC}}(a,g) - R^{P_N}(a',g')\right]^2}{|R^{\mathrm{MC}}(a,g)|^2}. \tag{3.7}$$

We also define the overall relative distance between the two calculations

$$S(a, g, a', g') \equiv \sqrt{\delta T(a, g, a', g') + \delta R(a, g, a', g')}. \tag{3.8}$$

2. As a first impression of the errors, the results are compared by calculating relative errors [112] for identical grid points $a = a'$ and $g = g'$, defined by

$$\Delta T(a, g) \equiv \sqrt{\delta T(a, g, a, g)} \times 100, \tag{3.9}$$

$$\Delta R(a, g) \equiv \sqrt{\delta R(a, g, a, g)} \times 100. \tag{3.10}$$

An example of a comparison in this step corresponds to comparing the blue square I in the Monte Carlo grid with the red square II in the P_N grid in Fig. 3.5. The relative error maps for all (a, g) are shown in Fig. 3.6(a-f).

3. In a real experiment, one measures the total transmission T and the total reflection R of a sample and uses a numerical or an analytical method
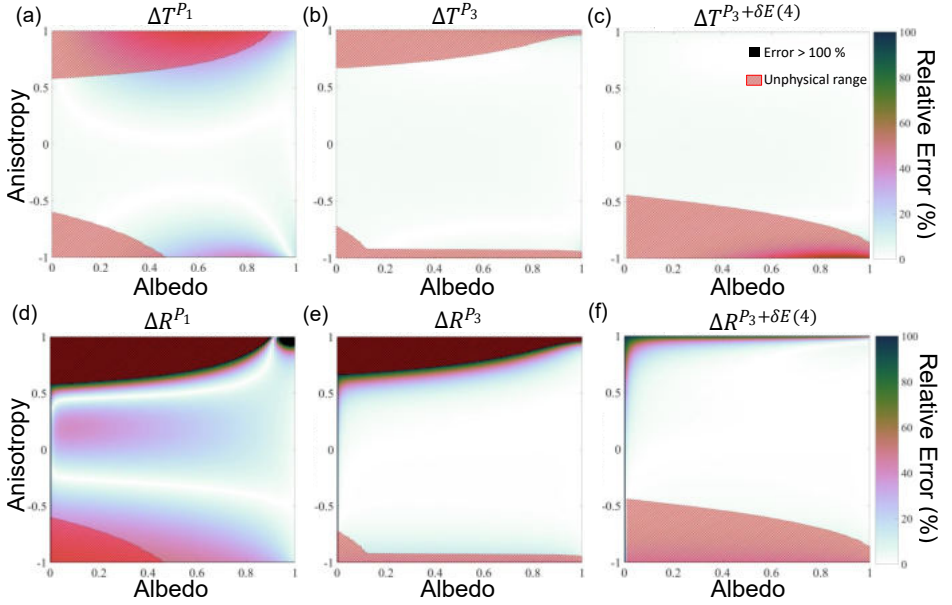
Figure 3.6: Relative error maps of the total transmission and the total reflection results for the P_N approximations. (a) and (d) for P_1, (b) and (e) for P_3, (c) and (f) for $P_3 + \delta E(4)$. Relative errors reported here are calculated by comparing these approximations to our Monte Carlo simulations. Color map indicates the percentage of errors. Values that are larger than 100% are indicated with black markers. The unphysical ranges of the approximations are added to the graphs as red hatched regions. Optical thickness and refractive index contrast are specifically chosen as $b = 3$ and $\Delta n^2 = 0.245$ for these relative error maps.

to infer the (a, g) parameters that corresponds to the observations. In this work we take T and R from Monte Carlo simulations as they are highly accurate (see Table 3.1 at the end of this chapter). We call the set obtained from Monte Carlo simulations (a_I, g_I), from which we infer the true transport lengths, ℓ_{tr} and ℓ_{abs}. If we interpret the Monte Carlo T and R results with the P_N approximation, we obtain the parameter set called (a_{III}, g_{III}), that minimizes the distance $S(a_I, g_I, a_{III}, g_{III})$. From the matched pair (a_{III}, g_{III}) we infer the mean free paths $\ell_{tr}^{P_N}(a_{III}, g_{III})$ and $\ell_{abs}^{P_N}(a_{III}, g_{III})$ of that sample using the appropriate P_N approximation. This step is illustrated in Fig. 3.5 where the blue grid point III in the P_N grid represents (a_{III}, g_{III}) pair fitted to the blue grid point I in the Monte Carlo grid.

4. In the final step, the procedure of the previous step is repeated for all possible (a_I, g_I) and its *matched* pair (a_{III}, g_{III}), and we calculate the relative

errors of the interpretations of the analytic P_N approximation:

$$\Delta\ell_{\text{tr}}(a_{\text{I}}, g_{\text{I}}) \equiv \sqrt{\frac{\left[\ell_{\text{tr}}^{\text{MC}}(a_{\text{I}}, g_{\text{I}}) - \ell_{\text{tr}}^{\text{P}_N}(a_{\text{III}}, g_{\text{III}})\right]^2}{\left[\ell_{\text{tr}}^{\text{MC}}(a_{\text{I}}, g_{\text{I}})\right]^2}} \times 100, \qquad (3.11)$$

$$\Delta\ell_{\text{abs}}(a_{\text{I}}, g_{\text{I}}) \equiv \sqrt{\frac{\left[\ell_{\text{abs}}^{\text{MC}}(a_{\text{I}}, g_{\text{I}}) - \ell_{\text{abs}}^{\text{P}_N}(a_{\text{III}}, g_{\text{III}})\right]^2}{\left[\ell_{\text{abs}}^{\text{MC}}(a_{\text{I}}, g_{\text{I}})\right]^2}} \times 100. \qquad (3.12)$$

These results are plotted in Fig. 3.7 for all $(a_{\text{I}}, g_{\text{I}})$.
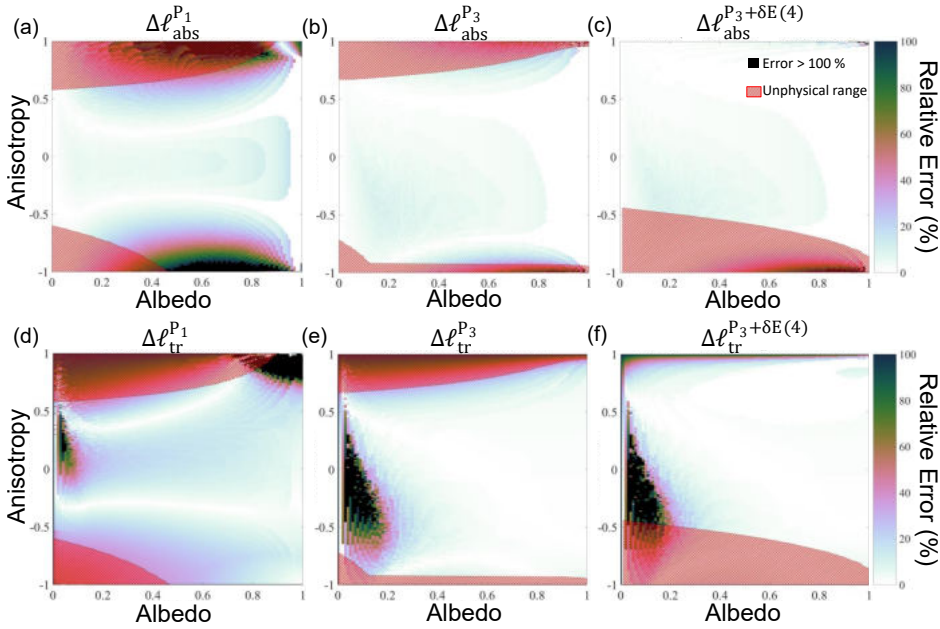
Figure 3.7: Relative error maps of absorption mean free path ℓ_{abs} and transport mean free path ℓ_{tr} for the P_N approximations. (a) and (d) for P_1, (b) and (e) for P_3, and (c) and (f) for $P_3 + \delta E(4)$. Relative errors reported here are calculated by comparing these approximations to our Monte Carlo simulations, according to the coordinates found from the fitting process explained in the text and illustrated in Fig. 3.5. Color map indicates the percentage of errors. Values that are larger than 100% are indicated with black markers. The unphysical ranges of the approximations are added to the graphs as red hatched regions. Optical thickness and refractive index contrast are specifically chosen as $b = 3$ and $\Delta n^2 = 0.245$ for these relative error maps.

3.3.3 Relative error maps inside and outside the physical ranges

Fig. 3.6 shows the relative error maps that present the deviations of the total transmission and the total reflection calculations of the analytical methods from the Monte Carlo simulations for realistic parameters $b = 3$ and $\Delta n^2 = 0.245$.

Fig. 3.6(a) shows that the total transmission results of the P_1 approximation have up to 53% relative error in the unphysical forward scattering region, and up to 86% relative error in the backscattering regions. For the P_1 approximation, the relative errors observed in total transmission occur for more directional scattering, however, significant relative errors are also observed for the total reflection results in the isotropic regions ($g \approx 0$) reaching as high as 29% for absorbing samples (see Fig. 3.6(d)). For an isotropic sample the errors in total reflection decrease as the absorption decreases and are less than 5% when the sample has no absorption ($a = 1$). Fig. 3.6(d) shows that the total reflection results of the P_1 approximation have large relative errors for most of the physical region, that can exceed 500% for forward scattering samples with $g > 0.9$. In the unphysical forward scattering region, the errors reach up to 10^3%. These results show that the P_1 approximation is particularly bad at describing total reflection, even for photonic scattering slabs with weak absorption. This observation is in line with our observations that the unphysical behaviors are usually encountered near the incident (left) boundary of the slab, where the light enters the slab (see Figs. 3.1(C,D)).

Relative errors of total transmission of the P_3 approximation are given in Fig. 3.6(b), which shows that it generally has less than 10% error in its physical regions. For the unphysical forward scattering and backscattering cases, the errors are 25% at most. Similar to the P_1 approximation, in the extreme forward scattering unphysical regions ($g > 0.9$), the P_3 approximation has large relative errors that go up to 10^4% in total reflection (see Fig. 3.6(e)). For the backscattering unphysical region, the P_3 approximation has errors up to 21% at most. In the physical regions, the relative errors of total reflection calculations of the P_3 approximation go up to 100% as the sample is in the vicinity of the unphysical forward scattering region. However, for the significant part of the physical region where there is weak anisotropy ($g < 0.5$ and $g > -0.5$), the relative errors are less than 10%.

Figs. 3.6(c,f) show that the $P_3 + \delta E(4)$ approximation has up to 73% relative error in the total transmission for extremely backscattering samples ($g < -0.9$). Even though the relative errors in total reflection results go up to 98% for regions where $g > 0.9$ and $a < 0.1$, the remaining forward scattering range where $0.5 < g < 0.9$ is much more accurate than with the P_1 and P_3 approximations.

Fig. 3.7 presents the deviations of the inferred mean free paths ℓ_{tr}^{PN} and ℓ_{abs}^{PN}, predicted by analytic approximations using "measured" total transmission (T^{MC}) and total reflection (R^{MC}), from the "real" ℓ_{tr}^{MC} and ℓ_{abs}^{MC} transport parameters.

Fig. 3.7(a) shows that the $\ell_{abs}^{P_1}$ has errors up to 211% for the forward scattering unphysical range. In addition, it is clear that the P_1 approximation also has large errors in the physical part of the forward scattering range. In the unphysical backscattering range, the relative errors of $\ell_{abs}^{P_1}$ are up to 100%, whereas, in the physical backscattering range, the errors reach 166%.

For the transport mean free path $\ell_{tr}^{P_1}$, Fig. 3.7(d) shows that the P_1 approximation has up to 56% error for the backscattering range. In the forward scattering unphysical range, errors up to 100% are observed. In the physical, non-absorbing, and dominant forward scattering range, relative errors reach 10^7%. Another high

error region, for which errors up to 123%, is seen in Fig. 3.7(d), where there is strong absorption ($a < 0.2$).

Fig. 3.7(b) shows that the P_3 approximation has up to 100% relative error in the absorption mean free path $\ell_{\mathrm{abs}}^{P_3}$ results for the strongly anisotropic samples $g < -0.9$ and $g > 0.9$. Moreover, the errors in the physical regions have fewer errors compared to the P_1 approximation. The relative error map for $\ell_{\mathrm{tr}}^{P_3}$ given in Fig. 3.7(e) shows relative errors up to 306% in the strong absorption regions ($a < 0.3$). In the unphysical forward scattering range, the errors of $\ell_{\mathrm{tr}}^{P_3}$ go up to 98%. In the rest of the grid, the P_3 approximation has significantly less relative errors than the P_1 approximation for extracting ℓ_{tr}.

The relative error map of $\ell_{\mathrm{abs}}^{P_3+\delta E(4)}$ given in Fig. 3.7(c) shows that the $P_3 + \delta E(4)$ approximation has fewer regions with large errors compared to the P_1 and the P_3 approximations. In the extremely anisotropic cases, however, the errors of $\ell_{\mathrm{abs}}^{P_3+\delta E(4)}$ reach 10^6% for $g = 0.98$, and 200% for $g = -0.99$. For $\ell_{\mathrm{tr}}^{P_3+\delta E(4)}$, Fig. 3.7(f) shows that fewer regions with large errors, especially in the forward scattering range, compared to the P_1 and the P_3 approximations. In addition, Fig. 3.7(f) shows that the $P_3 + \delta E(4)$ approximation, similar to the P_3 approximation, has errors as large as 322% in regions with strong absorption ($a < 0.3$).

Fig. 3.7 shows that the P_1 approximation has more regions in the grid with large relative errors, as expected. As the absorption increases, the P_3 and the $P_3 + \delta E(4)$ approximations predict results with relative errors more than 100%, however, both are more accurate for the rest of the grid, with the $P_3 + \delta E(4)$ approximation performing better for a wider forward scattering range.

With prior knowledge of parameters (a, g, b, Δn^2), one can verify if a sample is in the unphysical ranges and use the relative error maps provided in this work to see if any of the reported P_N approximations are appropriate for their sample. Needless to say, if (a, g, b, Δn^2) are already known, one could get the transport parameters ℓ_{tr} and ℓ_{abs} without the use of P_N approximation, given that the density of scatterers in their sample fulfils the independent scattering approximation [9]. Nevertheless, it is necessary to use either analytical approximations or numerical methods to infer the position-dependent energy density $u(z)$ and the diffuse flux $F(z)$ inside the sample. Hence, for these investigations, the unphysical ranges and relative error maps of the analytical methods are crucial.

3.3.4 Practical cases

A first practical example is a slab of human dermis in air. The optical constants of this slab are [113]: $a = 0.99$, $g = 0.81$, and $\Delta n^2 = 0.245$ (assuming $n_{\mathrm{slab}} = 1.4$). If the slab has an optical thickness $b = 3$, Figs. 3.6 and 3.7 serve to choose the analytical approximation to infer the position-dependent energy density and diffuse flux inside the tissue. In this case, the $P_3 + \delta E(4)$ approximation would be the best choice, as it has less than 1% error for extracting ℓ_{tr} and ℓ_{abs}. This decision is in line with Star [37], who investigated a thicker ($b = 9.5$) slab of human dermis and found the $P_3 + \delta E(4)$ approximation to be more accurate than the P_3 approximation.

Other examples stem from the solid state lighting industry, where understanding the light transport in white LEDs is an important issue. A typical white LED contains a phosphor layer that absorbs incoming blue light and re-emits light in different wavelengths to achieve white output. In reference [82], polymer slabs containing phosphor (YAG:Ce^{3+}) scatterers are studied, and their optical constants are found using Monte Carlo simulations and the P_3 approximation. The refractive index of the polymer matrix is $n_{slab} = 1.4$, and the surrounding medium is air, which gives $\Delta n^2 = 0.245$. The optical constants for such a slab are derived to be [82]: $a = 0.89$, $g = 0.72$ at a wavelength $\lambda = 460$nm where the phosphors are absorbing, and $a = 1$, $g = 0.82$ at $\lambda = 600$nm where the phosphors are non-absorbing. If we consider a slab with optical thickness $b = 3$ and look at the Figs. 3.6 and 3.7, we see that the $P_3 + \delta E(4)$ approximation would be the best one to use for both cases since it has less than 1% error for extracting ℓ_{tr} and ℓ_{abs}, whereas the P_3 approximation has $\Delta\ell_{tr}^{P_3} = 7\%$ for absorbing, and $\Delta\ell_{tr}^{P_3} = 10\%$ for non-absorbing wavelengths.

Earlier on, Jacques *et al.* have experimentally and numerically investigated light distribution in various phosphor plates [114]. The optical constants of a slab containing composite ceramic Ce:YAG are reported as: $a = 0.71$, $g = 0.75$ at a wavelength $\lambda = 450$nm where the phosphors are absorbing [114]. Assuming the index contrast $\Delta n^2 = 0.245$, and the optical thickness $b = 3$, Figs. 3.6 and 3.7 shows less than 1% error for $\Delta\ell_{tr}^{P_3+\delta E(4)}$ and $\Delta\ell_{abs}^{P_3+\delta E(4)}$. The lengths extracted using the P_3 approximation have $\Delta\ell_{tr}^{P_3} = 16.15\%$ and $\Delta\ell_{abs}^{P_3} = 7.41\%$, and with the P_1 approximation have $\Delta\ell_{tr}^{P_1} = 0.4\%$ and $\Delta\ell_{abs}^{P_1} = 52.63\%$. A more absorbing slab containing Ce:LuAG and Eu:nitride has reported optical constants $a = 0.25$ and $g = 0.75$ at a wavelength $\lambda = 450$nm [114]. With $\Delta n^2 = 0.245$ and $b = 3$, Figs. 3.6 and 3.7 shows that the $P_3 + \delta E(4)$ approximation yields ℓ_{tr} and ℓ_{abs} with less than 1% relative error, whereas with the P_1 approximation have $\Delta\ell_{tr}^{P_1} = 62.26\%$ and $\Delta\ell_{abs}^{P_1} = 38.89\%$, and the P_3 approximation have $\Delta\ell_{tr}^{P_3} = 40.13\%$ and $\Delta\ell_{abs}^{P_3} = 5.63\%$. For both slabs, the $P_3 + \delta E(4)$ is the best analytical approximation out of all three, as it gives the least relative errors, in agreement with our discussions above.

3.4 Summary

We have studied the unphysical ranges of the P_1, P_3, and $P_3 + \delta E(4)$ approximations to the radiative transfer equation. First of all, we have defined a physically sensible parameter space by albedo, anisotropy, optical thickness, and index contrast (a, g, b, Δn^2). The unphysical parameter ranges are characterized by unphysical negative energy densities and fluxes of the wrong sign. These ranges are crucial when the position-dependent energy density inside the photonic scattering slab is being investigated. We find that the delta function correction to P_3 eliminates the unphysical range in the forward scattering, but not in backscattering.

Typically researchers want to extract the transport parameters ℓ_{tr} and ℓ_{abs} from total transmission and reflection experiments. We have presented the rela-

tive errors in the transport parameters for all possible albedo and anisotropy and for realistically chosen optical thickness and refractive index contrast, by comparing the analytical results with Monte Carlo simulations. These relative error maps provide a guideline for the accuracy of the analytical methods to interpret experiments on light transport in photonic scattering slabs. In the unphysical ranges the relative errors are as large as $10^4\%$, but also in the physical ranges the errors can be substantial. We emphasize that the relative error maps provided here are for slabs with widely studied realistic optical thickness and refractive index contrast. Maps for any other kind of samples with their specific parameters require characterization using the methodology explained here.

We conclude that the P_1 approximation is not viable to extract either the transport parameters or the position dependent energy density, unless the scattering of the sample is purely isotropic and elastic. The P_3 and $P_3 + \delta E(4)$ approximations are more reliable to use than the P_1 approximation, unless there is strong absorption ($a < 0.3$) or extreme anisotropy ($g > 0.9$ and $g < -0.9$). The approximations should not be used if the samples are in the unphysical parameter range, even though the relative errors are low in some parts of these unphysical ranges. Especially, the $P_3 + \delta E(4)$ approximation is suited for enhancing the accuracy in the forward direction ($g > 0$) and should not be used in the backscattering range ($g < 0$). Our results provide a guideline for the applicability of the P_1, P_3, and $P_3 + \delta E(4)$ approximations to the radiative transfer equation, to interpret experiments on light transport in photonic scattering slabs.

Method	a	g	b	n_{slab}	Total Transmission		Reflection		Absorption	
Lambert-Beer-Bouguer	0	0.75	3	1	4.9787%		-		-	
Monte Carlo					4.9859%	± 0.0069%	0.0000%	± 0.0000%	95.0141%	± 0.0069%
Intensity Fabry-Pérot	1	1	3	1.4	94.5946%		5.4054%		-	
Monte Carlo					94.5946%	± 0.32×10^{-7}%	5.4054%	± 0.18×10^{-7}%	0.00%	
Diffusion (P_1 approx.)	1	0	100	1.5	3.1307%		96.8693%		0.00%	
Monte Carlo					3.1229%	± 0.0164%	96.8771%	± 0.0164%	0.00%	
van de Hulst [111]	0.9	0.75	2	1	66.096%		9.739%		-	
Monte Carlo					66.1001%	± 0.0104%	9.7408%	± 0.0074%	24.1591%	± 0.0059%

Table 3.1: Verification of our Monte Carlo simulations. Absorbing ($a = 0$), non-absorbing ($a = 1$), isotropic ($g = 0$), and forward scattering ($g \geq 0.75$) cases are compared.

4 Derivation of the $\mathrm{P_N}$ approximation to the radiative transfer equation for a slab

4.1 Introduction

In this chapter, we give the detailed theoretical background of most of the research done in this thesis. We start by deriving the radiative transfer equation (RTE), and give its version of a slab geometry. We then derive the $\mathrm{P_N}$ approximation to RTE for a slab, and solve its first and third order, and provide the derivations of a correction to $\mathrm{P_3}$ approximation for the forward direction, namely, the $\mathrm{P_3} + \delta\mathrm{E}(4)$ approximation. Finally, we discuss the consideration of dielectric cuvette walls surrounding the slab and the resulting internal reflections of the unscattered incident light in the models. Additionally, we discuss the alternative phase functions to the Henyey-Greenstein [109] phase function that is used in this work. Before starting with the derivations, we need to define important quantities, such as, the specific intensity, the flux and the energy density. The definitions and derivations in this chapter follow chapter 7 of Ref. [1], hence, the reader is referred to that textbook for more insight on transport theory.
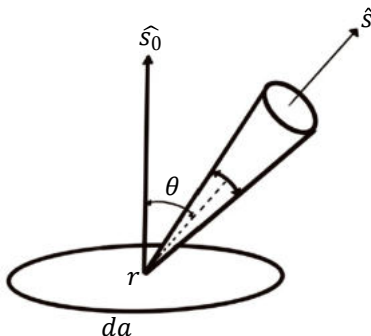
4.1.1 Specific Intensity

Figure 4.1: Illustration of directions for the specific intensity $I(\mathbf{r}, \hat{\mathbf{s}}, \nu)$ and power dP given in eqn. (4.1). Figure adapted from [1].

At a particular point in a random medium where the energy of wave flows, the properties of the wave such as phase, and amplitude vary randomly over time.

As a result, the magnitude and direction of the power flux density vector also change continuously. If we define a unit vector $\hat{\mathbf{s}}$ to represent a specific direction, we find the average power flux density within a frequency bandwidth $d\nu$ centred at frequency ν within a unit solid angle. This value, denoted as $I(\mathbf{r}, \hat{\mathbf{s}}, \nu)$, is the specific intensity (also known as the spectral radiance) and is measured in units of $\mathrm{Wm}^{-2}\mathrm{sr}^{-1}\mathrm{Hz}^{-1}$. The amount of power dP flowing through an elementary area dA oriented in the direction of unit vector $\hat{\mathbf{s}}_0$ within a unit solid angle (indicated as $d\hat{\mathbf{s}}$ in integrals) over a frequency interval $(\nu, \nu + d\nu)$ is given as

$$dP = I(\mathbf{r}, \hat{\mathbf{s}}, \nu)\cos\theta dA d\hat{\mathbf{s}} d\nu, \tag{4.1}$$

where $\cos\theta = \hat{\mathbf{s}} \cdot \hat{\mathbf{s}}_0$

4.1.2 Flux

The total forward flux in direction $\hat{\mathbf{s}}_0$, passing through an infinitesimal area dA, centred at position $\mathbf{r}$, on a surface is given by integrating eqn. (4.1) with the specific intensity over a solid angle 2π within the forward range $(0 \leq \theta \leq \frac{\pi}{2})$. The flux is written as $\mathbf{F}_+(\mathbf{r}, \hat{\mathbf{s}}_0, \nu)dA$, where the forward flux density is

$$\mathbf{F}_+(\mathbf{r}, \hat{\mathbf{s}}_0, \nu) \equiv \int_{(2\pi)^+} I(\mathbf{r}, \hat{\mathbf{s}}, \nu)\cos\theta d\hat{\mathbf{s}}, \tag{4.2}$$

where $\hat{\mathbf{s}}_0$ represents a unit vector normal to the surface dA. Similarly, we define the backward flux density $\mathbf{F}_-$ for the flux flowing through dA at $\mathbf{r}$ in the backward $(-\hat{\mathbf{s}}_0)$ direction. This flux is given by integrating eqn. (4.1) over a solid angle 2π in the backward range $(\frac{\pi}{2} \leq \theta \leq \pi)$, and the backward flux density is

$$\mathbf{F}_-(\mathbf{r}, \hat{\mathbf{s}}_0, \nu) \equiv \int_{(2\pi)^-} I(\mathbf{r}, \hat{\mathbf{s}}, \nu)\hat{\mathbf{s}} \cdot (-\hat{\mathbf{s}}_0)d\hat{\mathbf{s}}. \tag{4.3}$$
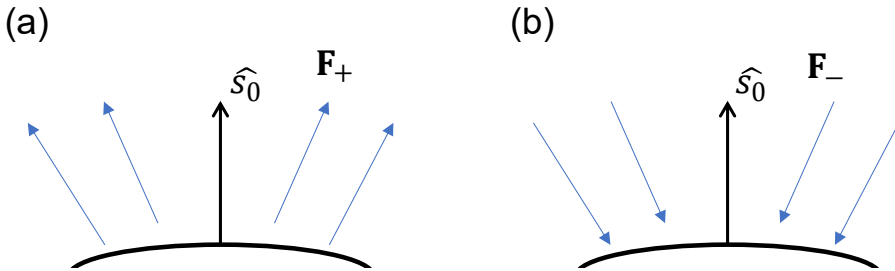

Figure 4.2: Illustration of (a) forward flux density $\mathbf{F}_+$ and (b) backward flux density $\mathbf{F}_-$. Figure adapted from [1].

The total flux density, forward and backward, in the direction $\hat{\mathbf{s}}_0$ is the vector sum of $\mathbf{F}_+$ and $\mathbf{F}_-$. It is expressed as the component of the flux density vector

$\mathbf{F}(\mathbf{r}, \nu)$ along $\hat{\mathbf{s}}_0$, where the integration is taken over a complete solid angle 4π,

$$\mathbf{F}_+(\mathbf{r}, \hat{\mathbf{s}}_0, \nu) - \mathbf{F}_-(\mathbf{r}, \hat{\mathbf{s}}_0, \nu) \equiv \mathbf{F}(\mathbf{r}, \nu) \cdot \hat{\mathbf{s}}_0, \tag{4.4}$$

$$\mathbf{F}(\mathbf{r}, \nu) \equiv \int_{4\pi} I(\mathbf{r}, \hat{\mathbf{s}}, \nu)\hat{\mathbf{s}}d\hat{\mathbf{s}}. \tag{4.5}$$

$\mathbf{F}(\mathbf{r}, \nu)$ represents the amount and the direction of the net flow of power, with units of $\mathrm{Wm}^{-2}\mathrm{Hz}^{-1}$.

4.1.3 Energy density, average intensity and energy fluence rate

Let us consider a small area dA, the energy leaving that area in a time duration dt, in a direction normal to the area within a solid angle $d\hat{\mathbf{s}}$ and a frequency interval $(\nu, \nu + d\nu)$ is $I dA d\hat{\mathbf{s}} d\nu dt$. The corresponding energy density is determined by considering the volume occupied by the energy flowing through dA, which is equal to $dA\,c\,dt$, where c is the velocity of the wave propagation. Therefore, the energy density $du(\mathbf{r})$ at $\mathbf{r}$ in a unit frequency interval $d\nu$ is

$$du(\mathbf{r}, \nu) = \frac{I dA d\hat{\mathbf{s}} d\nu dt}{dA c dt d\nu} = \frac{I(\mathbf{r}, \hat{\mathbf{s}}, \nu)d\hat{\mathbf{s}}}{c}. \tag{4.6}$$

When we consider the addition of energy due to the radiation in *all* directions, the energy density $u(\mathbf{r}, \nu)$ is integrated over all directions

$$u(\mathbf{r}, \nu) = \frac{1}{c} \int_{4\pi} I(\mathbf{r}, \hat{\mathbf{s}}, \nu)d\hat{\mathbf{s}}. \tag{4.7}$$

In certain cases, it is more useful to define the average intensity $U(\mathbf{r}, \nu)$ or the energy fluence rate $\Phi(\mathbf{r}, \nu)$ as the integral of the specific intensity over all directions. The average intensity is given as

$$U(\mathbf{r}, \nu) \equiv \frac{1}{4\pi} \int_{4\pi} I(\mathbf{r}, \hat{\mathbf{s}}, \nu)d\hat{\mathbf{s}} = \frac{c}{4\pi}u(\mathbf{r}, \nu), \tag{4.8}$$

and the energy fluence rate is

$$\Phi(\mathbf{r}, \nu) = \int_{4\pi} I(\mathbf{r}, \hat{\mathbf{s}}, \nu)d\hat{\mathbf{s}} = cu(\mathbf{r}, \nu). \tag{4.9}$$

The average intensity is equal to the normalized energy density $u(\mathbf{r}, \nu)$ and does not represent the power flow. The energy fluence rate $\Phi(\mathbf{r}, \nu)$ has units $\mathrm{Wm}^{-2}\mathrm{Hz}^{-1}$, same as the flux density $\mathbf{F}(\mathbf{r}, \nu)$, however, $\Phi(\mathbf{r}, \nu)$ represents the total optical power *through a sphere* of unit surface area in all directions, while $\mathbf{F}(\mathbf{r}, \nu)$ represents the optical power *through a surface* of unit area in a direction parallel to the surface normal [23], as illustrated in Fig. 4.3.
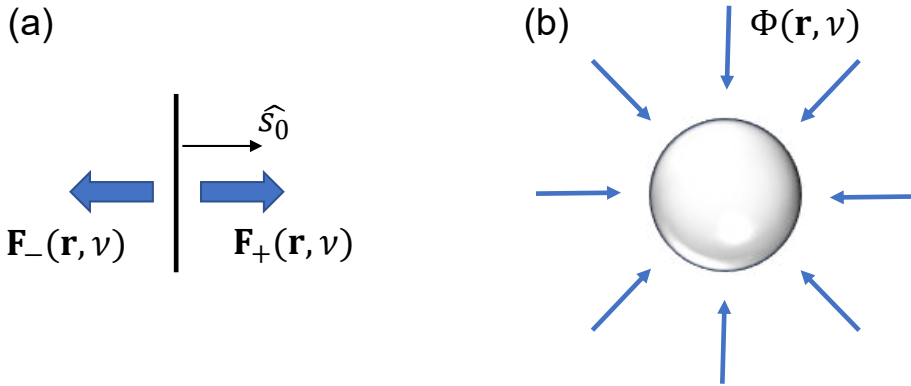
Figure 4.3: Illustration of (a) forward and backward flux densities that represent power flow through a unit surface area in a direction parallel to the surface normal, and (b) energy fluence rate $\Phi(\mathbf{r}, \nu)$ that represent the total power flow through a unit spherical surface in all directions.

4.1.4 Radiative transfer equation

Here we derive the radiative transfer equation (RTE) following chapter 7 of Ref. [1]. After this point, we drop the frequency ν dependency of the specific intensity and write it as $I(\mathbf{r}, \hat{\mathbf{s}})$, as our study is near-monochromatic.

Consider an elementary volume dV with unit cross-section dA and length ds, that contains ρdV scatterers, where ρ represents the number of scatterers per unit volume. The specific intensity $I(\mathbf{r}, \hat{\mathbf{s}})$ is incident on this volume dV. Each scatterer, upon interacting with the total incident intensity I with units of Wm^{-2}, absorbs the power $\sigma_{\mathrm{abs}}I$ and scatters the power $\sigma_{\mathrm{scat}}I$. This is called extinction, and the decrease of specific intensity per length is represented as

$$\text{Decrease} = -\rho(\sigma_{\mathrm{scat}} + \sigma_{\mathrm{abs}})I(\mathbf{r}, \hat{\mathbf{s}}) = -\rho\sigma_{\mathrm{ext}}I(\mathbf{r}, \hat{\mathbf{s}}), \qquad (4.10)$$

where σ_{scat}, σ_{abs}, and σ_{ext} represent the scattering, the absorption and the extinction cross-sections respectively.

The specific intensity also increases when a portion of the specific intensity incident from another direction $\hat{\mathbf{s}}'$ is scattered into the direction $\hat{\mathbf{s}}$. This increase per length is equal to

$$\text{Increase} = \rho\sigma_{\mathrm{ext}}a \int_{4\pi} p(\hat{\mathbf{s}}, \hat{\mathbf{s}}')I(\mathbf{r}, \hat{\mathbf{s}}')d\hat{\mathbf{s}}', \qquad (4.11)$$

where a is the albedo, that is, the ratio of σ_{scat} to σ_{ext}, and $p(\hat{\mathbf{s}}, \hat{\mathbf{s}}')$ is the phase function that describes the probability of light arriving from the $\hat{\mathbf{s}}'$ direction to scatter into the $\hat{\mathbf{s}}$ direction. The probability is normalized, so integration of $p(\hat{\mathbf{s}}, \hat{\mathbf{s}}')$ over 4π is equal to 1.

The sources of the specific intensity, inside and outside the scattering medium, also have an effect on the spatial change of the intensity in the volume dV. We

sum all contributions including the source terms to obtain the RTE that describes the rate of change of the specific intensity in space as

$$\frac{dI(\mathbf{r}, \hat{\mathbf{s}})}{ds} = -\rho\sigma_{\text{ext}}I(\mathbf{r}, \hat{\mathbf{s}}) + \rho\sigma_{\text{ext}}a\int_{4\pi} p(\hat{\mathbf{s}}, \hat{\mathbf{s}}')I(\mathbf{r}, \hat{\mathbf{s}}')d\hat{\mathbf{s}}' + \epsilon_{\text{ri}}(\mathbf{r}, \hat{\mathbf{s}}) + \epsilon(\mathbf{r}, \hat{\mathbf{s}}), \quad (4.12)$$

where $\epsilon(\mathbf{r}, \hat{\mathbf{s}})$ and $\epsilon_{\text{ri}}(\mathbf{r}, \hat{\mathbf{s}})$ are internal and external source functions, respectively. These functions represent the power generated per unit volume per unit solid angle in the direction $\hat{\mathbf{s}}$ that accounts for all sources inside and outside the medium, respectively. Since we only consider sources outside the medium in this work, $\epsilon(\mathbf{r}, \hat{\mathbf{s}})$ is omitted from now on.

Furthermore, we decompose $I(\mathbf{r}, \hat{\mathbf{s}})$ as

$$I(\mathbf{r}, \hat{\mathbf{s}}) = I_{\text{ri}}(\mathbf{r}, \hat{\mathbf{s}}) + I_{\text{diff}}(\mathbf{r}, \hat{\mathbf{s}}), \quad (4.13)$$

where $I_{\text{diff}}(\mathbf{r}, \hat{\mathbf{s}})$ is the diffuse specific intensity and $I_{\text{ri}}(\mathbf{r}, \hat{\mathbf{s}})$ is the reduced specific intensity. The diffuse specific intensity I_{diff} is the intensity that is created after an extinction event in the volume. The reduced specific intensity I_{ri} is the part of the originally incident intensity that is left after extinction, and that satisfies the Lamber-Beer-Bouguer equation

$$\frac{dI_{\text{ri}}(\mathbf{r}, \hat{\mathbf{s}})}{ds} = -\rho\sigma_{\text{ext}}I_{\text{ri}}(\mathbf{r}, \hat{\mathbf{s}}). \quad (4.14)$$

We also express the external source function as

$$\epsilon_{\text{ri}}(\mathbf{r}, \hat{\mathbf{s}}) = \rho\sigma_{\text{ext}}a\int_{4\pi} p(\hat{\mathbf{s}}, \hat{\mathbf{s}}')I_{\text{ri}}(\mathbf{r}, \hat{\mathbf{s}}')d\hat{\mathbf{s}}'. \quad (4.15)$$

This means that we can express the spatial change of I_{diff} in volume ds as

$$\frac{dI_{\text{diff}}(\mathbf{r}, \hat{\mathbf{s}})}{ds} = -\rho\sigma_{\text{ext}}I_{\text{diff}}(\mathbf{r}, \hat{\mathbf{s}}) + \rho\sigma_{\text{ext}}a\int_{4\pi} p(\hat{\mathbf{s}}, \hat{\mathbf{s}}')I_{\text{diff}}(\mathbf{r}, \hat{\mathbf{s}}')d\hat{\mathbf{s}}' + \epsilon_{\text{ri}}(\mathbf{r}, \hat{\mathbf{s}}). \quad (4.16)$$

We use eqn. (4.16) as RTE when deriving the P_{N} approximations for the diffuse light; the complete RTE is just the addition of the unscattered light from eqn. (4.14).

4.2 Radiative transfer equation for a slab

The coordinate system for a slab geometry is shown in Fig. 4.4. When we consider a slab, where the (x, y) coordinates tend to $\pm\infty$, due to spatial symmetry the $\mathbf{r}$ dependence of the specific intensity simplifies into a z-dependence, and the angular dependence $\hat{\mathbf{s}}'$ simplifies to a μ-dependence, where $\mu \equiv \cos\theta$. We use the relation

$$\frac{d}{ds} = \frac{d}{dz}\frac{dz}{ds} = \cos\theta\frac{d}{dz} \equiv \mu\frac{d}{dz}, \quad (4.17)$$

and the RTE becomes

$$\mu \frac{dI_{\mathrm{diff}}(z,\mu)}{dz} = -\rho\sigma_{\mathrm{ext}}I_{\mathrm{diff}}(z,\mu)$$
$$+ \rho\sigma_{\mathrm{ext}}a(2\pi)\int_{-1}^{1}p(\mu,\mu')I_{\mathrm{diff}}(z,\mu')d\mu' \qquad (4.18)$$
$$+ \epsilon_{\mathrm{ri}}(z,\mu).$$

It is worth to note that we assume spherical scatterers in a slab that are well separated from each other for the derivations given here.
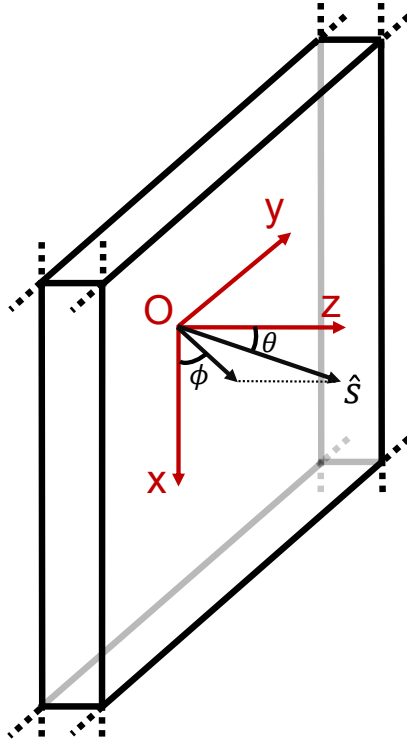

Figure 4.4: Coordinate system used in radiative transfer equation for slab geometry. The slab has finite thickness in z-direction and infinite at the xy-plane. ϕ is the azimuthal angle on xy-plane, and θ is the angle between $\hat{s}$ and z directions, a.k.a. the scattering angle.

4.2.1 P_N approximation to radiative transfer equation

The P_N approximation solves the RTE by expanding every term on the basis of spherical harmonics. The expansion of the specific intensity $I(\mathbf{r},\hat{s})$ is already given in eqn. (1.6). For a slab, spherical harmonics simplify to Legendre polynomials [76], as the azimuthal term vanishes after integration over 4π. This is

due to the symmetries introduced by the well-dispersed spherical scatterers in the slab. In the P_N approximation, I_{diff} is then expressed as

$$I_{\text{diff}}(z, \mu) = \sum_{l=0}^{\infty} \frac{2l+1}{2} \psi_l(z) P_l(\mu), \tag{4.19}$$

where $P_l(\mu)$ is a Legendre polynomial of order l and the coefficient $\psi_l(z)$ is equal to

$$\psi_l(z) = \int_{-1}^{1} I_{\text{diff}}(z, \mu) P_l(\mu) d\mu. \tag{4.20}$$

Similarly, the source term $\epsilon_{\text{ri}}(z, \mu)$ is expanded as

$$\epsilon_{\text{ri}}(z, \mu) = \sum_{l=0}^{\infty} \frac{2l+1}{2} s_l(z) P_l(\mu), \tag{4.21}$$

where the coefficient $s_l(z)$ is the lth moment of the source function. For plane waves incident perpendicularly to the slab surface as the source of light with incident flux F_0, the coefficient equals

$$s_l(z) = F_0 \rho \sigma_{\text{t}} a w_l e^{-\rho \sigma_{\text{t}} z}, \tag{4.22}$$

where w_l is the lth moment of the phase function.

The phase function $p(\hat{\mathbf{s}}, \hat{\mathbf{s}}')$ only depends on the angle between the incoming $\hat{\mathbf{s}}'$ and outgoing $\hat{\mathbf{s}}$ directions. Thus, we can expand the phase function as

$$p(\hat{\mathbf{s}}, \hat{\mathbf{s}}') = \sum_{l=0}^{\infty} \frac{2l+1}{4\pi} w_l P_l(\hat{\mathbf{s}} \cdot \hat{\mathbf{s}}'). \tag{4.23}$$

Using the addition theorem for spherical harmonics [76], we get

$$\begin{aligned} P_l(\hat{\mathbf{s}} \cdot \hat{\mathbf{s}}') &= P_l(\mu) P_l(\mu') + \\ &\left[2 \sum_{m=-l}^{l} \frac{(l-m)!}{(l+m)!} P_l(\mu)^m P_l(\mu')^m \cos\left[m(\phi'-\phi)\right] \right], \end{aligned} \tag{4.24}$$

where ϕ and ϕ' are azimuthal angles. Due to symmetries in the slab mentioned above, only $m = 0$ remains and the second term on the right-hand side vanishes after integration over 4π [69]. Thus we rewrite eqn. (4.23) as

$$p(\hat{\mathbf{s}}, \hat{\mathbf{s}}') = p(\mu, \mu') = \sum_{l=0}^{\infty} \frac{2l+1}{4\pi} w_l P_l(\mu) P_l(\mu'). \tag{4.25}$$

The well-known Henyey-Greenstein phase function [109] is given as

$$p(\hat{\mathbf{s}} \cdot \hat{\mathbf{s}}') = \frac{1}{4\pi}(1 - g^2)(1 + g^2 - 2g(\hat{\mathbf{s}} \cdot \hat{\mathbf{s}}'))^{-3/2}, \tag{4.26}$$

and has moments equal to powers of the anisotropy

$$w_l = g^l, \tag{4.27}$$

where g is the anisotropy, also called the asymmetry parameter.

Substituting eqns. (4.19), (4.21) and (4.25) into eqn. (4.18), we get

$$\mu \frac{dI_{\mathrm{diff}}(z,\mu)}{dz} + \sum_{l=0}^{\infty} \frac{2l+1}{2} \rho \sigma_{\mathrm{ext}} \psi_l(z) P_l(\mu)$$

$$- \rho \sigma_{\mathrm{ext}} a \int_{-1}^{1} \sum_{l=0}^{\infty} \frac{2l+1}{2} \sum_{l=0}^{\infty} \frac{2l+1}{2} w_l P_l(\mu) P_l(\mu') \psi_l(z) P_l(\mu') d\mu'$$

$$- \sum_{l=0}^{\infty} \frac{2l+1}{2} s_l(z) P_l(\mu) = 0. \tag{4.28}$$

Notice that we did not expand $I_{\mathrm{diff}}(z,\mu)$ in the first term yet. We will do that later for convenience. Let us multiply eqn. (4.28) with $P_n(\mu)$ and integrate over 2π

$$\int_{-1}^{1} P_n(\mu) \mu \frac{dI_{\mathrm{diff}}(z,\mu)}{dz} d\mu + \int_{-1}^{1} \sum_{l=0}^{\infty} \frac{2l+1}{2} \rho \sigma_{\mathrm{ext}} \psi_l(z) P_l(\mu) P_n(\mu) d\mu$$

$$- \int_{-1}^{1} \rho \sigma_{\mathrm{ext}} a \int_{-1}^{1} \sum_{l=0}^{\infty} \frac{2l+1}{2} \sum_{l=0}^{\infty} \frac{2l+1}{2} w_l P_n(\mu) P_l(\mu) P_l(\mu') \psi_l(z) P_l(\mu') d\mu' d\mu$$

$$= \int_{-1}^{1} \sum_{l=0}^{\infty} \frac{2l+1}{2} s_l(z) P_l(\mu) P_n(\mu) d\mu. \tag{4.29}$$

Let us now evaluate every term in eqn. (4.29) using the following recurrence

$$(2l+1)xP_l(x) = (l+1)P_{l+1}(x) + lP_{l-1}(x), \tag{4.30}$$

and the orthogonality properties

$$\int_{-1}^{1} P_l(x) P_n(x) dx = \frac{2}{2l+1} \delta_{ln}, \tag{4.31}$$

of the Legendre polynomials, where δ_{ln} is the Kronecker delta [76]. Hence, using eqns. (4.30) and (4.31), the first term in eqn. (4.29) becomes

$$\int_{-1}^{1} P_l(\mu) \mu \frac{dI_{\mathrm{diff}}(z,\mu)}{dz} d\mu = \int_{-1}^{1} \left(\frac{l+1}{2l+1} P_{l+1}(\mu) + \frac{l}{2l+1} P_{l-1}(\mu) \right) \frac{dI_{\mathrm{diff}}(z,\mu)}{dz}$$

$$= \frac{l+1}{2l+1} \frac{d}{dz} \int_{-1}^{1} P_{l+1}(\mu) I_{\mathrm{diff}}(z,\mu) d\mu$$

$$+ \frac{l}{2l+1} \frac{d}{dz} \int_{-1}^{1} P_{l-1}(\mu) I_{\mathrm{diff}}(z,\mu) d\mu$$

$$= \frac{l+1}{2l+1} \frac{d\psi_{l+1}}{dz} + \frac{l}{2l+1} \frac{d\psi_{l-1}}{dz}. \tag{4.32}$$

The second term becomes

$$\int_{-1}^{1} \sum_{l=0}^{\infty} \frac{2l+1}{2} \rho\sigma_{\text{ext}}\psi_l(z)P_l(\mu)P_n(\mu)d\mu = \rho\sigma_{\text{ext}}\psi_l(z). \qquad (4.33)$$

The third term becomes

$$\int_{-1}^{1} \sum_{l=0}^{\infty} \frac{2l+1}{2}(-\rho\sigma_{\text{ext}}a) \int_{-1}^{1} \sum_{l=0}^{\infty} \frac{2l+1}{2}w_l P_n(\mu)P_l(\mu)\psi_l(z)P_l(\mu')P_l(\mu')d\mu'd\mu$$
$$= -\rho\sigma_{\text{ext}}aw_l\psi_l(z). \quad (4.34)$$

where we twice used the normalization from eqn. (4.31). Finally, the term on the right-hand-side becomes

$$\int_{-1}^{1} \sum_{l=0}^{\infty} \frac{2l+1}{2}s_l(z)P_l(\mu)P_n(\mu)d\mu = s_l(z). \qquad (4.35)$$

Adding eqns. (4.32), (4.33), (4.34) and (4.35) we get

$$\frac{l+1}{2l+1}\frac{d\psi_{l+1}}{dz} + \frac{l}{2l+1}\frac{d\psi_{l-1}}{dz} + \rho\sigma_{\text{ext}}\psi_l(z) - \rho\sigma_{\text{ext}}aw_l\psi_l(z) = s_l(z). \qquad (4.36)$$

We multiply eqn. (4.36) with $(2l+1)$ to get the final expression,

$$(l+1)\frac{d\psi_{l+1}}{dz} + l\frac{d\psi_{l-1}}{dz} + (2l+1)(1-aw_l)\rho\sigma_{\text{ext}}\psi_l(z) = (2l+1)s_l(z). \qquad (4.37)$$

4.2.2 Plane waves as source

We use plane waves as source in our derivations. For plane waves parallel to z-direction, I_{ri} is [1]

$$I_{\text{ri}}(\mathbf{r}, \hat{\mathbf{s}}) = F_0 e^{-\rho\sigma_{\text{ext}}z}\delta(\hat{\mathbf{s}} - \hat{\mathbf{s}}_z), \qquad (4.38)$$

where $\hat{\mathbf{s}}_{\mathbf{z}}$ is aligned with the z-axis. Eqn. (4.15) now becomes

$$\epsilon_{\text{ri}}(z, \mu) = \rho\sigma_{\text{ext}}a \int_{-1}^{1} F_0 e^{-\rho\sigma_{\text{ext}}z}\delta(\mu' - \mu_z) \sum_{l=0}^{\infty} \frac{2l+1}{2}w_l P_l(\mu)P_l(\mu')d\mu'. \quad (4.39)$$

We multiply eqn. (4.39) with $P_n(\mu)$ and integrate over 2π to employ the orthonormality property of the Legendre polynomials, given in eqn. (4.31), to obtain

$$
\int_{-1}^{1} \epsilon_{\text{ri}}(z,\mu)P_n(\mu)d\mu
$$

$$
= \rho\sigma_{\text{ext}}a \int_{-1}^{1} P_n(\mu) \int_{-1}^{1} F_0 e^{-\rho\sigma_{\text{ext}}z}\delta(\mu'-\mu_z)\sum_{l=0}^{\infty}\frac{2l+1}{2}w_l P_l(\mu)P_l(\mu')d\mu'd\mu
$$

$$
= \rho\sigma_{\text{ext}}a \int_{-1}^{1} F_0 e^{-\rho\sigma_{\text{ext}}z}\delta(\mu'-\mu_z))w_l P_l(\mu')d\mu'
$$

$$
= \rho\sigma_{\text{ext}}aF_0 e^{-\rho\sigma_{\text{ext}}z}w_l \int_{-1}^{1} \delta(\mu'-\mu_z)P_l(\mu')d\mu'
$$

$$
= F_0\rho\sigma_{\text{ext}}aw_l e^{-\rho\sigma_{\text{ext}}z}.
$$

$$(4.40)$$

We acquire the expression for $s_l(z)$ by expanding the term on the left-hand side of eqn. (4.40)

$$
\int_{-1}^{1}\sum_{l=0}^{\infty}\frac{2l+1}{2}s_l(z)P_l(\mu)P_n(\mu)d\mu = F_0\rho\sigma_{\text{ext}}aw_l e^{-\rho\sigma_{\text{ext}}z}
$$

$$
s_l(z) = F_0\rho\sigma_{\text{ext}}aw_l e^{-\rho\sigma_{\text{ext}}z}.
$$

$$(4.41)$$

Therefore, for plane waves as light source, our final expression (eqn.(4.37)) becomes

$$
(l+1)\frac{d\psi_{l+1}}{dz}+l\frac{d\psi_{l-1}}{dz}+(2l+1)(1-aw_l)\rho\sigma_{\text{ext}}\psi_l(z) = (2l+1)F_0\rho\sigma_{\text{ext}}aw_l e^{-\rho\sigma_{\text{ext}}z}.
$$

$$(4.42)$$

Eqn. (4.42) is an infinite set of coupled differential equations that describe the propagation of the intensity of light in the scattering medium. To solve this system of differential equations, we limit the expansion to order N. An odd [1] positive integer N is chosen with

$$
\psi_{-1}(z) = 0,
$$
$$
N < l < \infty \implies \psi_l(z) = 0.
$$

$$(4.43)$$

Thus, we get a set of $N+1$ differential equations to solve, as l only takes values $l = 0, 1, ..., N$.

4.2.3 P_1 and diffusion approximations

The 1st order P_N approximation is called, unsurprisingly, the P_1 approximation. In this case the system of two coupled first order differential equations can be transformed to one second order differential equation. This second order

---

[1]Odd positive integers are chosen for N since odd order approximations are known to be more accurate than even orders, as in the latter the angular integrands are discontinuous [77].

differential equation is equivalent to the steady state of the well known diffusion equation [82, 104, 115, 116]. The steady state diffusion equation for the average diffuse intensity in the case of plane wave incident upon a slab is given as [1]

$$\frac{d^2 U_{\text{diff}}(z)}{dz^2} - \kappa_{\text{d}}^2 U_{\text{diff}}(z) = -Q e^{-\rho\sigma_{\text{ext}}z}, \tag{4.44}$$

where the average intensity $U_{\text{diff}}(z)$ is defined in eqn. (4.9) and the prefactors are defined as

$$\kappa_{\text{d}}^2 \equiv 3(\rho\sigma_{\text{abs}})(\rho\sigma_{\text{tr}}), \tag{4.45}$$

$$Q \equiv (3\rho\sigma_{\text{scat}}\rho\sigma_{\text{tr}} + 3\rho\sigma_{\text{scat}}\rho\sigma_{\text{ext}}g)\left(\frac{F_0}{4\pi}\right), \tag{4.46}$$

$$g \equiv \frac{\left(\int_{4\pi} p(\hat{\mathbf{s}}, \hat{\mathbf{s}}')(\hat{\mathbf{s}} \cdot \hat{\mathbf{s}}')d\hat{\mathbf{s}}'\right)}{\left(\int_{4\pi} p(\hat{\mathbf{s}}, \hat{\mathbf{s}}')d\hat{\mathbf{s}}'\right)}. \tag{4.47}$$

Here, σ_{tr} is the transport cross-section that is equal to the sum of the scattering and absorption cross-sections, where the scattering is weighted by the anisotropy; yielding

$$\sigma_{\text{tr}} = \sigma_{\text{scat}}(1 - g) + \sigma_{\text{abs}}. \tag{4.48}$$

In the P_1 approximation, we solve eqn. (4.42) with $l = 0, 1$ to get

$$l = 0 \Rightarrow \frac{d\psi_1(z)}{dz} + (1 - aw_0)\rho\sigma_{\text{ext}}\psi_0(z) = F_0\rho\sigma_{\text{ext}}aw_0 e^{-\rho\sigma_{\text{ext}}z}, \tag{4.49}$$

$$l = 1 \Rightarrow \frac{d\psi_0(z)}{dz} + 3(1 - aw_1)\rho\sigma_{\text{ext}}\psi_1(z) = 3F_0\rho\sigma_{\text{ext}}aw_1 e^{-\rho\sigma_{\text{ext}}z}, \tag{4.50}$$

Using the moments of the Henyey-Greenstein phase function given in eqn. (4.27), we have explicitly

$$\begin{aligned} w_0 &= 1, \\ w_1 &= g. \end{aligned} \tag{4.51}$$

Using eqn. (4.51) we get from eqn. (4.50)

$$\begin{aligned} \frac{d\psi_0(z)}{dz} &+ 3(1 - ag)\rho\sigma_{\text{ext}}\psi_1(z) = 3F_0\rho\sigma_{\text{ext}}age^{-\rho\sigma_{\text{ext}}z}, \\ \Rightarrow \psi_1(z) &= \frac{3F_0\rho\sigma_{\text{ext}}age^{-\rho\sigma_{\text{ext}}z} - \frac{d\psi_0(z)}{dz}}{3(1 - ag)\rho\sigma_{\text{ext}}}, \\ \Rightarrow \psi_1(z) &= \frac{3F_0\rho\sigma_{\text{scat}}ge^{-\rho\sigma_{\text{ext}}z} - \frac{d\psi_0(z)}{dz}}{3\rho\sigma_{\text{tr}}}. \end{aligned} \tag{4.52}$$

Substituting this expression for ψ_1 into its derivative in eqn. (4.49) we get

$$\left(\frac{-3F_0\rho\sigma_{\text{ext}}\rho\sigma_{\text{scat}}ge^{-\rho\sigma_{\text{ext}}z} - \frac{d^2\psi_0(z)}{dz^2}}{3\rho\sigma_{\text{tr}}}\right) + \rho\sigma_{\text{abs}}\psi_0(z) = F_0\rho\sigma_{\text{ext}}ae^{-\rho\sigma_{\text{ext}}z},$$

$$\Rightarrow \frac{d^2\psi_0(z)}{dz^2} + 3F_0\rho\sigma_{\text{ext}}\rho\sigma_{\text{scat}}ge^{-\rho\sigma_{\text{ext}}z} - 3\rho\sigma_{\text{tr}}\rho\sigma_{\text{abs}}\psi_0(z) = -3F_0\rho\sigma_{\text{tr}}\rho\sigma_{\text{scat}}e^{-\rho\sigma_{\text{ext}}z},$$

$$\Rightarrow \frac{d^2\psi_0(z)}{dz^2} - 3\rho\sigma_{\text{tr}}\rho\sigma_{\text{abs}}\psi_0(z) = -\left(3\rho\sigma_{\text{tr}}\rho\sigma_{\text{scat}} + 3\rho\sigma_{\text{scat}}\rho\sigma_{\text{ext}}g\right)F_0e^{-\rho\sigma_{\text{ext}}z}. \tag{4.53}$$

Using coefficients κ_{d}^2 in eqn. (4.45) and Q in eqn. (4.46) this expression can be simplified as

$$\frac{d^2\psi_0(z)}{dz^2} - \kappa_{\text{d}}^2\psi_0(z) = -(4\pi)Qe^{-\rho\sigma_{\text{ext}}z}. \tag{4.54}$$

Using the definition of the coefficient ψ_l in eqn. (4.20), we get ψ_0 equals

$$\psi_0(z) = \int_{-1}^{1} I_{\text{diff}}(z,\mu)d\mu. \tag{4.55}$$

Since eqn. (4.55) is essentially the same as eqn. (4.9), we identify that ψ_0 is proportional to the energy density and average intensity:

$$U_{\text{diff}}(z) = \frac{1}{4\pi}\psi_0(z). \tag{4.56}$$

Thus, when we multiply eqn. (4.54) with $\frac{1}{4\pi}$ we get the diffusion equation

$$\frac{1}{4\pi}\frac{d^2\psi_0(z)}{dz^2} - \kappa_{\text{d}}^2\frac{1}{4\pi}\psi_0(z) = -Qe^{-\rho\sigma_{\text{ext}}z}. \tag{4.57}$$

4.3 Solving the P_N approximation

To solve higher order P_N approximations, we follow the method used in references [37, 47, 69]. We first demonstrate the method for P_1 approximation, and then expand it to P_3 approximation. Finally, we discuss the $P_3 + \delta E(4)$ approximation, which is a correction to P_3 approximation for the forward direction.

4.3.1 P_1 approximation

We start with a slight modification to eqns. (4.49) and (4.50) by writing them as

$$l = 0 \Rightarrow \frac{d\psi_1(z)}{dz} + \gamma_0\psi_0(z) = F_0\rho\sigma_{\text{ext}}aw_0e^{-\rho\sigma_{\text{ext}}z}, \tag{4.58}$$

$$l = 1 \Rightarrow \frac{d\psi_0(z)}{dz} + \gamma_1\psi_1(z) = 3F_0\rho\sigma_{\text{ext}}aw_1e^{-\rho\sigma_{\text{ext}}z}, \tag{4.59}$$

where we define

$$\gamma_0 \equiv (1 - aw_0)\rho\sigma_{\text{ext}},$$
$$\gamma_1 \equiv 3(1 - aw_1)\rho\sigma_{\text{ext}}. \tag{4.60}$$

Eqns. (4.58) and (4.59) have two types of solutions: Homogeneous and particular solutions, where the full solution is the sum of the two. The particular solution is of the form

$$\psi_{l_{\text{pt}}}(z) = G_l e^{-\rho\sigma_{\text{ext}}z}, \tag{4.61}$$

so we get

$$\psi_{0_{\text{pt}}}(z) = G_0 e^{-\rho\sigma_{\text{ext}}z},$$
$$\psi_{1_{\text{pt}}}(z) = G_1 e^{-\rho\sigma_{\text{ext}}z}. \tag{4.62}$$

Using the particular solution, we solve eqns. (4.58) and (4.59), and get

$$G_0 = \frac{\rho\sigma_{\text{ext}}aF_0(\gamma_1 w_0 + 3\rho\sigma_{\text{ext}}w_1)}{\gamma_0\gamma_1 - \rho^2\sigma_{\text{ext}}^2},$$
$$G_1 = \frac{\rho\sigma_{\text{ext}}aF_0(3\gamma_0 w_1 + \rho\sigma_{\text{ext}}w_0)}{\gamma_0\gamma_1 - \rho^2\sigma_{\text{ext}}^2}. \tag{4.63}$$

For the homogeneous solution, we take the right side of eqns. (4.58) and (4.59) to be 0, which gives

$$l = 0 \Rightarrow \frac{d\psi_1(z)}{dz} + \gamma_0\psi_0(z) = 0, \tag{4.64}$$

$$l = 1 \Rightarrow \frac{d\psi_0(z)}{dz} + \gamma_1\psi_1(z) = 0. \tag{4.65}$$

The homogeneous solution is of the form

$$\psi_{l_{\text{h}}} = H_{li}C_i e^{\lambda_i z}. \tag{4.66}$$

For the P_1 approximation, we take $i = 1, 2$ and $l = 0, 1$. Here C_1 and C_2 are integration constants, that will be calculated using suitable boundary conditions. To find H_{li}, we neglect them for now, and we set $H_{0i} = 1$ to insert it in eqn. (4.64). We get

$$\lambda_i H_{1i} + \gamma_0 H_{0i} = 0,$$
$$H_{1i} = -\frac{\gamma_0}{\lambda_i}. \tag{4.67}$$

Substituting H_{li} values to eqn. (4.65) gives

$$\lambda_i - \frac{\gamma_1\gamma_0}{\lambda_i} = 0, \tag{4.68}$$

so we get

$$\lambda_1 = \sqrt{\gamma_1\gamma_0},$$
$$\lambda_2 = -\sqrt{\gamma_1\gamma_0},$$
$$H_{01} = 1,$$
$$H_{02} = 1, \qquad\qquad (4.69)$$
$$H_{11} = -\frac{\gamma_0}{\lambda_1},$$
$$H_{12} = -\frac{\gamma_0}{\lambda_2},$$

and the homogeneous solution for the P_1 approximation is

$$\psi_{0_h}(z) = H_{01}C_1 e^{\lambda_1 z} + H_{02}C_2 e^{\lambda_2 z}, \qquad\qquad (4.70)$$

$$\psi_{1_h}(z) = H_{11}C_1 e^{\lambda_1 z} + H_{12}C_2 e^{\lambda_2 z}. \qquad\qquad (4.71)$$

We get the full solution of the P_1 approximation by summing the particular and homogeneous solutions, that is

$$\psi_0(z) = H_{01}C_1 e^{\lambda_1 z} + H_{02}C_2 e^{\lambda_2 z} + G_0 e^{-\rho\sigma_{\text{ext}}z}, \qquad\qquad (4.72)$$

$$\psi_1(z) = H_{11}C_1 e^{\lambda_1 z} + H_{12}C_2 e^{\lambda_2 z} + G_1 e^{-\rho\sigma_{\text{ext}}z}. \qquad\qquad (4.73)$$

Now we apply Marshak type boundary conditions [117] to these equations. The boundary conditions assume that on the boundaries, no diffuse light enters the scattering medium from the surrounding medium outside. When the refractive indices of the media inside and outside does not match, the total diffuse flux at the boundary directed into the medium is the part of the outwardly directed flux that is reflected by the surface [37, 69, 70, 74, 104]. This conservation law results in two boundary conditions

$$\int_0^1 I_{\text{diff}}(0,\mu)P_l(\mu)d\mu = \int_0^1 R(\mu)I_{\text{diff}}(0,-\mu)P_l(\mu)d\mu, \qquad\qquad (4.74)$$

$$\int_{-1}^0 I_{\text{diff}}(L,-\mu)R(-\mu)P_l(\mu)d\mu = \int_{-1}^0 I_{\text{diff}}(L,\mu)P_l(\mu)d\mu, \qquad\qquad (4.75)$$

where L is the sample thickness and $l = 1$. $R(\mu)$ is the specular Fresnel reflection function for unpolarized light, given by

$$R_s = \left| \frac{n_1\mu - n_2\sqrt{1 - \left(\frac{n_1}{n_2}\sqrt{1-\mu^2}\right)^2}}{n_1\mu + n_2\sqrt{1 - \left(\frac{n_1}{n_2}\sqrt{1-\mu^2}\right)^2}} \right|^2,$$

$$R_p = \left| \frac{n_1\sqrt{1 - \left(\frac{n_1}{n_2}\sqrt{1-\mu^2}\right)^2} - n_2\mu}{n_1\sqrt{1 - \left(\frac{n_1}{n_2}\sqrt{1-\mu^2}\right)^2} + n_2\mu} \right|^2, \qquad\qquad (4.76)$$

$$R(\mu) = \frac{(R_s + R_p)}{2}.$$

After substituting the expression for intensity in eqn. (4.19) into eqns (4.74) and (4.75), and putting $l = 0, 1$ for the P1 approximation, we get

$$\psi_0(0)J_0(\mu) + 3\psi_1(0)J_1(\mu) = 0, \tag{4.77}$$

$$\psi_0(L)D_0(\mu) + 3\psi_1(L)D_1(\mu) = 0, \tag{4.78}$$

where

$$
\begin{aligned}
J_0(\mu) &= \int_0^1 \mu(1 - R(\mu))d\mu, \\
J_1(\mu) &= \int_0^1 \mu^2(1 + R(\mu))d\mu, \\
D_0 &= -J_0, \\
D_1 &= J_1.
\end{aligned}
\tag{4.79}
$$

To find the integration constants C_1 and C_2, we submit eqns. (4.72) and (4.73) into eqns. (4.77) and (4.78)

$$J_0(\mu)\left(H_{01}C_1 + H_{02}C_2 + G_0\right) + 3J_1(\mu)\left(H_{11}C_1 + H_{12}C_2 + G_1\right) = 0, \tag{4.80}$$

$$
\begin{aligned}
&D_0(\mu)\left(H_{01}C_1 e^{\lambda_1 L} + H_{02}C_2 e^{\lambda_2 L} + G_0 e^{-\rho\sigma_{\text{ext}}L}\right) \\
&+ 3D_1(\mu)\left(H_{11}C_1 e^{\lambda_1 L} + H_{12}C_2 e^{\lambda_2 L} + G_1 e^{-\rho\sigma_{\text{ext}}L}\right) = 0.
\end{aligned}
\tag{4.81}
$$

Solving these two equations for C1 and C2 gives the integration constants. We do not write them here because the resulting expressions are rather long. Now that we have everything, we can calculate ψ_0 to get the diffuse average intensity $U_{\text{diff}}(z)$ as in eqn. (4.56), and ψ_1 for the diffuse flux

$$F_{\text{diff}}(z) = \psi_1(z). \tag{4.82}$$

4.3.2 P_3 **approximation**

For the P_3 approximation, we must take $l = 0, 1, 2, 3$ in eqn. (4.42) and we get the four differential equations

$$l = 0 \Rightarrow \ \frac{d\psi_1(z)}{dz} + \gamma_0\psi_0(z) = F_0\rho\sigma_{\text{ext}}aw_0 e^{-\rho\sigma_{\text{ext}}z}, \tag{4.83}$$

$$l = 1 \Rightarrow \ 2\frac{d\psi_2(z)}{dz} + \frac{d\psi_0(z)}{dz} + \gamma_1\psi_1(z) = 3F_0\rho\sigma_{\text{ext}}aw_1 e^{-\rho\sigma_{\text{ext}}z}, \tag{4.84}$$

$$l = 2 \Rightarrow \ 3\frac{d\psi_3(z)}{dz} + 2\frac{d\psi_1(z)}{dz} + \gamma_2\psi_2(z) = 5F_0\rho\sigma_{\text{ext}}aw_2 e^{-\rho\sigma_{\text{ext}}z}, \tag{4.85}$$

$$l = 3 \Rightarrow \ 3\frac{d\psi_2(z)}{dz} + \gamma_3\psi_3(z) = 7F_0\rho\sigma_{\text{ext}}aw_3 e^{-\rho\sigma_{\text{ext}}z}, \tag{4.86}$$

where

$$
\begin{aligned}
\gamma_0 &= (1 - aw_0)\rho\sigma_{\text{ext}}, \\
\gamma_1 &= 3(1 - aw_1)\rho\sigma_{\text{ext}}, \\
\gamma_2 &= 5(1 - aw_2)\rho\sigma_{\text{ext}}, \\
\gamma_3 &= 7(1 - aw_3)\rho\sigma_{\text{ext}}.
\end{aligned}
\tag{4.87}
$$

We again use eqn. (4.27) to get the first four moments of the phase function

$$
\begin{aligned}
w_0 &= 1, \\
w_1 &= g, \\
w_2 &= g^2, \\
w_3 &= g^3,
\end{aligned}
\tag{4.88}
$$

The particular solution in eqn. (4.61) gives

$$
\begin{aligned}
\psi_{0_{\text{pt}}}(z) &= G_0 e^{-\rho\sigma_{\text{ext}}z}, \\
\psi_{1_{\text{pt}}}(z) &= G_1 e^{-\rho\sigma_{\text{ext}}z}, \\
\psi_{2_{\text{pt}}}(z) &= G_2 e^{-\rho\sigma_{\text{ext}}z}, \\
\psi_{3_{\text{pt}}}(z) &= G_3 e^{-\rho\sigma_{\text{ext}}z}.
\end{aligned}
\tag{4.89}
$$

Using these particular solutions, we solve eqns. (4.83-4.86) and get the prefactors G_l. They are rather long so we won't write them here.

For the homogeneous solution, we again set the right-hand side of eqns. (4.83-4.86) to be zero and the solution is again of the form given in eqn. (4.66). For the P_3 approximation we take $i = 1, 2, 3, 4$ and $l = 0, 1, 2, 3$, and get

$$
\gamma_0 H_{0i} + \lambda_i H_{1i} = 0, \tag{4.90}
$$

$$
\lambda_i H_{0i} + \gamma_1 H_{1i} + 2\lambda_i H_{2i} = 0, \tag{4.91}
$$

$$
2\lambda_i H_{1i} + \gamma_2 H_{2i} + 3\lambda_i H_{3i} = 0, \tag{4.92}
$$

$$
3\lambda_i H_{2i} + \gamma_3 H_{3i} = 0. \tag{4.93}
$$

We set $H_{0i} = 1$ and put it in eqn. (4.90) and get

$$
\begin{aligned}
\lambda_i H_{1i} + \gamma_0 H_{0i} &= 0, \\
H_{1i} &= -\frac{\gamma_0}{\lambda_i}.
\end{aligned}
\tag{4.94}
$$

Substituting H_{1i} into eqn. (4.91) gives

$$
\begin{aligned}
\lambda_i - \frac{\gamma_1\gamma_0}{\lambda_i} + 2\lambda_i H_{2i} &= 0, \\
H_{2i} &= \frac{\gamma_0\gamma_1 - \lambda_i^2}{2\lambda_i^2}.
\end{aligned}
\tag{4.95}
$$

Similarly, we put H_{2i} to eqn. (4.92) and get

$$-2\lambda_i \frac{\gamma_0}{\lambda_i} + \gamma_2 \frac{\gamma_0\gamma_1 - \lambda_i^2}{2\lambda_i^2} + 3\lambda_i H_{3i} = 0,$$

$$H_{3i} = \frac{-\gamma_0\gamma_1\gamma_2 + 4\gamma_0\lambda_i^2 + \gamma_2\lambda_i^2}{6\lambda_i^3}. \tag{4.96}$$

Finally, putting all H_{li} in eqn. (4.93) gives λ_i values, however, they are also rather long and won't be given here. Now we have all the values needed, except C_i to write the coefficients for the final solution,

$$\psi_0(z) = H_{01}C_1 e^{\lambda_1 z} + H_{02}C_2 e^{\lambda_2 z} + H_{03}C_3 e^{\lambda_3 z} + H_{04}C_4 e^{\lambda_4 z} + G_0 e^{-\rho\sigma_{\text{ext}} z}, \tag{4.97}$$

$$\psi_1(z) = H_{11}C_1 e^{\lambda_1 z} + H_{12}C_2 e^{\lambda_2 z} + H_{13}C_3 e^{\lambda_3 z} + H_{14}C_4 e^{\lambda_4 z} + G_1 e^{-\rho\sigma_{\text{ext}} z}, \tag{4.98}$$

$$\psi_2(z) = H_{21}C_1 e^{\lambda_1 z} + H_{22}C_2 e^{\lambda_2 z} + H_{23}C_3 e^{\lambda_3 z} + H_{24}C_4 e^{\lambda_4 z} + G_2 e^{-\rho\sigma_{\text{ext}} z}, \tag{4.99}$$

$$\psi_3(z) = H_{31}C_1 e^{\lambda_1 z} + H_{32}C_2 e^{\lambda_2 z} + H_{33}C_3 e^{\lambda_3 z} + H_{34}C_4 e^{\lambda_4 z} + G_3 e^{-\rho\sigma_{\text{ext}} z}. \tag{4.100}$$

Now, we again apply the boundary conditions given in eqns. (4.74-4.75). For P_1, we set $l = 1$ to them and get 2 equations. To solve the P_3 approximation, we need 2 more equations, which we obtain by setting $l = 3$ in eqns. (4.74-4.75). This gives us the four equations below as boundary conditions

$$\psi_0(0)J_0(\mu) + 3\psi_1(0)J_1(\mu) + 5\psi_2(0)J_2(\mu) + 7\psi_3(0)J_3(\mu) = 0, \tag{4.101}$$

$$\psi_0(L)D_0(\mu) + 3\psi_1(L)D_1(\mu) + 5\psi_2(L)D_2(\mu) + 7\psi_3(L)D_3(\mu) = 0, \tag{4.102}$$

$$\psi_0(0)E_0(\mu) + 3\psi_1(0)E_1(\mu) + 5\psi_2(0)E_2(\mu) + 7\psi_3(0)E_3(\mu) = 0, \tag{4.103}$$

$$\psi_0(L)K_0(\mu) + 3\psi_1(L)K_1(\mu) + 5\psi_2(L)K_2(\mu) + 7\psi_3(L)K_3(\mu) = 0, \tag{4.104}$$

where

$$J_0(\mu) = \int_0^1 \mu(1 - R(\mu))d\mu,$$

$$J_1(\mu) = \int_0^1 \mu^2(1 + R(\mu))d\mu,$$

$$J_2(\mu) = \int_0^1 \mu\frac{3\mu^2 - 1}{2}(1 - R(\mu))d\mu,$$

$$J_3(\mu) = \int_0^1 \mu\frac{5\mu^3 - 3\mu}{2}(1 + R(\mu))d\mu,$$

$$D_0 = -J_0,$$

$$D_1 = J_1,$$

$$D_2 = -J_2,$$

$$D_3 = J_3,$$

$$E_0(\mu) = \int_0^1 \frac{5\mu^3 - 3\mu}{2}(1 - R(\mu))d\mu,$$

$$E_1(\mu) = \int_0^1 \mu\frac{5\mu^3 - 3\mu}{2}(1 + R(\mu))d\mu,$$

$$E_2(\mu) = \int_0^1 \frac{5\mu^3 - 3\mu}{2}\frac{3\mu^2 - 1}{2}(1 - R(\mu))d\mu,$$

$$E_3(\mu) = \int_0^1 \frac{5\mu^3 - 3\mu}{2}\frac{5\mu^3 - 3\mu}{2}(1 + R(\mu))d\mu,$$

$$K_0 = -E_0,$$

$$K_1 = E_1,$$

$$K_2 = -E_2,$$

$$K_3 = E_3.$$

(4.105)

When we substitute the eqns. (4.97-4.100) into the boundary conditions given in eqns. (4.101-4.104) and solve for all C_i, we get the C_i coefficients. Again, these are extremely long results and are not included here.

We now have everything we need to calculate the diffuse average intensity $U_{\text{diff}}(z)$ from eqn. (4.56), and the diffuse flux $F_{\text{diff}}(z)$ from eqn. (4.82). The total transmission TT is given as

$$TT = \frac{\psi_1(L) + F_0 e^{-\rho\sigma_{\text{ext}}L}}{F_0}, \tag{4.106}$$

and the total reflection TR is

$$TR = \frac{-\psi_1(0)}{F_0} \tag{4.107}$$

4.3.3 $P_3 + \delta E(4)$ **approximation**

When the order N of the approximation is chosen, the higher-order terms of the expansions are truncated. Therefore, the implementations of higher-order approximations are expected to be more accurate, especially when it comes to a photonic scattering slab with anisotropic scattering. The $P_N + \delta E(N+1)$ approximation adds a delta function to the Henyey-Greenstein phase function to compensate for the loss in extreme forward scattering due to truncated higher-order terms [69, 105]. This means the expansion of Henyey-Greenstein phase function $p_{H-G}(\mu, \mu')$ given in eqn. (4.25) becomes

$$p_{\delta E(N+1)}(\mu, \mu') = (1 - f)p_{H-G}(\mu, \mu') + f\delta(\mu - \mu'), \qquad (4.108)$$

where

$$f = g^{N+1}. \qquad (4.109)$$

As the RTE and its moments keep their mathematical form, only the optical constants need to be modified as [37]:

$$
\begin{aligned}
\sigma'_{\text{scat}} &= (1 - f)\sigma_{\text{scat}} \; ; \\
(g')^n &= \frac{g^n - f}{1 - f} \; ; \\
a' &= \frac{\sigma'_{\text{scat}}}{\sigma_{\text{abs}} + \sigma'_{\text{scat}}}.
\end{aligned}
\qquad (4.110)
$$

The addition of a strongly forward peaked delta function does not result in any physical changes, as photons that maintain their direction of propagation are not scattered [69]. However, mathematically, this modification leads to a more forward-directed average scattering.

By using the phase function $p_{\delta E(N+1)}$, replacing the original optical constants with the ones from eqn. (4.110) and taking the order $N = 3$ in the method explained in subsection 4.3.2, the solution for the $P_3 + \delta E(4)$ approximation to the RTE is found. In other words, only the optical constants in eqns. (4.83 - 4.89) are modified to obtain the solution. To avoid redundancy, we refrain from rewriting the modified equations in this context. The success of the $P_3 + \delta E(4)$ approximation is discussed in chapters 3 and 5.

4.4 Consideration of cuvette walls

In our experiments in chapter 5, the samples are microsphere suspensions in water, and they are held in quartz cuvettes during measurements. Therefore, for these samples the reflections from cuvette walls need to be considered in the boundary conditions of the models. The simple internal reflection scheme is shown in Fig. 4.5. Since the cuvette walls do not have any scatterers or significant absorption, we neglect the extinction in these regions and approach the problem by considering only the reflections from the interfaces. We define μ as the directional cosine of light coming from slab to the cuvette wall and μ_{cuv}

as the directional cosine of light coming from the cuvette wall towards the slab, where

$$\mu_{\mathrm{cuv}} = \sqrt{1 - \left(\frac{n_{\mathrm{slab}}}{n_{\mathrm{cuv}}}\sqrt{1-\mu^2}\right)^2}. \tag{4.111}$$
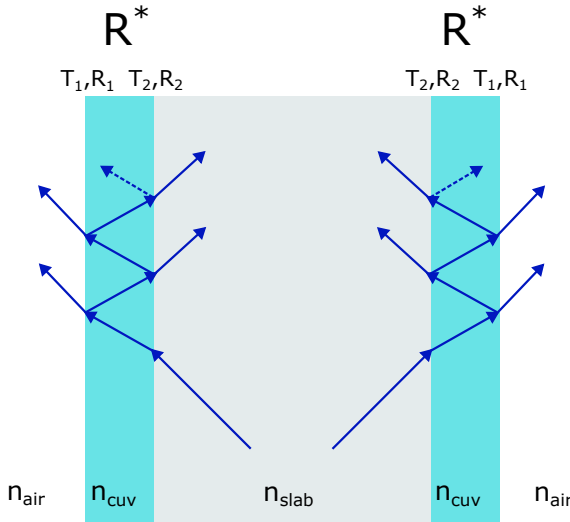

Figure 4.5: Cross-section of a slab with cuvette walls. The blue arrows represent light being reflected from and transmitted through the boundaries. The refractive indices of air, cuvette and slab media are n_{air}, n_{cuv} and n_{slab}, respectively. T_1 and R_1 are the Fresnel transmission and reflection coefficients for unpolarized light, for the air-cuvette interface. T_2 and R_2 are the Fresnel transmission and reflection coefficients for unpolarized light, for the slab-cuvette interface. R^* represents the combined Fresnel reflection coefficient of the boundaries.

Next, we define a Fresnel reflection coefficient $R^*(\mu)$, that combines the effect of the cuvette walls and reflections from the slab-cuvette and cuvette-air interfaces, as

$$\begin{aligned}
R^*(\mu) &\equiv R_2(\mu) + T_2^2(\mu)R_1(\mu_{\mathrm{cuv}})\sum_{i=0}^{\infty}(R_2(\mu)R_1(\mu_{\mathrm{cuv}}))^i \\
&= R_2(\mu) + T_2^2(\mu)R_1(\mu_{\mathrm{cuv}})\frac{1}{1-R_2(\mu)R_1(\mu_{\mathrm{cuv}})},
\end{aligned} \tag{4.112}$$

where the reflection coefficient of air-cuvette interface $R_1(\mu_{\text{cuv}})$ is

$$R_{1\text{s}}(\mu_{\text{cuv}}) = \left| \frac{n_{\text{cuv}}\mu_{\text{cuv}} - n_{\text{air}}\sqrt{1 - \left(\frac{n_{\text{cuv}}}{n_{\text{air}}}\sqrt{1 - \mu_{\text{cuv}}^2}\right)^2}}{n_{\text{cuv}}\mu_{\text{cuv}} + n_{\text{air}}\sqrt{1 - \left(\frac{n_{\text{cuv}}}{n_{\text{air}}}\sqrt{1 - \mu_{\text{cuv}}^2}\right)^2}} \right|^2,$$

$$R_{1\text{p}}(\mu_{\text{cuv}}) = \left| \frac{n_{\text{cuv}}\sqrt{1 - \left(\frac{n_{\text{cuv}}}{n_{\text{air}}}\sqrt{1 - \mu_{\text{cuv}}^2}\right)^2} - n_{\text{air}}\mu_{\text{cuv}}}{n_{\text{cuv}}\sqrt{1 - \left(\frac{n_{\text{cuv}}}{n_{\text{air}}}\sqrt{1 - \mu_{\text{cuv}}^2}\right)^2} + n_{\text{air}}\mu_{\text{cuv}}} \right|^2,$$

$$(4.113)$$

$$R_1(\mu_{\text{cuv}}) = \frac{(R_{1\text{s}} + R_{1\text{p}})}{2},$$

the reflection coefficient of slab-cuvette interface $R_{2(\mu)}$ is

$$R_{2\text{s}}(\mu) = \left| \frac{n_{\text{slab}}\mu - n_{\text{cuv}}\sqrt{1 - \left(\frac{n_{\text{slab}}}{n_{\text{cuv}}}\sqrt{1 - \mu^2}\right)^2}}{n_{\text{slab}}\mu + n_{\text{cuv}}\sqrt{1 - \left(\frac{n_{\text{slab}}}{n_{\text{cuv}}}\sqrt{1 - \mu^2}\right)^2}} \right|^2,$$

$$R_{2\text{p}}(\mu) = \left| \frac{n_{\text{slab}}\sqrt{1 - \left(\frac{n_{\text{slab}}}{n_{\text{cuv}}}\sqrt{1 - \mu^2}\right)^2} - n_{\text{cuv}}\mu}{n_{\text{cuv}}\sqrt{1 - \left(\frac{n_{\text{slab}}}{n_{\text{cuv}}}\sqrt{1 - \mu^2}\right)^2} + n_{\text{cuv}}\mu} \right|^2,$$

$$(4.114)$$

$$R_2(\mu) = \frac{(R_{2\text{s}}(\mu) + R_{2\text{p}}(\mu))}{2},$$

and the transmission coefficient of slab-cuvette interface $T_2(\mu)$ is

$$T_{2\text{s}}(\mu) = \left| \frac{2n_{\text{slab}}\mu}{n_{\text{slab}}\mu + n_{\text{cuv}}\mu_{\text{cuv}}} \right|^2,$$

$$T_{2\text{p}}(\mu) = \left| \frac{2n_{\text{slab}}\mu}{n_{\text{cuv}}\mu + n_{\text{slab}}\mu_{\text{cuv}}} \right|^2,$$

$$(4.115)$$

$$T_2(\mu) = \frac{(T_{2\text{s}} + T_{2\text{p}})}{2} \frac{n_{\text{cuv}}\mu_{\text{cuv}}}{n_{\text{slab}}\mu}.$$

The $R^*(\mu)$ in eqn. (4.112) is then substituted to eqns. (4.74) and (4.75) as the fresnel reflection coefficient, to include the effect of cuvette walls in the boundary conditions.

4.5 Internal reflection of the reduced intensity

The internal reflections of the reduced intensity I_{ri}, or the unscattered source, is not considered in the derivations given in the previous sections of this chapter.

However, the effect of these reflections is not negligible for the realistic samples with cuvette walls. Fig. 4.6 shows the simple scheme of the internal reflections of the reduced intensity that contribute to the total left flux F_{0L} at $z = 0$ with direction z, and the total right flux F_{0R} at $z = L$ with direction $-z$.
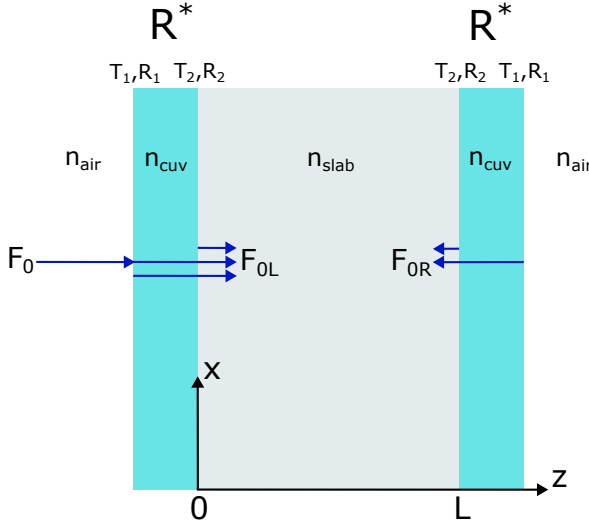
Figure 4.6: Cross-section of a slab with cuvette walls. The blue arrows represent the unscattered part of the incident flux F_0 being reflected from and transmitted through the boundaries. F_{0L} is the total flux that travels in z-direction, and F_{0R} is the total flux that travels in $-z$-direction. The refractive indices of air, cuvette and slab media are n_{air}, n_{cuv} and n_{slab}, respectively. T_1 and R_1 are the Fresnel transmission and reflection coefficients for unpolarized light, for the air-cuvette interface. T_2 and R_2 are the Fresnel transmission and reflection coefficients for unpolarized light, for the slab-cuvette interface. R^* represents the combined Fresnel reflection coefficient of the boundaries.

The reduced intensity I_{ri} in the slab medium for plane waves as source in eqn. (4.38) is re-written as

$$I_{ri}(\mathbf{r}, \hat{\mathbf{s}}) = F_{0L}e^{-\rho\sigma_{ext}z}\delta(\hat{\mu} - \hat{\mu}_z) + F_{0R}e^{-\rho\sigma_{ext}(L-z)}\delta(\hat{\mu} + \hat{\mu}_z) \qquad (4.116)$$

where μ_z is aligned with the z-axis, F_{0L} is

$$F_{0L} = F_0 T_1 T_2 \left(\sum_{i=0}^{\infty} (R_2 R_1)^i \right) \left(\sum_{k=0}^{\infty} \left(e^{-2\rho\sigma_{ext}L} R^{*2} \right)^k \right),$$

$$F_{0L} = F_0 T_1 T_2 \frac{1}{1 - (R_2 R_1)} \frac{1}{1 - (e^{-2\rho\sigma_{ext}L} R^{*2})}, \qquad (4.117)$$

and F_{0R} is

$$F_{0R} = F_0 T_1 T_2 e^{-\rho\sigma_{ext}L} R^* \left(\sum_{i=0}^{\infty} (R_2 R_1)^i \right) \left(\sum_{k=0}^{\infty} \left(e^{-2\rho\sigma_{ext}L} R^{*2} \right)^k \right),$$

$$F_{0R} = F_0 T_1 T_2 e^{-\rho\sigma_{ext}L} R^* \frac{1}{1-(R_2 R_1)} \frac{1}{1-(e^{-2\rho\sigma_{ext}L} R^{*2})}. \qquad (4.118)$$

Substituting eqn. (4.116) into eqn. (4.15) gives the lth moment of the source function $s_l(z)$ to

$$s_l(z) = (F_{0L} e^{-\rho\sigma_{ext}z} + (-1)^l F_{0R} e^{-\rho\sigma_{ext}(L-z)})\rho\sigma_{ext} a w_l, \qquad (4.119)$$

which changes eqn. (4.42) to

$$(l+1)\frac{d\psi_{l+1}}{dz} + l\frac{d\psi_{l-1}}{dz} + (2l+1)(1-aw_l)\rho\sigma_{ext}\psi_l(z) =$$
$$(2l+1)(F_{0L} e^{-\rho\sigma_{ext}z} + (-1)^l F_{0R} e^{-\rho\sigma_{ext}(L-z)})\rho\sigma_{ext} a w_l. \qquad (4.120)$$

Eqn. (4.120) is solved the same way as explained in section 4.3, with consideration of two separate sources with z and $-z$ directions and the boundary conditions including cuvette walls given in derived in section 4.4. To avoid redundancy, we refrain from repeating the derivations with these slight modifications.

4.6 Alternative phase functions

In this study, the Henyey-Greenstein and $\delta E(N+1)$ phase functions have been utilized. The literature reports several alternative phase functions, and the selection of an appropriate one is dependent on the knowledge of the optical properties of the scatterers. Optimized phase functions have been developed for specific cases, and these can provide better results compared to the commonly used phase functions.

Perhaps the most famous phase function is the Mie phase function. Gustav Mie showed an analytical solution to the electromagnetic field inside dielectric spheres subject to an incident planewave [12], from which a phase function can be constructed in the form of an expansion in series of Legendre polynomials [118]. This phase function is dependent on the refractive index of the sphere relative to the surrounding medium, and the size parameter x, that is the ratio of the circumference of the sphere to the wavelength of the light in the surrounding medium [7]

$$x = \frac{2\pi r}{\lambda}. \qquad (4.121)$$

Another famous description of scattering is done by Rayleigh [10], which is applicable for isotropically scattering spheres smaller than the size of the incident wavelength, that is $x \ll 1$.

An example for a phase function that is optimized for a specific case is the Fournier-Forand phase function [31], which is designed to describe light scattering

in oceans. This phase function approximates the particle size distributions in the oceans using an inverse power law called the Junge distribution [119]. With a few more assumptions, the Fournier-Forand phase function, with two parameters that determine the size distribution, and the refractive index of the scatterers, is derived. There is no analytic expression for the mean cosine or an analytical Legendre expansion for the Fournier-Forand phase function yet. This means numerical calculations are required, that are difficult due to the complex form of the phase function and the singularity it has for scattering angle $\theta = 0$.

Other alternatives include the Cornette-Shanks phase function [120] that describes scattering by small particles well, the Draine phase function [121] that aims to improve the Henyey-Greenstein phase function to better describe scattering by interstellar dust, and the Liu phase function [122] developed for strongly forward scattering biomedical media. These alternatives, usually introduce extra parameters and complexity to the phase function to better describe their specific cases and require more knowledge about the scatterers in the medium that light travels. In this study, the focus is on the simplest cases, and a relatively simple correction to Henyey-Greenstein by the $\delta E(N+1)$ is considered.

4.7 Summary

This chapter lays out the theoretical foundation of of chapters 3 and 5, starting with an explanation of key parameters in transport theory, such as specific intensity and energy density. The radiative transfer equation for a slab geometry is then derived and solved, utilizing the first and third-order P_N approximations, and a correction to the P_3 approximation for forward scattering is explored, which involves the incorporation of a delta function in the forward direction. Furthermore, to better represent the experiments in chapter 5, consideration of cuvette walls surrounding the slab for boundary conditions and the addition of internal reflections of the reduced intensity to the models are discussed. Finally, several alternative phase functions are discussed as examples, although they are out of the scope of this thesis.

5 Probing the position-dependent energy fluence rate in 3D scattering samples

5.1 Introduction

For numerous applications such as light emitting diodes (LEDs) [34, 44–47], oceanography [31–33, 35, 36], and biophysics [37–40] it is crucial to understand the light transport, hence, predict the position-dependent energy density, which is proportional to the position-dependent energy fluence rate. While Monte Carlo simulations are a powerful tool to study the energy distribution in scattering media [58–66], they come at the cost of extremely long computation times [67]. Analytical approximations to transport theory offer a much faster alternative, but they may not provide accurate results for samples that exhibit strong anisotropic scattering and absorption [98] (see Chapter 3).

Experimental observations of the position-dependent energy fluence rate in *real* scattering samples are essential to identify reliable methods to model the light transport in real devices. Such *in situ* and *in vitro* measurements of light transport have been widely used in various research areas, including aerosols [123, 124], light-emitting diodes (LEDs) [125], and photodynamic therapy (PDT) [22, 24, 126]

In Chapter 3, we studied different models of light transport, and presented their validity ranges. We are curious to see what happens *in real samples* in the $(a, g, b, \Delta n)$ parameter space where the analytic models breakdown. Naively one would solely trust Monte Carlo simulations, but it is important to note that even the most ideal simulation cannot fully replicate experimental observations. For instance, Monte Carlo simulations of light transport rely on input parameters such as scattering and absorption coefficients, which are typically interpreted from other experiments that carry additional assumptions and errors. Hence, accurate experimental measurements are considered superior to stand-alone simulations.

In this chapter, we report the experiments done in parameter ranges where most of the approximations fail, to find out what happens and how well models pertain. We present our experiments on the *in situ* detection of the position-dependent fluence rate $\Phi(z)$ in both absorbing and non-absorbing, anisotropically scattering samples. A schematic of the detection method is shown in Fig. 5.1, where a slab with spherical scatterers is illuminated from the (x, y) side by light with intensity $I_0(\nu_0)$. Light enters the sample and propagates inside, undergoing

scattering and absorption by the spheres. A probe in the form of a thin cylindrical capillary, filled with quantum dots, is utilized to detect the intensity at known positions inside the sample. When the light reaches the probe from any direction, it excites the quantum dots, which subsequently emit light at a lower frequency ν_e. Part of the re-emitted light is then collected from the top of the probe, and the position-dependent energy fluence rate is inferred from this measurement.
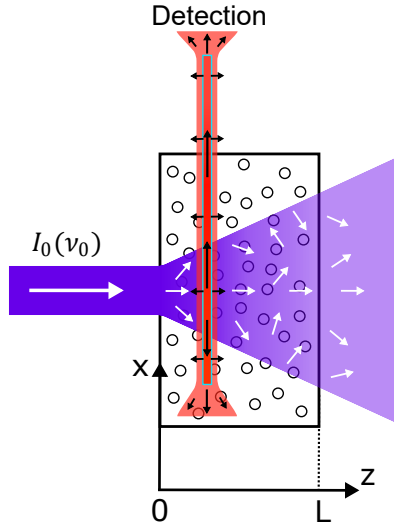
Figure 5.1: Cross-section of a slab with thickness L that contains a suspension of microspheres in water. A thin capillary filled with fluorescent reporters is inserted in the sample as a probe. The slab is illuminated from the side by light with intensity $I_0(\nu_0)$. The white arrows represent the direction of light with frequency ν_0, including both the diffuse and the unscattered parts. The black arrows represent the direction of emitted light with frequency ν_e. Fluorescent emission is detected from the top of the probe.

5.2 Experimental details

The experimental details of the position-dependent energy fluence rate measurements inside scattering samples are presented in this section. The experiments are conducted using samples that have strongly forward-scattering (anisotropy $g > 0.75$) and absorbing (albedo $a < 1$) scatterers, which lie within the parameter range where common analytical approximations fail, as shown in Figs. 3.3 and 3.4.

5.2.1 Sample preparation

Samples are prepared by diluting commercially-bought polystyrene microsphere suspensions, with a reported particle radii $r = 0.5 \pm 0.025$ μm. The microsphere suspensions used in our experiments are both plain and red-dyed

Polybead® Polystyrene Microspheres from Polysciences for undyed and dyed sphere suspensions, respectively. A buffer solution is produced by mixing Sodium dodecyl sulfate (SDS) surfactant (0.05%) with de-ionized (DI) water (99.95%). The samples with scatterers are then prepared by diluting their respective suspensions with the buffer solution. The use of SDS in the buffer solution served to prevent agglomeration and rapid sedimentation of the scatterers. The samples prepared with this buffer solution are stable for approximately 24 hours, after which sedimentation is observed. Prior to subsequent use in experiments, the samples are carefully agitated to re-disperse the sediment, with attention paid to prevent the introduction of air bubbles. Dyed sphere samples are labelled DS, and plain (undyed) sphere samples are US. The contents and scatterer concentrations of prepared samples are provided in Table 5.1, and a photograph of the samples are shown in Fig. 5.2.

Sample name	Contents	$\rho\,(\mathrm{mm}^{-3})$
Ref	99.95 $wt.\%$ DI water + 0.05 $wt.\%$ SDS	0
DS1	0.025% (w/v) dyed sphere + Ref	$(4.6\,\pm\,0.6)\times 10^5$
DS2	0.013% (w/v) dyed sphere + Ref	$(2.3\,\pm\,0.3)\times 10^5$
DS3	0.006% (w/v) dyed sphere + Ref	$(1.1\,\pm\,0.1)\times 10^5$
US1	0.026% (w/v) plain sphere + Ref	$(4.7\,\pm\,0.6)\times 10^5$
US2	0.013% (w/v) plain sphere + Ref	$(2.4\,\pm\,0.3)\times 10^5$
US3	0.007% (w/v) plain sphere + Ref	$(1.2\,\pm\,0.2)\times 10^5$

Table 5.1: Contents and the number density of scatterers ρ of the prepared samples. The percentages of spheres are adjusted from the information provided by Polyscience about their products. DS are red-dyed microsphere samples, and US are undyed microsphere samples.
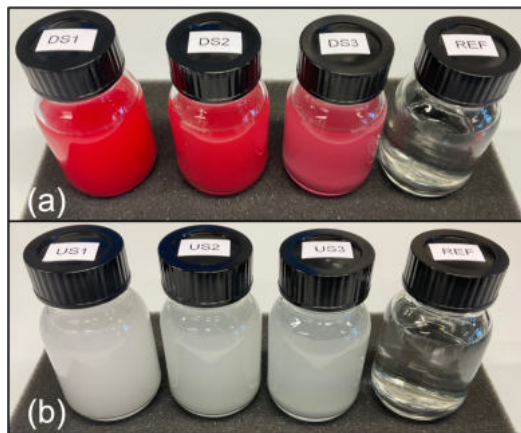
Figure 5.2: Photographs of the prepared samples with different densities of (a) red-dyed scatterers, (b) undyed scatterers. The scatterers are polystyrene spheres with $(1.00\,\pm\,0.05)\,\mu$m diameter.

5.2.2 Choice of the light source

Extinction spectra of the diluted dyed microsphere suspension with a scatterer number density of $\rho = (4.6 \pm 0.6) \times 10^4$ mm^{-3} were measured using a UV-Vis spectrometer (Perkin Elmer Lambda 850, MNF chair at MESA+). The measured spectrum is presented in Fig. 5.3. The sphere suspension is diluted with DI water, thus, the reference used in this UV-Vis measurement is also DI water. The extinction peak of the microspheres in the visible range is observed to be around 400 nm wavelength. Therefore, we chose a Thorlabs NPL41B nanosecond laser with a peak wavelength of $\lambda = 408.5$ nm as the light source in our experiments, to minimize the albedo of the scatterers.
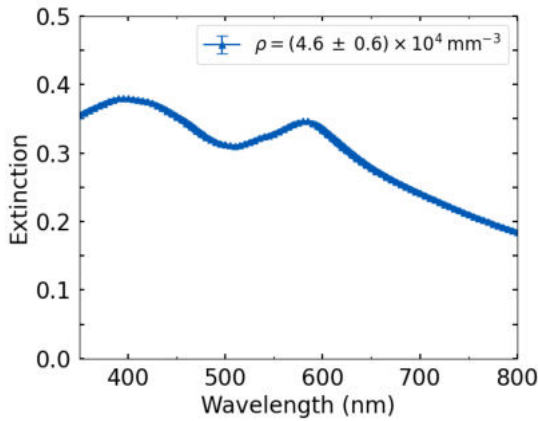
Figure 5.3: Measured extinction of dyed microsphere suspension with number density $\rho = (4.6 \pm 0.6) \times 10^4$ mm^{-3}. The sample is prepared by diluting the commercially bought spheres with DI-water and does not include any surfactants to prevent agglomeration of spheres.

5.2.3 Preparation of the probe

The concept of a probe filled with fluorescent reporters is depicted in Fig. 5.1. To realize this concept, a cylindrical, quartz capillary with 10 cm length (CM Scientific, CV1017Q-100), an outer diameter of $170\,\mu$m and an inner diameter of $100\,\mu$m is utilized. A capillary is filled with quantum dots suspended in decane (Thermo Fisher Qdot$^{\text{TM}}$ 655 ITK$^{\text{TM}}$ Organic Quantum Dots). The quantum dots scatter and absorb the incident UV light, and re-emit in the red, with a peak at $\lambda_{peak} = 665$ nm wavelength (see Fig. 5.4(b)). To place the quantum dots inside the capillary, the capillary is put in a teflon-lined fiber chuck (Newport FPH-J). A rubber stop is attached to the back end of the fiber chuck, and the quantum dots are sucked in the capillary using this assembly (see Fig. 5.4(a)). Finally, both ends of the capillary are sealed with super glue, as shown in Fig. 5.4(c). Hereafter, we will refer to the capillary-fiber chuck assembly as the probe.
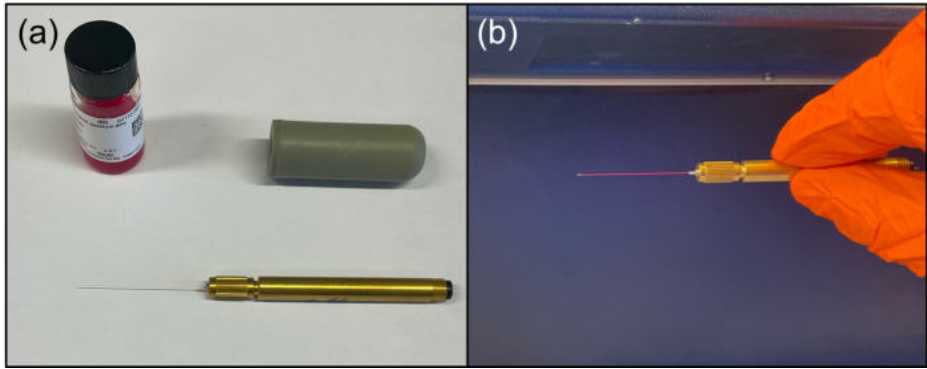
Figure 5.4: Photograph of the preparation phases of the probe. (a) The quantum dots, the capillary held by the fiber chuck, and the rubber stop used for sucking quantum dots inside the capillary. (b) Red emission is observed when the capillary is illuminated with UV light.

5.2.4 Experimental Setup

Figure 5.5 presents a schematic of the setup used in our experiments to probe the position-dependent energy fluence rate inside anisotropically scattering and absorbing samples. A blue laser (Thorlabs NPL41B) is used as the primary light source (see subsection 5.2.2). The laser beam is spatially filtered because of the many modes created inside the laser, which are not collimated as well as the main mode, still perturb the beam profile when the beam reaches the sample. The beam profiles at the sample position, before and after rough spatial filtering are shown in Fig. 5.6, where a substantial improvement is observed when the laser beam is spatially filtered. The sample holders SH1 and SH2, attached to the integrating sphere are 3D-printed in the Design Lab, whereas the holder SH3 where the probe is immersed in (see Fig.5.5), is 3D-printed in the Rapid Prototyping Lab of the University of Twente. The probe is connected to a custom-built holder with 3D-printed and manually made parts, as shown in Fig. 5.7. To detect the intensity emitted from the probe, a connector part is created in the workshop to connect the probe with a fiber-optic cable that is attached to a spectrometer (Avantes Starline, AvaSpec-2048L) on the other end. The holder is attached to an assembly of motorized translation stages (Thorlabs MTS50/M-Z8) that moves the probe to precise positions in 3 dimensions. In-house Python scripts are used to control the movement of the probe and detection with the spectrometer. The x-direction movement is utilized to dip the probe in and take it out of the sample, whereas the y and z-direction movements are used to scan the sample and measure the intensity at specific positions. Total transmission and total reflection measurements are done with an integrating sphere (Opsira uku240), with a port diameter $d_{port} = 20$ mm for both transmission and reflection ports (see also chapter 2).
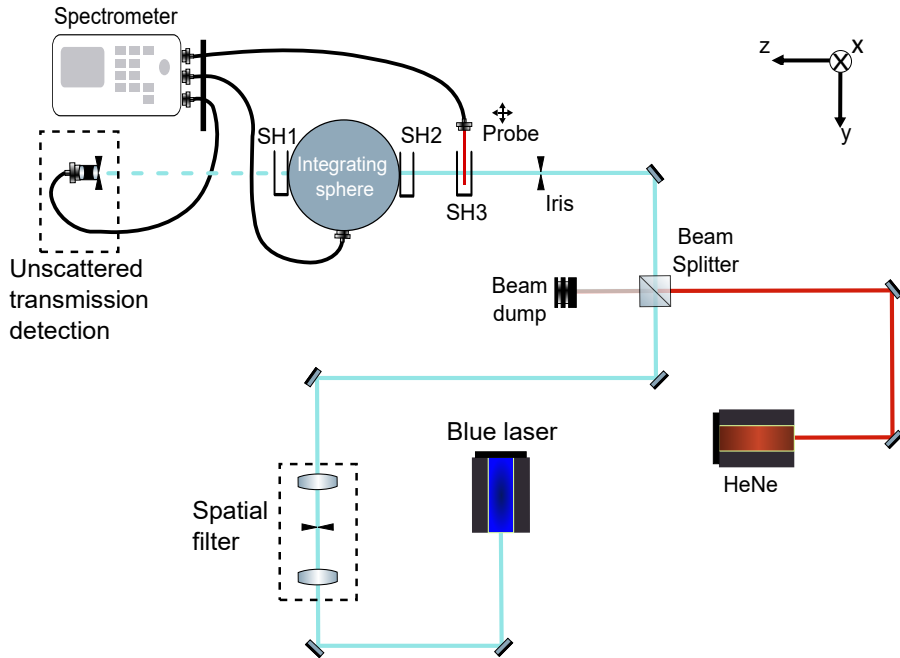
Figure 5.5: Schematic representation of the experimental setup. The blue laser is the primary light source and is combined with the HeNe laser at the beam splitter, for alignment purposes. The blue beam is spatially filtered. The probe is attached to an assembly of motorized translation stages, for precise positioning in 3 dimensions. The spectrometer is connected to the probe, integrating sphere, and unscattered transmission detection via fiber-optic cables. Holders SH1 and SH2 are used for total reflection and total transmission measurements, respectively. Holder SH3 is used for measurements with the probe and unscattered transmission (T_u) measurements Several components, including ND filters and beam dumps, have been omitted for clarity.
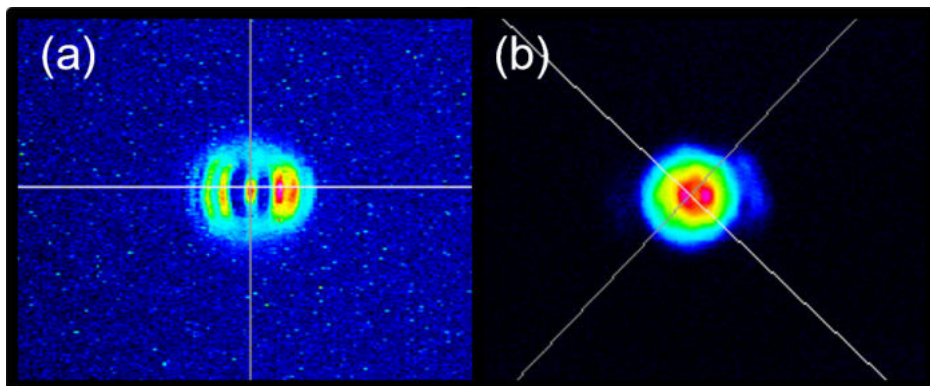
Figure 5.6: Measured beam profiles of the blue laser at the sample position (a) without spatial filtering, and (b) with spatial filtering.
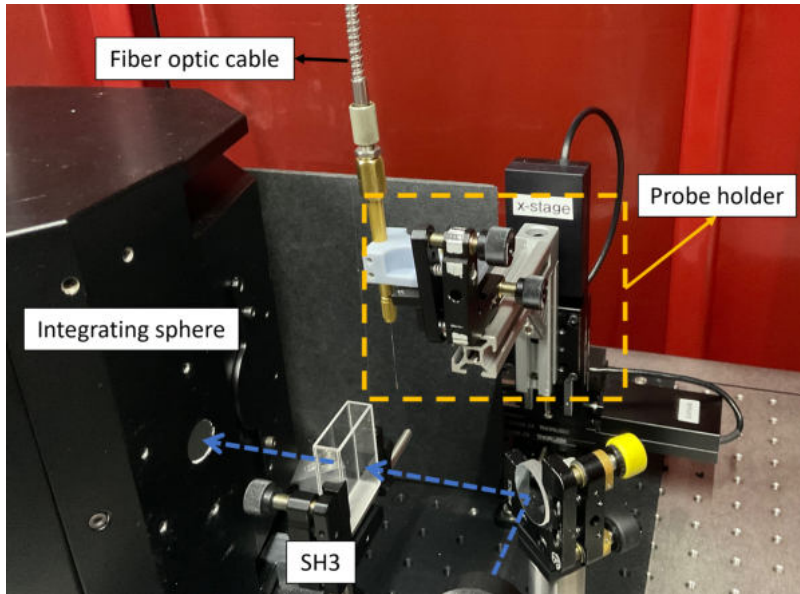
Figure 5.7: Photograph of the assembled probe holder. The fiber attached to the probe, the integrating sphere transmission port and the sample holder SH3 with an empty cuvette attached to it, is also visible in the photo.

Before measurements, each sample suspension is transferred to a wide quartz cuvette (outer dimensions $12.5 \times 32.5 \times 45 \, \text{mm}$) with an inner thickness of $L = 10$ mm along the z-direction. These cuvettes are then placed in sample holders for measurements. Holders SH1 and SH2 are used for total reflection and total transmission measurements, respectively. Holder SH3 is used for measurements with the probe and unscattered transmission (T_u) measurements, as the distance between the fiber coupler of T_u detection and SH3 is sufficiently long for this purpose [127].

5.3 Results and discussion

In this section, the results of unscattered transmission, total transmission, total reflection, and probe measurements are discussed. In addition, the method to extract the albedo a and the anisotropy g of the samples is discussed.

5.3.1 Unscattered Transmission, Total Transmission and Total Reflection

The unscattered transmission T_u represents the portion of the incident light that is transmitted through the sample without deviating from its initial direction of travel. In other words, it represents the light that survives extinction while maintaining its original direction. The Beer-Lambert-Bouguer's law is used to

express T_{u} as

$$T_{\mathrm{u}}(\lambda, \rho) = \frac{I_{\mathrm{u}}(\lambda, \rho)}{I_0(\lambda)} = e^{-\rho\sigma_{\mathrm{ext}}(\lambda,\rho)L}. \tag{5.1}$$

Here, I_{u} is the intensity transmitted without changing its direction, I_0 is the incident intensity, ρ is the number density, σ_{ext} is the extinction cross-section, and L is the sample thickness. Furthermore, the optical thickness b is defined

$$b(\lambda, \rho) \equiv \rho\sigma_{\mathrm{ext}}(\lambda)L = \mu_{\mathrm{ext}}(\lambda)L, \tag{5.2}$$

where μ_{ext} is the extinction coefficient.
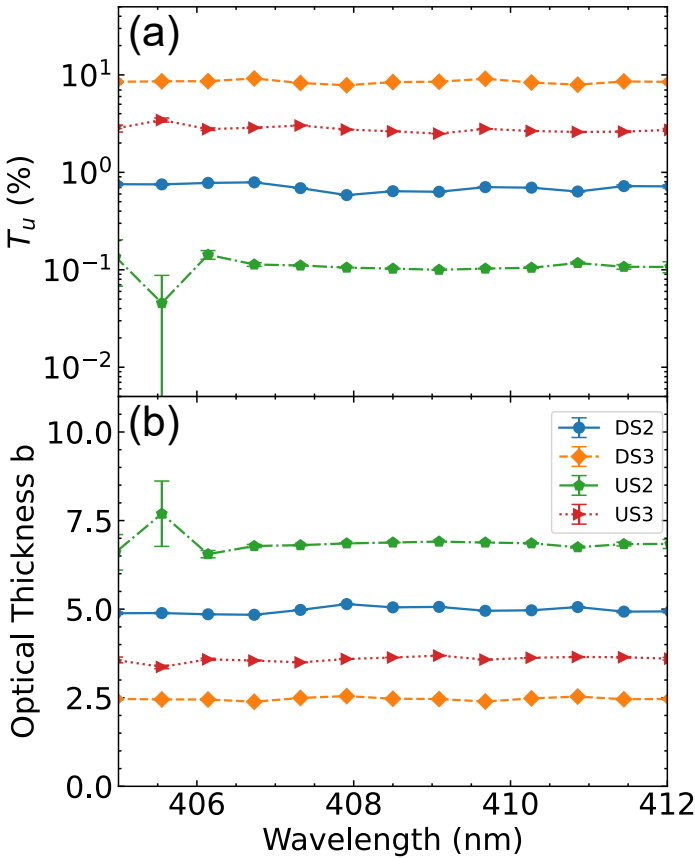
Figure 5.8: (a) Unscattered transmission T_{u}, and (b) extracted optical thickness b of samples DS2, DS3, US2 and US3.

Figure 5.8(a) presents the measured unscattered transmission T_{u}, and Fig. 5.8(b) displays the extracted optical thickness of samples DS2, DS3, US2, and US3 throughout the bandwidth of the blue laser. The densest samples DS1 and US1 have a vanishing transmission below our detection limit and are not shown.

Therefore, the optical thickness of DS1 and US1 are calculated from the measurements of other samples, by scaling the density of scatterers. The measurement results show a clear effect of the density of scatterers and the composition of the scatterers on the light transmission. Naively, one would expect dyed samples to be optically thicker than undyed samples with similar scatterer concentrations due to increased absorption, however, our measurements show the opposite. We attribute this interesting result to the presence of an unknown red dye inside the scatterers that alters the refractive index of the polystyrene spheres in DS2 and DS3. The dye likely makes the spheres more anisotropic, causing them to scatter light more in the forward direction. Consequently, the unscattered part of the transmitted light increases, which explains our observations in Fig. 5.8.
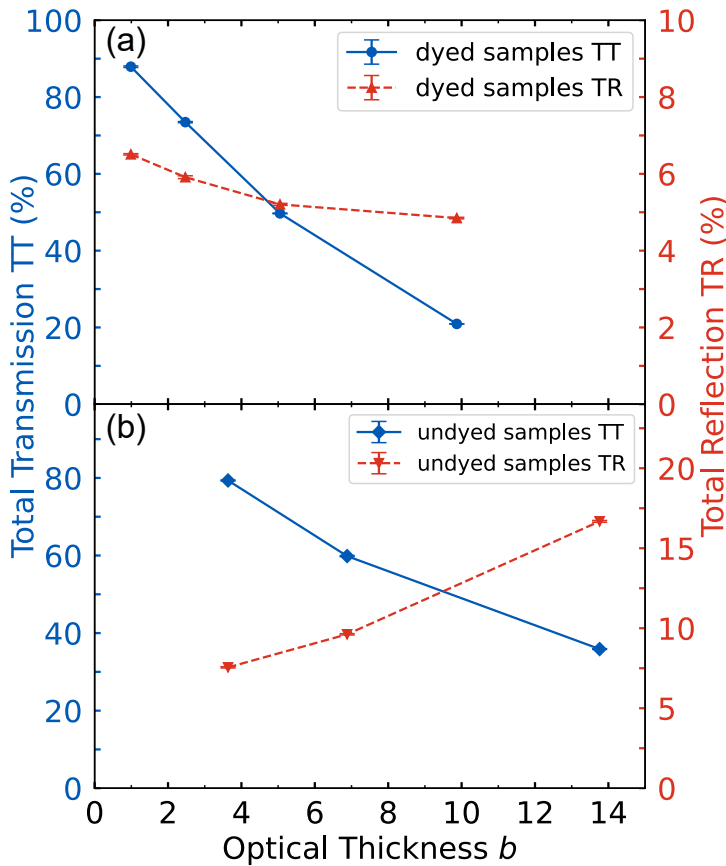
Figure 5.9: Total transmission TT(b) and total reflection TR(b) of (a)dyed microsphere suspensions, (b) undyed microsphere suspensions, as a function of optical thickness. The lines connect the data points.

Total transmission (TT) and total reflection (TR) measurements of dyed and undyed microsphere suspensions are displayed in Fig. 5.9 as a function of their

optical thicknesses at a wavelength of $\lambda = 408.5$ nm. As the optical thickness b increases, both TT and TR decrease for the dyed microspheres. The decrease in TT is in line with an increasing absorption, and the decrease in TR agrees with the increasing density of forward scattering scatterers and absorption as the suspension gets optically thicker. In contrast, for undyed sphere suspensions, the TR increases with increasing optical thickness due to the scatterers having negligible absorption. These measurements are necessary to determine the scattering parameters of the samples using models such as the diffusion approximation, P_N approximations, and Monte Carlo simulations of light transport.

5.3.2 Determining (a, g) parameters of the samples

Mie calculations provide the albedo and anisotropy (a, g) of scatterers in a sample if the complex refractive index and size of the scatterers are known. Unfortunately, the scatterers in the dyed microsphere suspensions are filled with a red dye that is unknown to us, as the manufacturer was not able to share the information. Therefore, the albedo and anisotropy (a, g) of dyed microsphere suspensions are determined by comparing TT and TR measurements to Monte Carlo simulations of light transport, using a *brute-force* approach. This process is similar to what is described in subsection 3.3.2. First, the optical thicknesses b of the samples are extracted, and then Monte Carlo simulations of light transport are performed for a grid of (a, g) pairs covering all possible albedos and anisotropies. We then use the relative cost function $S(a, g)$ defined as

$$S(a,g) \equiv \sqrt{\frac{(TT_{\mathrm{MC}}(a,g) - TT_{\mathrm{DS\#}}(a_0,g_0))^2}{TT_{\mathrm{DS\#}}^2(a_0,g_0)} + \frac{(TR_{\mathrm{MC}}(a,g) - TR_{\mathrm{DS\#}}(a_0,g_0))^2}{TR_{\mathrm{DS\#}}^2(a_0,g_0)}}, \qquad (5.3)$$

where $TT_{\mathrm{MC}}(a, g)$ and $TR_{\mathrm{MC}}(a, g)$ are the total transmission and reflection from Monte Carlo simulations, $TT_{\mathrm{DS\#}}(a_0, g_0)$ and $TR_{\mathrm{DS\#}}(a_0, g_0)$ are measured, (a, g) is the running coordinate in the albedo-anisotropy grid, and (a_0, g_0) is the albedo-anisotropy pair of the sample that we are trying to extract. For the measured $TT_{\mathrm{DS\#}}(a_0, g_0)$ and $TR_{\mathrm{DS\#}}(a_0, g_0)$ quantities, # represents the number of the sample name, given in Table 5.1.

Fig. 5.10 shows the contour plot of calculated $S(a, g)$ in percentage, for the densest sample DS1. The x and y axes represent all possible albedo a and anisotropy g values, respectively. $S(a, g)$ decrease as the (a, g) coordinates indicate strong forward scattering and absorption. The minimum cost or the best fit is found, as expected, in the strong forward scattering and moderately absorbing region of the (a, g) grid. However, it is noteworthy that the best fit to our measurements is at $g_0 = 1$, which is an extreme point and is realistically unattainable in real samples with scatterers. This implies that errors in our measurements have a significant effect on the determination of the (a, g) parameters of the samples. While the random errors in the measurements are negligible (see Fig. 5.9), the systematic errors are significant and merit further discussion below. We attribute the systematic errors to the integrating sphere ports, which are not large enough to capture the total reflected and transmitted light. Moreover, as

we perform single-beam measurements, there is an inherent *substitution error* of about 2% in our system (see Chapter 2).
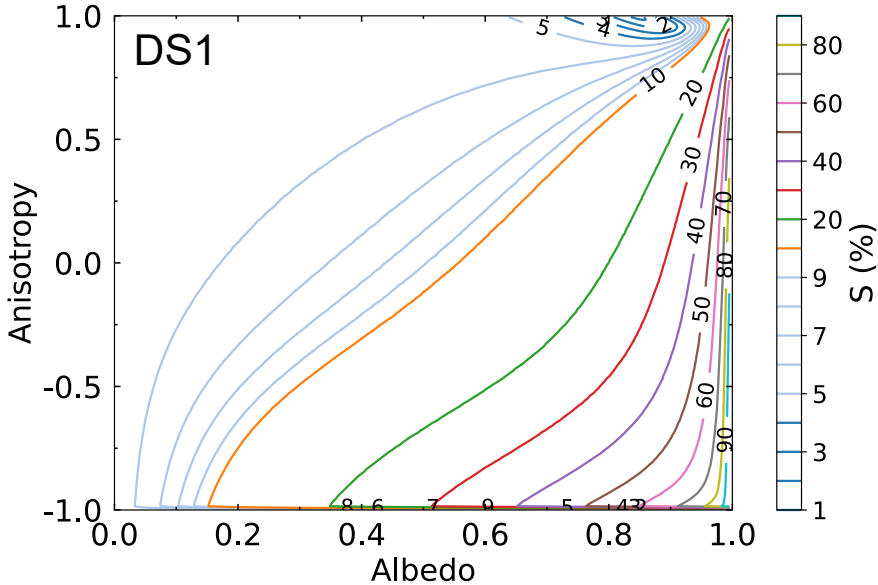

Figure 5.10: The calculated cost $S(a, g)$ for sample DS1 as a function of albedo (a) and anisotropy (g). The minimum of $S(a, g)$, that is in a forward scattering and absorbing range (top right of this figure), indicates the best fit between simulated and experimental total transmission and reflection. The contour plot shows the variation of $S(a, g)$ for different values of (a, g).

Systematic errors are more significant for samples with a lower density of scatterers, as the suspensions are held in quartz cuvettes, and light reflects from the cuvette walls multiple times before leaving the sample. This could cause the light to exit the sample at a wider angle than the integrating sphere can collect, especially for the total reflection measurements, as light is incident on the sample with a 6° angle (see Chapter 2). If the absorption is high inside the sample, this is a minor issue as the internally reflected light diminishes quickly and the spread is not wide. It is important to note that these internal reflections are included in the Monte Carlo simulations to obtain results as close as possible to the actual measurements. Since errors are larger for lower densities and as we know that the reference sample has $a = 1$ and $g = 1$, we estimate the maximum potential systematic errors of TT and TR for our measurements by comparing the measurements to the Monte Carlo simulations for the reference sample. This comparison gives us the maximum systematic error for the total transmission $\Delta TT = 6\%$ and for the total reflection $\Delta TR = 4\%$. We utilize these errors to extract a range of possible (a, g) parameters for each sample, and we take the average value of that range as the extracted pair. Additionally, we use the extracted range to model a dynamic range with the P_N approximations,

which are discussed in subsection 5.3.3. The extracted (a, g) parameters of the dyed microsphere suspension samples are given in Table 5.2, which shows that the dyed samples are highly forward scattering, and have moderate absorption.

Sample name	Extracted a	Extracted g
DS1	0.90 ± 0.02	0.95 ± 0.02
DS2	0.91 ± 0.01	0.96 ± 0.02
DS3	0.94 ± 0.02	0.97 ± 0.01

Table 5.2: Extracted albedo a and anisotropy g values of dyed microsphere suspension samples DS1, DS2 and DS3. The values reported here are averaged over the extracted range of (a, g) pairs, and errors are the standard deviation of the mean.

The comparison of simulated and measured transmission and reflection signals is not necessary for the undyed microsphere suspensions, as their optical properties can be obtained directly from Mie calculations. The complex refractive index of polystyrene spheres at 408.5 nm is taken from reference [128] to be $n_{\text{poly}} = 1.61 + 0.0004i$, which yields non-absorbing $a = 0.997$ and strong forward scattering $g = 0.919$ for the undyed microspheres suspended in DI water. Additionally, Mie calculations provide the extinction cross-section σ_{ext}, which we utilized together with the uncertainty of the scatterer radius $\Delta r_{\text{scat}} = \pm 0.03$ μm to determine the $\sim 13\%$ uncertainty in the reported densities listed in Table 5.1. These extracted (a, g) parameters for both dyed and undyed samples lie within the range where P_1 and P_3 approximations fail, whereas $P_3 + \delta E(4)$ should give accurate results.

5.3.3 Position-dependent energy fluence rate of dyed microsphere suspensions

To determine the position-dependent energy fluence rate $\Phi(z)$, the light intensity at specific points inside samples is measured using the experimental setup described in subsection 5.2.4. The coordinate system adopted in this section is depicted in Fig. 5.5. The objective is to infer $\Phi(z)$ from measurements of the emission of quantum dots inside the probe, which are excited by the blue light inside the sample, along z from the left boundary at $z = 0$ where the incident light enters, to the right boundary at $z = 10$ mm. Finally, the experimental data are compared to the theoretical models outlined in Chapter 3. Due to experimental constraints, the probe scans start at $z = 0.05$ mm and end at $z = 9.75$ mm.

Measurements with probe along the z-direction inside the sample DS1 are shown in Fig. 5.11, including the results from four primary scan directions: forward, forward-side, random, and random-side. The forward direction indicates that the sample is scanned from the left boundary ($z = 0$) to the right boundary ($z = 10$), while forward-side refers to scanning the sample in the same direction as forward in z, as well as scanning it in the y-direction at specific z-positions. Random direction refers to scans of the sample along the z-direction with the

probe randomly positioned during the scan. Finally, random-side indicates that the sample is scanned in the same way as in random direction, but in addition, it is scanned in the y-direction at specific z-positions, and the y-scans are also done with a random positioning of the probe. Fig. 5.11 shows that the scan direction has minimal influence on the outcomes. The minor differences are attributed to slight instabilities of the probe holder, which are discussed further in subsection 5.3.5.
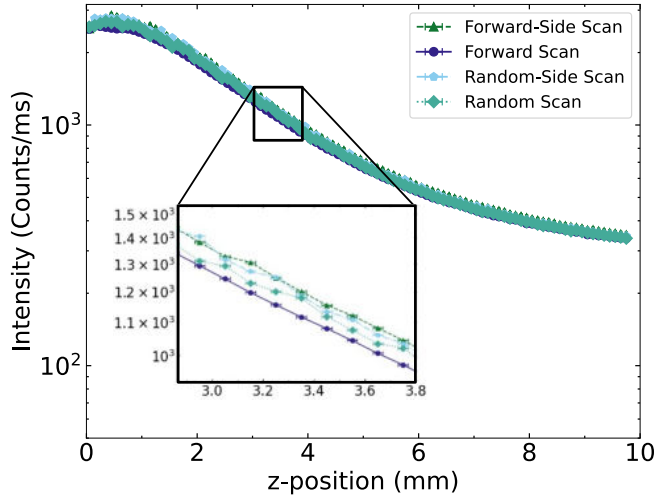
Figure 5.11: Representative scans of the position-dependent intensity in the z-direction in sample DS1, for four different scan directions. The inset highlights the small differences between scans.

Figure 5.12 presents the position-dependent intensity in the z-direction for samples DS1, DS2, and DS3. The datapoints in Fig. 5.12 represent an average of four different scan directions, as elaborated in Fig. 5.11. Notably, the optically thicker samples exhibit a higher intensity than the thinner samples, up to a depth of approximately 2 mm inside the sample. This behavior is attributed to the increased number of scatterers in the thicker samples, which scatter the light into the probe more than the less dense samples at the first few millimeters. After $z = 2$ mm depth, the trend reverses and the densest sample has the lowest detected intensity. This trend is expected, as the extinction is higher for thicker samples. However, it should be noted that while the probe scans the z-direction entirely in this measurement, it is insufficient to fully characterize the $\Phi(z)$ as modelled in Chapter 3, since a large portion of the xy-plane is not measured. The models simplify the problem to one dimension by utilizing the symmetries within the slab and averaging over the xy-plane at each z-position [98]. The diameter of our probe is 170 μm, while the beam size is approximately 1 mm, and the z-scans are done when the probe is at the center of the beam in y-direction. Consequently, although the probe's length in the x-direction is roughly 40 mm within the sample, the scan presented in Fig. 5.12 predominantly collects the

unscattered intensity.
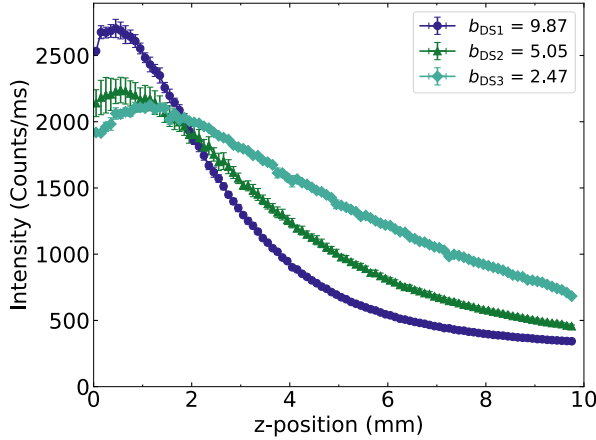
Figure 5.12: Position-dependent intensity in the z-direction detected inside dyed microsphere suspensions DS1, DS2 and DS3. Optical thicknesses of the samples are given in the legend. Data points represent the averages of four scans in different directions (see Fig. 5.11).
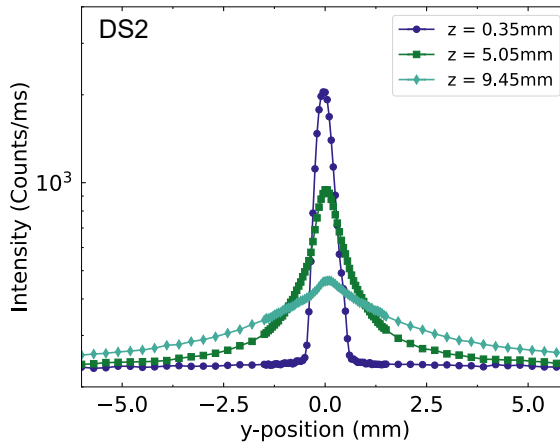
Figure 5.13: Representative scans of y-direction at specific z-positions inside sample DS2.

In order to obtain a more comprehensive understanding of $\Phi(z)$, it is necessary to scan samples in the y-direction at various positions in z. Figure 5.13 presents three scans at specific z-positions. The results show that the energy distribution broadens in the y-direction as the light travels deeper in z, in agreement with expectations from multiple scattering [3, 6, 11, 129]. All samples are probed in the y-direction at numerous z-positions, and the resulting curves obtained from

these y-scans at each z-position are integrated to derive a value that represents the total $\Phi(z)$ integrated over an xy-plane. Fig. 5.14 shows the integrated y-scans of sample DS2, where the z-positions are scaled by the thickness of the sample, and the measured $\Phi(z)$ is normalized by the incident intensity. Notably, Fig. 5.14 illustrates the inclusion of diffuse light to the detection, in contrast to the measurements obtained solely from z-scans, as shown in Fig. 5.12. To compare with these measurements, $\Phi(z)$ is modelled using the P_1, P_3, and $P_3 + \delta E(4)$ approximations to the radiative transfer equation, and Monte Carlo simulations of light transport [98].
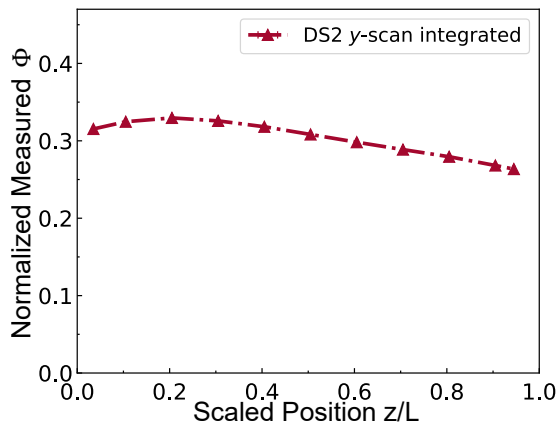
Figure 5.14: Representative integrated y-scans at specific z-positions inside sample DS2.

Fig. 5.15 presents the comparison between the models and our measurements. The P_1 and P_3 approximations are not shown as they demonstrate poor accuracy in Fig. 5.16. The green areas represent the modelled values for the extracted (a, g) range using $P_3 + \delta E(4)$ approximation. The horizontal axis represents the z-positions scaled by the thickness of the sample, while the vertical axis on the left displays the $\Phi(z)$ measurements of samples normalized to the measurements of the incident intensity, which is presented in Fig. 5.18(b). The right vertical axis corresponds to the modelled relative $\Phi(z)$. Both vertical axes are scaled to compare the trends of measured and modelled Φ, and a good agreement is observed between them. We define a straightforward relation, neglecting the small random errors in measurements,

$$\Phi_{\mathrm{real}}(z) \equiv K\Phi_{\mathrm{measured}}(z), \tag{5.4}$$

where K is a constant that represents the portion of Φ that is measured. K mainly depends on the experimental limitations that are discussed below in subsection 5.3.5. The small differences in measured and modelled Φ trends, excluding the scaling discussed above, are attributed to the limitations of the Henyey-Greenstein phase function [109].
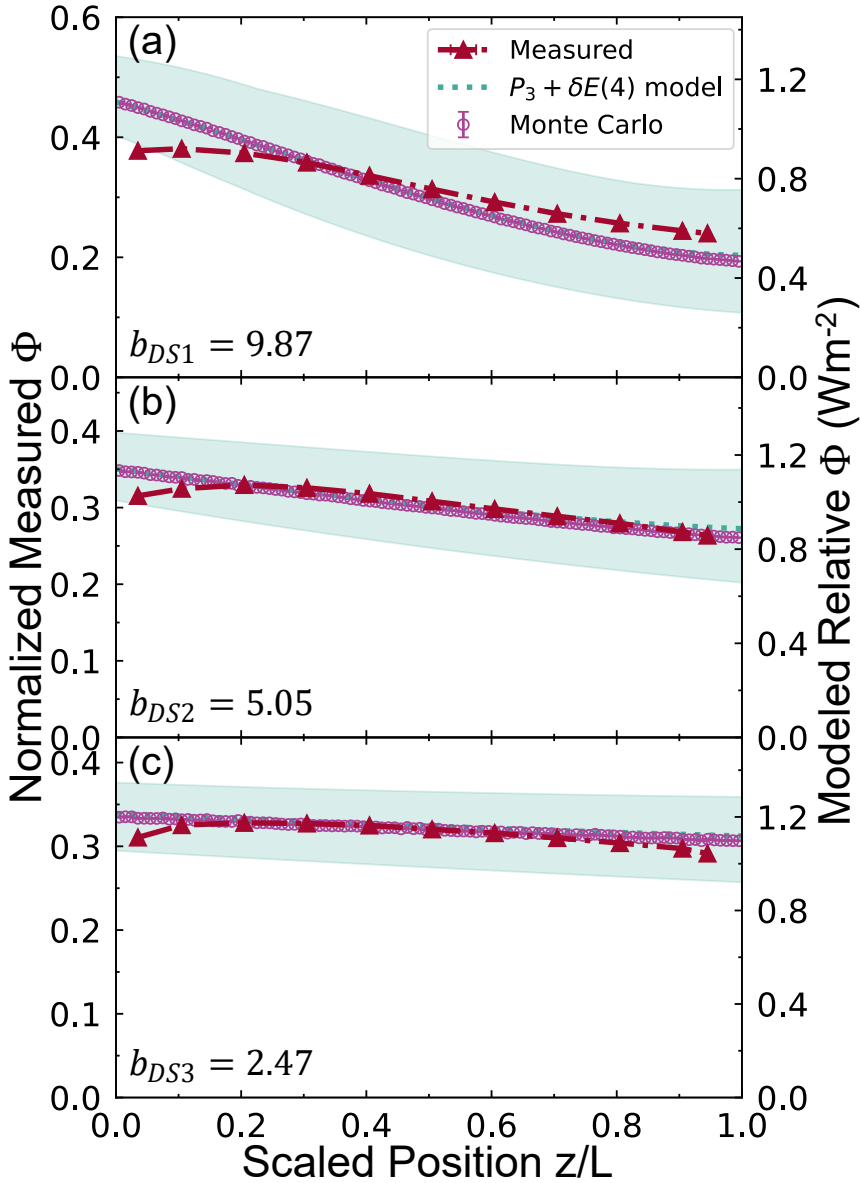
Figure 5.15: Comparison of measurement and models for samples (a) DS1, (b) DS2, and (c) DS3. The dotted lines represent the calculated $\Phi(z)$ from the $P_3 + \delta E(4)$ approximation. The dynamic range of the $P_3 + \delta E(4)$ approximation is shown as the green area. The circles represent the results of Monte Carlo simulations, and the triangles connected with red dash-dotted lines represent the measured results of samples. The measured results are calculated by integrating the y-scans at each z-position, shown as triangles.
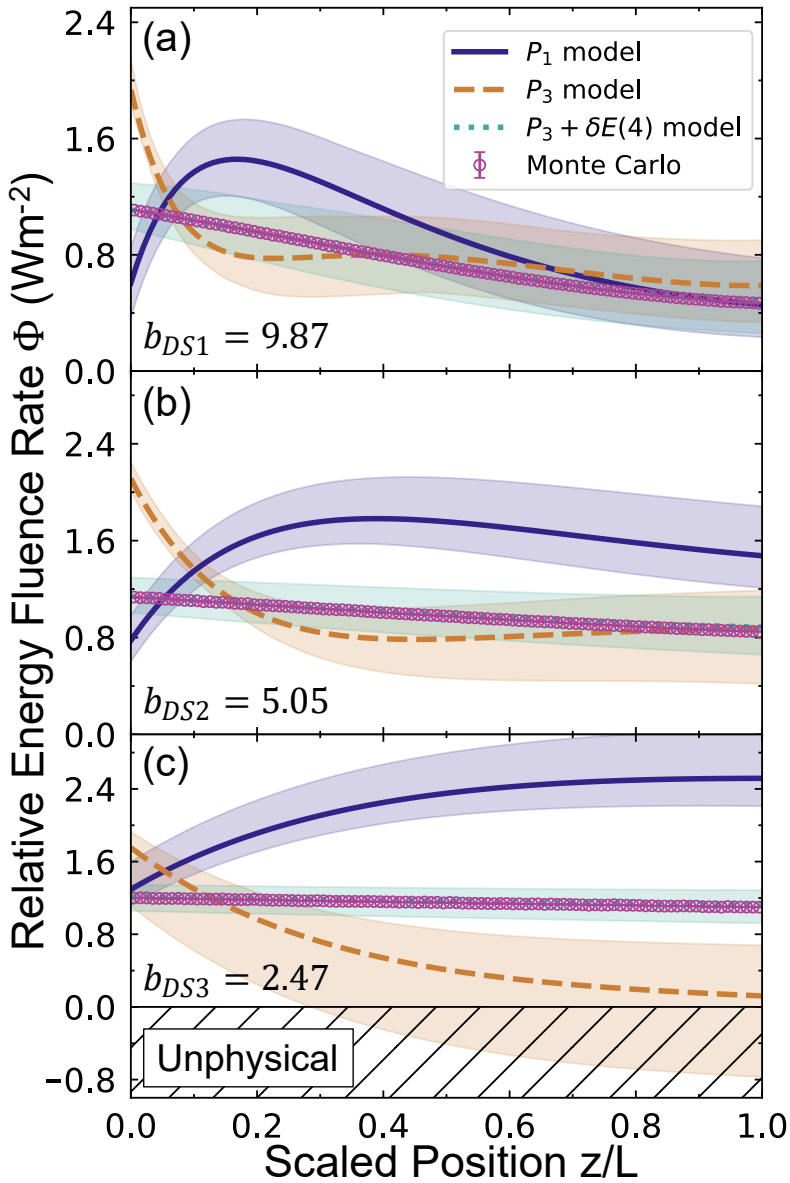
Figure 5.16: Modelled position-dependent energy fluence rate $\Phi(z)$ for samples (a) DS1, (b) DS2, and (c) DS3. Lines represent the results of the P_N approximations, and circles represent the results of Monte Carlo simulations. In (c), the unphysical area where Φ is negative is hatched in black

The results of the P_1, P_3, and $P_3 + \delta E(4)$ approximations and Monte Carlo simulations are illustrated in Fig. 5.16, where the z-positions are scaled by the thickness of the sample, and the modelled $\Phi(z)$ is relative, as the incident flux

density (irradiance) in the models is set to be $F_0 = 1$. The dynamic ranges of the P_N approximations represent the modelled values for the extracted (a, g) range. Initially, it may appear confusing that a relative result is greater than 1, as seen in the case of sample DS1. Although both the irradiance F_0 and energy fluence rate Φ have the same units Wm^{-2}, the former denotes the optical power through the surface of a *flat* unit area in the direction normal to the surface, while the latter refers to the total optical power through a *spherical* unit surface area in all directions [23]. Therefore, depending on the scattering properties of the medium being measured, it is possible for Φ to be larger than the incident irradiance [37, 130, 131].

Fig. 5.16 shows that the $P_3 + \delta \mathrm{E}(4)$ approximation has the closest agreement with the Monte Carlo simulations, which is consistent with previously reported findings [37, 98] (see Chapter 3). The P_1 and P_3 approximations perform poorly for these anisotropically scattering and absorbing samples, and the P_3 approximation even predicts an unphysical negative energy fluence rate in the dynamic range of the optically thin sample DS3. The unphysical results of the P_3 approximation for sample DS3 also agree with our previous findings [98] presented in Fig. 3.3, which shows a broader unphysical range of P_3 for optically thin samples in the strong forward scattering range, compared to the thicker samples.

5.3.4 Position-dependent energy fluence rate of undyed microsphere suspensions

In this subsection, we present measured $\Phi(z)$ of undyed sphere suspensions and compare them to models. Fig. 5.17 presents the comparison of all models to measurements. The P_N approximation results do not have dynamic ranges in Fig. 5.17 as the (a, g) pair of samples US1, US2, and US3 are extracted from exact Mie calculations, as explained in subsection 5.3.2. Similar to Fig. 5.15, the horizontal axis denotes the z-positions scaled by the thickness of the sample, and the left vertical axis gives the $\Phi(z)$ measurements of samples normalized to the measurements of the incident intensity given in Fig. 5.18(b). The right vertical axis is the modelled relative $\Phi(z)$, and both vertical axes are scaled to compare the trends of measured and modelled Φ. A good agreement between the trends of $P_3 + \delta E(4)$, Monte Carlo, and measurements are observed. Differences due to experimental limitations are discussed in subsection 5.3.5.

5.3.5 Experimental Limitations

Systematic errors are inevitable in any experimental measurement, including the measurements of $\Phi(z)$. It is important to identify and comprehend the underlying causes of the systematic errors, before claiming that the measurements reflect reality. This subsection discusses the limitations of our experiment that affects the scaling value, K, for eqn. 5.4.

The discussion starts with the shift in detected peaks for y-scans at different z-positions, which is not immediately obvious for scans presented in Fig. 5.13. To clarify this effect, y-scans by the probe at specific z are presented in Fig. 5.18(a),
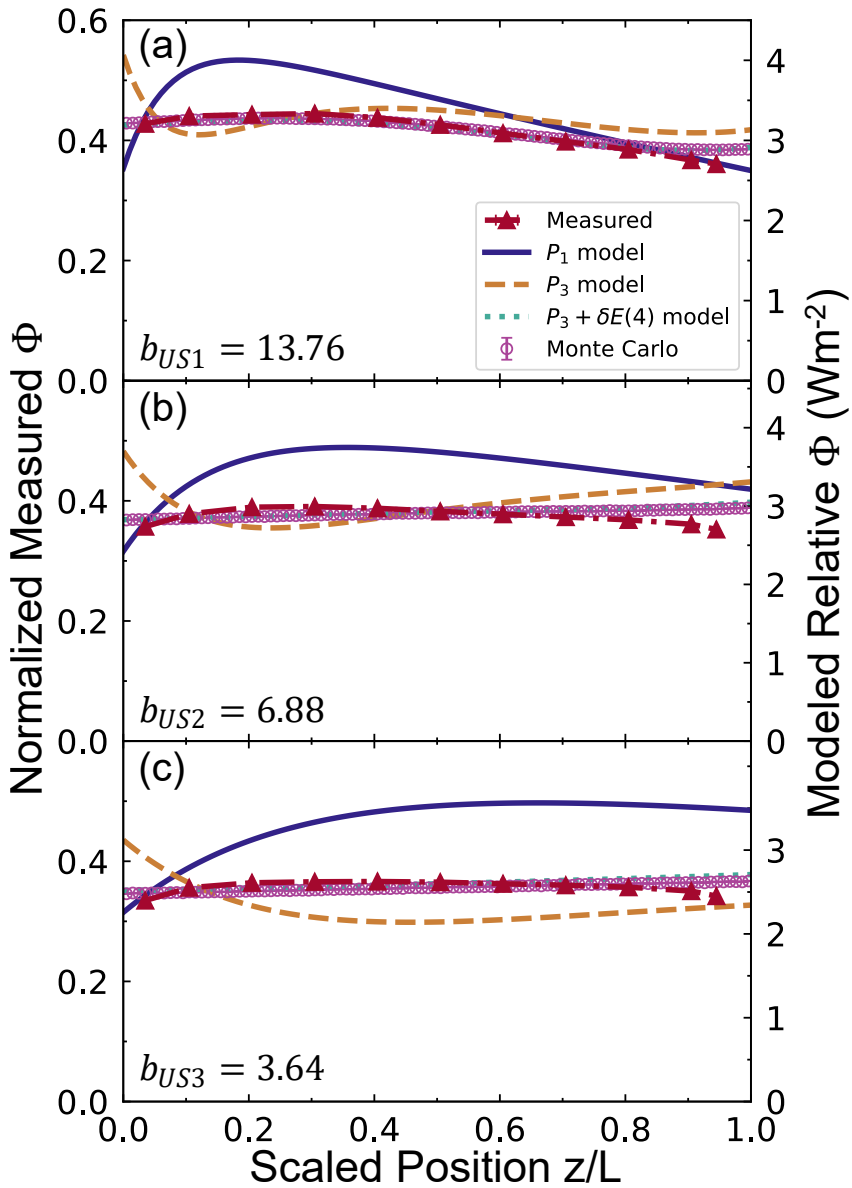
Figure 5.17: Comparison of measurement and models for samples (a) US1, (b) US2, and (c) US3. The lines represent the results of the P_N approximations and the circles represent the results of Monte Carlo simulations The red triangles connected with dash-dotted lines represent the measured results of samples. The measured results are calculated by integrating the y-scans at each z-position, shown as triangles.

which demonstrate a clear shift of the detected intensity in the y-direction. This shift is caused by the probe moving at a small angle with respect to the z-axis.

The angle is estimated as approximately $\theta_z = 0.63°$, considering the peaks movement of 0.1 mm in the y-direction for a 9.1 mm travel in the z-direction. Furthermore, Fig. 5.18(b) presents the incident intensity detected by the probe in air, which is used to normalize the measurements of samples in order to compensate for the effect of the y-shift.
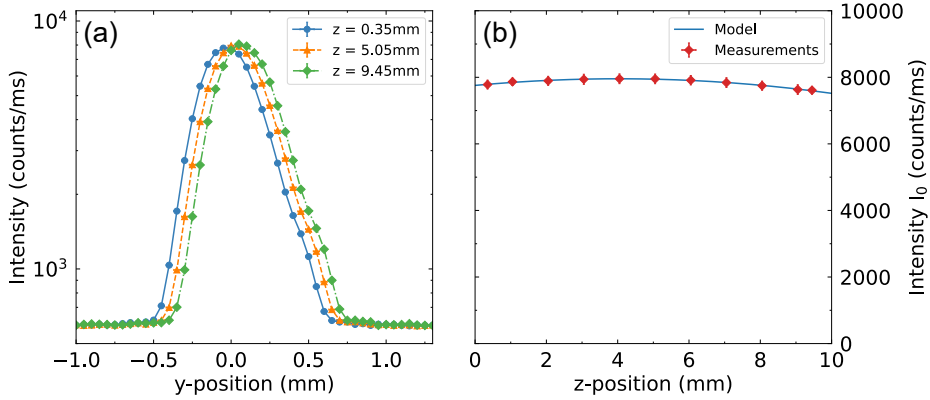
Figure 5.18: (a) Probe scans in the y-direction in absence of a sample. This represents the incident beam profiles at the indicated z-positions inside the sample. (b) Integrated y-scans at specific z-positions, in the absence of a sample. The blue line represents the polynomial fit to the measurements, to determine the incident beam intensity at all z-positions.

Other experimental limitations associated with the measurements with the probe are listed as follows:

1. The capillary filled with quantum dots, is not exactly parallel to the x-axis given in Fig. 5.5. Although the kinematic mount attached to the probe holder, as shown in Fig. 5.7, is utilized to adjust the capillary angle, perfect alignment is not always achieved. As a result, the probe positioning inside the sample is restricted to a range between $z = 0.35$ mm and $z = 9.75$ mm, for the z-direction. In the event that the probe approaches the boundaries beyond these limits, the capillary may come into contact with the quartz walls of the cuvette, potentially causing its displacement or, worse, breaking of the capillary.

2. The stabilities of the probe holder, sample holder, and fiber-optic cable that connects the probe and detector are not ideal. Small variances in different scan directions presented in Fig. 5.11 are likely caused by this. However, even slight changes in the adjustment of these elements can lead to drastic changes in the detected intensity. Therefore it is crucial to normalize the measurements to the incident intensity measured under identical conditions as the sample measurements. The measurements presented in this chapter are conducted with utmost care to address this issue.

3. The finite dimensions of the cuvette used in our experiments differ from ideal slab geometry, as a slab has an infinite xy-plane. However, the beam diameter of our source ($d_{\text{beam}} \approx 1$ mm) is significantly smaller than the inner xy-dimensions of the cuvette (42.5×30 mm), rendering this effect negligible.

4. Although the measurement of $\Phi(z)$ along the xy-plane is carried out through y-scans of the samples, the scans are limited to the range $y = -6$ mm to $y = 6$ mm with the beam centred at $y = 0$. This range is selected due to low signal strength beyond this range, and to shorten the complete measurement time of samples. The range restriction leaves 18 mm of unmeasured space in the y-axis. Additionally, during the sample scans, the capillary tip is situated at a distance of approximately $x \approx 11$ mm from the cuvette's bottom. Consequently, the probe scans a rectangular area of dimensions 34 x 12 mm within the cuvette. Hence, the portion of the scanned area to the full xy-plane within the sample is $A_{\text{scan}} = 32\%$. However, the measurement of $\Phi(z)$ cannot be directly scaled with A_{scan} because the experiments employ a collimated beam as the source and detect most of the light within the cuvette, as evident by the low signal strength beyond the scan range (see Fig. 5.13). However, it is worth noting that the signal outside the scanned range is higher for undyed samples, owing to the lower absorption by the scatterers compared to the dyed samples. Therefore, the scaling difference between the measured and modelled $\Phi(z)$ for undyed samples is greater than the one for dyed samples.

5. The quantum dots inside the capillary have a certain quantum yield to convert absorbed blue light to emitted red light. This quantum yield is provided by the manufacturer as $\eta \geq 64\%$. Furthermore, the manufacturer provides the molar extinction coefficient $\epsilon = 5.7 \times 10^6$ cm^{-1}M^{-1}, and the molar concentration $c = 1.0 \pm 0.1$ μM. Using the inner diameter of the capillary that holds the quantum dots $d_{\text{inner}} = 100$ μm and the Beer-Lambert-Bouguer's law, we calculate the extinction E_{qdots} to be

$$E_{\text{qdots}} = \epsilon c d_{\text{inner}} = 57, \tag{5.5}$$

and the optical thickness b_{qdots} to be

$$b_{\text{qdots}} = E_{\text{qdots}} * \ln(10) = 131.2. \tag{5.6}$$

6. The presence of the probe inside the sample has an impact on light transport within the medium. In order to investigate this effect, the unscattered transmission T_{u} of the probe is measured [1], while scanning in the y-direction at various z-positions inside sample Ref (see Table 5.1). The obtained results are illustrated in Fig. 5.19. Based on Fig. 5.19, the extinction coefficient of the probe is derived as $\mu_{\text{ext}} = 4.8$ mm^{-1} when the

---

[1]This measurement is conducted with a similar capillary as the one used in the measurements of $\Phi(z)$.

probe is situated at the center of the beam. The μ_{ext} represents the sum of absorption and scattering by the probe, hence, the absorbed portion of light by the probe and quantum dots inside, cannot be estimated by this measurement alone.
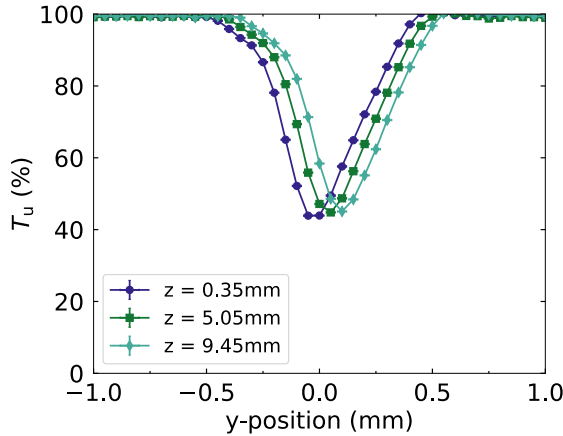
Figure 5.19: Unscattered transmission T_{u} of the probe scanning the y-direction at various z-positions inside sample Ref, see Table 5.1.

7. Part of the emitted light propagates through the capillary and emerges from its top, where it is coupled to the fiber-optic cable of the spectrometer via a connector manufactured in the workshop of the University of Twente. This connector, visible in Fig. 5.7, introduces a distance of approximately $d_{\text{cap}-\text{fiber}} \approx 5$ mm between the capillary and the fiber. Assuming that the light emanates from the capillary with a solid angle of 2π and taking into account the core diameter of the fiber-optic cable (600 μm), straightforward calculations yield a coupling efficiency of $\eta_{\text{coup}} = 2\%$ between the capillary and the fiber.

All the experimental limitations listed above contribute to the deviation of measurement results to the model predictions in scale, hence the parameter K in eqn. 5.4 is introduced to capture these effects.

5.4 Summary

In this chapter, we present a comprehensive analysis of the experimental measurements of the position-dependent energy fluence rate of samples. The analytical P_1 and P_3 approximations to the radiative transfer equation predict inaccurate results for these samples, which are various dilutions of dyed and undyed polystyrene microsphere suspensions. The albedo and anisotropy parameters for the dyed samples are extracted from experiments and Monte Carlo simulations, while Mie calculations are used to determine the parameters for the undyed samples. A thin capillary filled with quantum dots is used in the experiments as a

probe to measure the fluence rate inside the sample, and the results are compared to analytical models and Monte Carlo simulations. We provide a detailed account of the experimental limitations that prevent an absolute measurement, and an exact match with the models. Notably, the P_1 and P_3 approximations fail to match the observed trends in the position-dependent fluence rate, as anticipated. In contrast, the Monte Carlo simulations and the $P_3 + \delta E(4)$ approximation, which do not yield unphysical results for the samples under consideration, exhibit a relatively good agreement with the measured trends of the fluence rate.

6 Probing position-dependent energy density in quasi-2D disordered arrays of silicon micropillars

6.1 Introduction

So far in this thesis we have studied the light transport through three dimensional (3D) random media containing spherical scatterers, with a focus on predicting and measuring the position-dependent energy density, which is relevant to many applications as outlined in chapters 3 and 5. However, numerous other application domains involve samples that contain scatterers with *anisotropic shapes*, such as biological tissues [132–135], forests [136–140], atmospheric dust [141, 142], and nematic liquid crystals [143–146]. The scatterers in these samples are often assumed to be cylinders. To describe the light transport in anisotropic scattering media, mostly the anisotropic diffusion theory [144, 147–149] or Monte Carlo simulations of radiative transport [133, 150–152] are used in the literature.

In this chapter we perform a study of the transport of light in quasi-2D ensembles of micropillars, made from silicon (Si) that have a shape that is as cylindrical as possible. These samples are especially attractive for localization studies, since they have high refractive index contrast between the scatterers and the medium, hence strongly scattering [148, 153]. Furthermore, they are fabricated in a manner that allows good control of shape and orientation of the scatterers (see section 6.2). In 2D random medium with such properties, observation of Anderson localization is predicted to be possible, however, the size of the cylinders and the wavelength of the incident light should be optimized for that purpose [153].

For perspective, figure 6.1 provides an overview of exemplary scattering media from literature with anisotropically shaped scatterers, in terms of their orientation of the scatterers defined below, and the refractive index contrast Δn between scatterers and their surrounding medium defined as

$$\Delta n \equiv |n_{\text{scat}} - n_{\text{sur}}|, \tag{6.1}$$

where n_{scat} and n_{sur} are the refractive indices of the scatterers and the surrounding medium, respectively. The refractive indices provided are either taken directly from the corresponding reference (with respect to the wavelength of light used in the corresponding study), or estimated for wavelength $\lambda = 1064\ \mu$m. We define $\langle \cos \zeta \rangle$ to be the average cosine of the angle ζ between the long axes of the

anisotropically shaped scatterers, to represent the average orientation of scatterers. Therefore, $\langle \cos \zeta \rangle = 1$ means the scatterers are parallel, and $\langle \cos \zeta \rangle \approx 0$ means there is no apparent general orientation. From this comparison it is apparent that our samples are in the well-aligned limit, and push the index contrast beyond state of the art, with the additional feature compared to GaP that our scatterers have a well-defined geometry that makes them readily amenable for modelling.
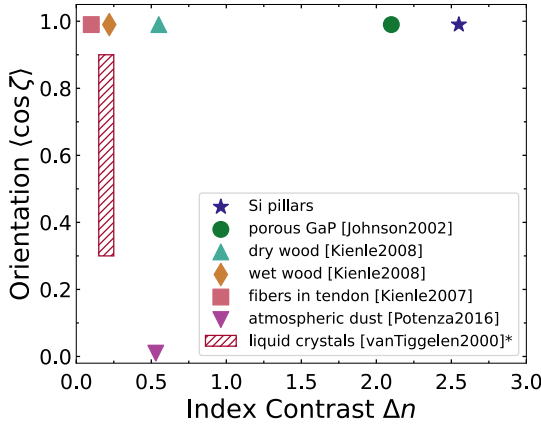
Figure 6.1: Exemplary scattering media with anisotropically shaped scatterers, as a function of orientation $\langle \cos \zeta \rangle$ and refractive index contrast Δn, which are defined in the text. Si pillars represent the samples used in this chapter. The data for Porous GaP [148], dry and wet wood [154], fibers in tendon [155] and atmospheric dust [141] are estimated from the respective references. *For liquid crystals, the anisotropic refractive index and an accepted range of order parameter S defined in reference [145] is used for x and y-axes, respectively.

Figure 6.2 shows an illustration of a sample with randomly positioned and parallel oriented cylindrical scatterers, that is illuminated by a light beam with intensity I_0 and incident direction z. When the direction of incident light aligns perpendicular to the long axes of the cylinders, the light is scattered only in the two-dimensional (2D) xz-plane, thus, the sample is translational-invariant. This ideal case assumes that the cylinders are long enough that the ends of cylinders do not scatter light into the third dimension. Furthermore, the cylinders are closely parallel to each other, so the light transport is confined in 2D. In reality, unavoidable fabrication defects cause roughness on the surface, imperfect parallelism between the cylinders, and scatterer shapes that are not perfect cylinders, all of which results in a quasi-2D sample with some light scattering in the y-direction, shown as scattered intensity I_{scat} in Fig. 6.2. Since the sample is multiple scattering, this transfer into the third dimension is significant. Nevertheless, we assume the transport in the 3rd dimension hardly affects the 2D scattering, since it is not very likely that a lot of light travelling in the y-direction will be scattered back in the xz-plane. In other words, we assume the transport

mean free path of our samples in y-direction to be much larger than the sample thickness in y-direction, $\ell_{\mathrm{tr,y}} \gg L_y$. While the out-of-plane scattering may be considered as loss in studies that aim to observe strong and weak localization of light in multiple scattering media [156–160], for us it is a feature that we can exploit to extract information from within the sample [161, 162]. We assume that the intensity detected in the 3$^{\mathrm{rd}}$ dimension is proportional to the energy density in the 2D xz-plane.
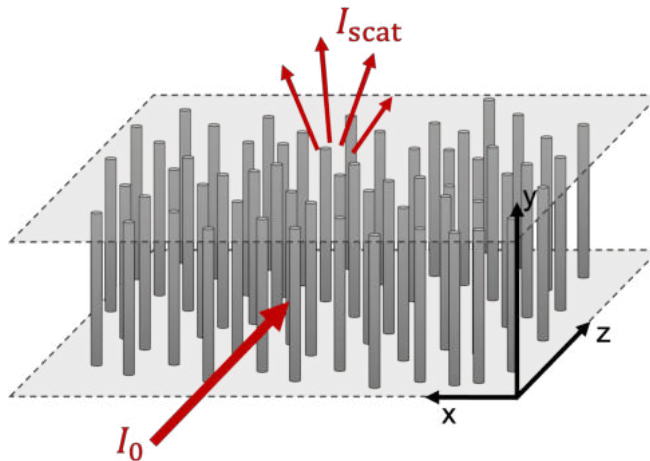
Figure 6.2: Illustration of a sample consisting of randomly positioned cylinders with equal dimensions and parallel long axes in the y-direction. Light with intensity I_0 and direction z is incident on the cylinders. For a non-ideal sample with defects, part of the light scatters into the y-direction, illustrated as scattered intensity I_{scat} at the top, where it is conveniently detected.

In this chapter, we report the experiments done to measure the position-dependent energy density inside slabs with randomly positioned Si pillars. We employ the fabrication feature of light scattering into the third dimension, and measure the scattered light from the top of the sample to observe the energy distribution inside the sample. We explain the fabrication of the samples, the experimental procedures, and present the first results[1] acquired from the setup.

6.2 Experimental details

The samples used in this chapter require different approaches than the microsphere suspensions, both in terms of fabrication and measurement. The fabrication of Si pillars is done by etching a silicon wafer using reactive ion etching [163],

---

[1]The measurements of samples are ongoing at the time of writing this thesis. Once the experiments are completed, the findings will be submitted to a peer-reviewed scientific journal.

and the energy density is probed by detecting the scattered light from the top of the sample.
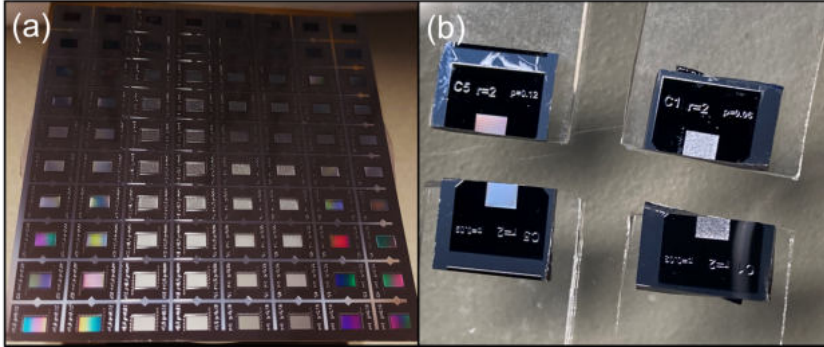
Figure 6.3: Photographs of random and ordered arrays with different scatterer densities (a) before cutting out of the wafer, and (b) individual samples attached to glass slides for experiments.

6.2.1 Sample fabrication

Patterns for randomly placed micropillars were generated by in-house Matlab script, and a mask that fits 80 samples in one wafer was designed with those patterns using CleWin software. Samples are distinguished by having different pillar radii of $r = 2\,\mu$m or $r = 3\,\mu$m, and having different packing fractions p, ranging from $0.03 < p < 0.12$, defined as

$$p \equiv \frac{(\text{num. of pillars}) \times V_{\text{scat}}}{V_{\text{sample}}}, \qquad (6.2)$$

where V_{scat} and V_{sample} are the volumes of one micropillar and the sample, respectively. The pattern also includes samples with periodically ordered structures, however those samples are not discussed in this thesis. All sample fabrication was performed in the MESA+ Nanolab. Silicon wafers (110, p-doped silicon, 4 inch, 500 nm thickness) were coated with a layer of positive photoresist (Olin OiR 908-35) that was spin-coated at 4000 rpm for 1 min and baked at 95 °C for 10 min to remove residual solvent. An EVG 6200NT mask aligner was used for the mask exposure, for which a hard contact and an exposure of 195 mJ/cm² were used. The sample was then post-exposure baked at 120 °C for 2 min before being developed in OPD 4262 positive resist developer. The sample was then rinsed with deionised water in a quick dump rinser until a resistivity of 10 Mohm was reached. Etching was performed using a SPTS Pegasus reactive ion etcher, using C_4F_8 as the protection gas, SF_6 as the etching gas and O_2 for plasma cleaning to remove leftover fluorocarbon. A TePla300 plasma cleaner using O_2 was used to remove any leftover photoresist using a preset programme. Finally, individual samples are cut from the wafer using a diamond scriber.
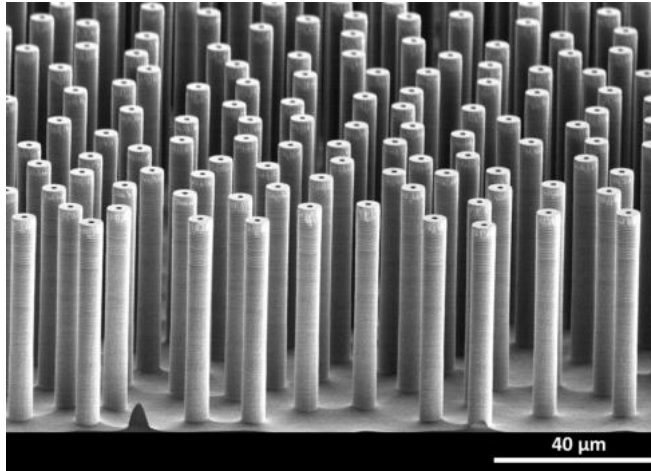
Figure 6.4: SEM image of a sample that has randomly positioned pillars with radius $r = 3$ μm.

A photograph of the full batch of samples before being cut is given in Fig. 6.3(a), where the colorful reflections from the samples with periodically ordered pillar positions are observed. The random samples reveal a silvery appearance. Figure 6.3(b) shows individually cut samples that are placed on glass substrates by double-sided carbon tape, which is done to conveniently attach them to a home-made sample holder during experiments. Fig. 6.4 shows the SEM image of a sample with disordered pillars, that have radius $r = 3$ μm, where the rough surface of the pillars and thin tunnels parallel to the long axes of the pillars are visible. These tunnels are present due to the errors in the lithography process, and they do not reach the bottom of the pillars. The pillar heights are approximately $h = 54$ μm.

6.2.2 Optical setup

Figure 6.5 presents a schematic of the optical setup used in the experiments reported in this chapter. An infrared (IR) Nd:YVO laser ($\lambda = 1064$ nm) is used as the primary light source and a HeNe laser is used for alignment purposes. The IR laser is expanded 4 times by the reflective beam expander (Thorlabs BE04R/M) to create the desired focus spot size by the cylindrical lens ($f = 100$ mm) on the front surface of the sample. The cylindrical lens focuses the incoming beam in the y-direction, while keeping the initial size in x. The line focus is formed on the front surface of the sample (see Fig. 6.7(a)), where the long axis of the pillars are aligned with the y-axis. The measured beamwidth ($1/e^2$) in the y-direction for the IR beam at various z-positions around the focus spot is shown in Fig. 6.6. From these measurements, the y-beamwidth is determined to be $d_{0y} = 50.5 \pm 0.6$ μm and the Rayleigh length is $z_R = 2.4$ mm. This beamwidth ensures that $\approx 86\%$ of the incident beam is within the pillar height $h = 54$ μm. Within the Rayleigh length z_R inside the sample, which has its front surface at the focus

spot, we assume all the directional vectors of the laser are parallel to z-direction.
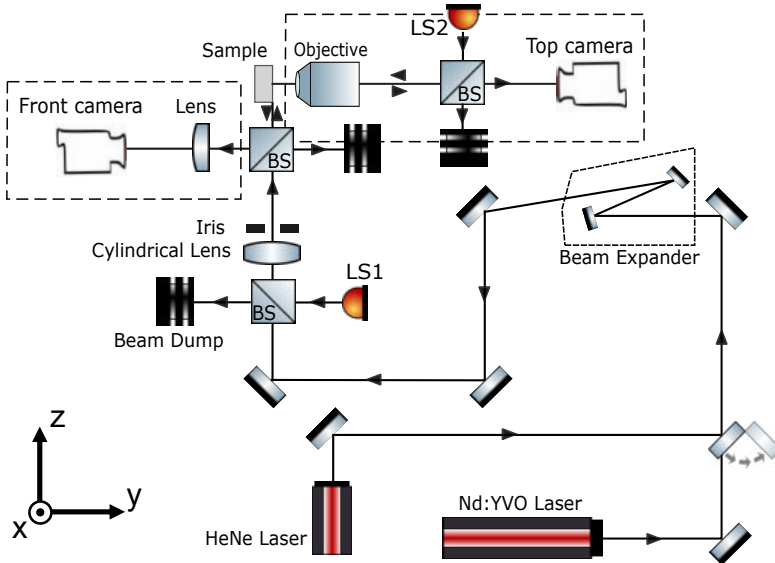
Figure 6.5: Schematic representation of the experimental setup. The Nd:YVO laser is the primary light source and the HeNe laser introduced with the flip mirror is used for alignment purposes. The beam expander expands the beam 4 times. LS1 and LS2 are white light sources that are integrated to the beam paths by beam splitters (BS). The cylindrical lens focuses the incoming beam on the front surface of the sample, where the long axis of the pillars are aligned with the y-axis. The front camera views the front surface of the sample. The scattered light is collected by the objective from the top of the sample, and detected by the top camera.
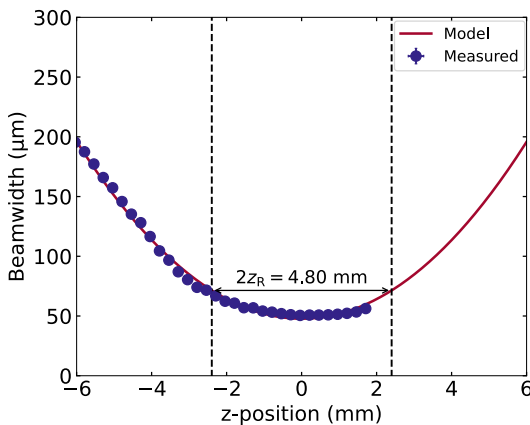
Figure 6.6: Measured beamwidths of IR laser around the focus position $z = 0$. A parabola is fit to the data to estimate the Rayleigh length z_R.

The iris placed after the cylindrical lens blocks stray light and decreases the spot size in the x-direction to make sure only the area with pillars is illuminated, as illustrated in Fig. 6.7(a). The front camera (Guppy Pro F125B) and lens are used to observe the focus spot on the front surface of the sample, to ensure correct positioning of the sample. The sample is attached to a holder that incorporates an assembly of linear stages, that allow movement in three dimensions. When a sample is mounted on the holder for measurement, it is positioned at the focus spot using real-time images acquired by the front camera. LS1 and LS2 are white light sources that are integrated to the beam paths by beam splitters, to illuminate the front and top surface of the sample for alignment purposes. The objective ($NA = 0.25$) and the top camera (Stingray F145B) are used to detect the scattered light from the top. The rectangular area, hereby referred to as a *panel*, viewed by the top camera is illustrated in Fig. 6.7(b). Many panels are measured along the x-axis of each sample to obtain an average result of the samples. The top detection part of the setup, that is the objective, LS2, and the top camera, is attached to linear stage assembly that is capable of moving in three dimensions, which allows scanning the top surface of the sample. Monochromatic images of the rectangular area viewed by the top camera are captured using Vimba Viewer software.
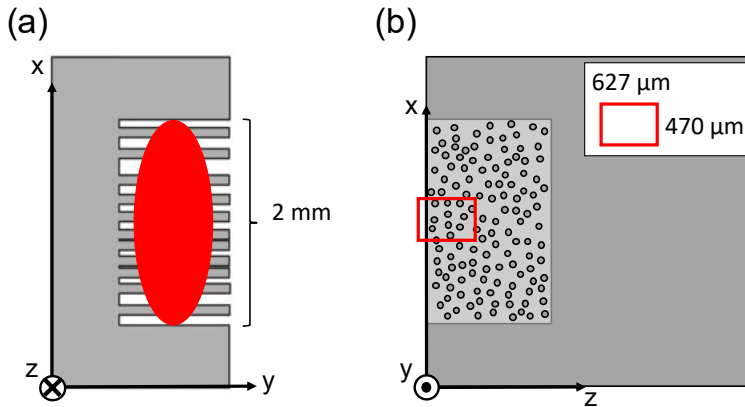
Figure 6.7: Illustration of (a) the front view of the sample with representative elliptical incident beam shape in red, and (b) the top view of the sample with the detected region highlighted by the red rectangle.

6.3 Results and discussions

Fig. 6.8 shows example images captured by the top detection part of the setup. The sample shown has a packing fraction $p = 0.06$ and pillar radius $r = 2$ μm. Fig. 6.8(a) is the image of the sample when it is illuminated by the LS2 from the top (xz surface), and Fig. 6.8(b) is the image of the out-of-plane scattered light from the sample when the IR-laser is incident from the front side (xy surface). It is immediately observed from Fig. 6.8(b) that the IR light becomes extinct

within a short distance from the edge of the sample.
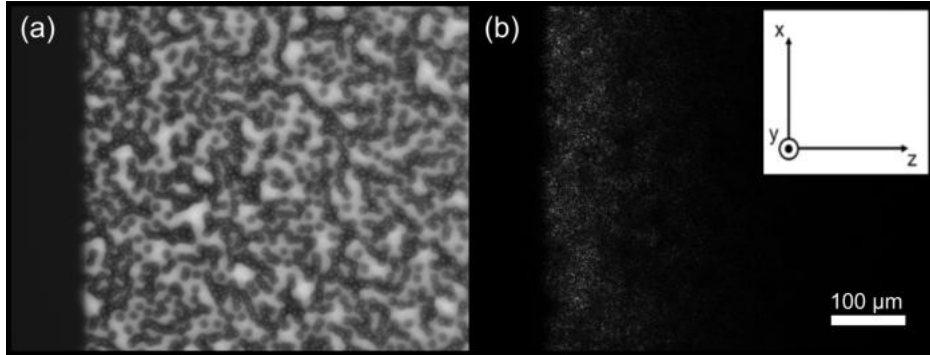
Figure 6.8: Captured images of a panel on a sample with packing fraction $p = 0.06$ and pillar radius $r = 2$ μm, by the top camera. (a) Microscopy image illuminated with white light. (b) Out-of-plane scattered light, with IR laser focused on the front surface of the sample.

The intensity of the light that is scattered out-of-plane, is measured at various panels along the x-direction *on the sample*, as shown in Fig. 6.7. Figure 6.9 shows measurements on one sample at three different panels, which mainly differ in intensity value. The labelling of panel numbers runs from 1 to 20, and consecutive panels overlap due to the limited size of the sample. We do our analysis on panels that do not overlap and are close to the middle of the sample, such as the three panels presented in Fig. 6.9. It is observed from Fig. 6.9, that the detected intensity is lower for panel 5 which is close to the bottom edge of the sample. This is likely due to the intensity of the incident beam being less towards the top and bottom edges of the sample. Another possible reason for the difference in detected intensities is the imperfect mounting of the sample, which could have a slight *tilt* over the z-direction, that would vary the incident intensities for different panels. The samples are mounted with utmost care to prevent this systematic tilt error, and only panels close to the middle of the samples are selected for the analysis. The measured intensity at these panels are averaged to get the position-dependent *diffuse* average intensity $U_{\text{diff}}(z)$ of the sample that is proportional to the diffuse energy density $u_{\text{diff}}(z)$. $U_{\text{diff}}(z)$ here is a *relative* quantity, as we detect a portion of the absolute quantity, limited by the systematic errors and capabilities of the experimental setup. Furthermore, the *tail* on the left side of the edge of the measured curves, potentially includes information about the diffuse reflection from the sample, however, measurements from the front surface would provide better understanding on the reflection of the samples. This work focuses on the z-dependent energy density distribution *inside* the sample, and reflection measurements are left as an outlook.
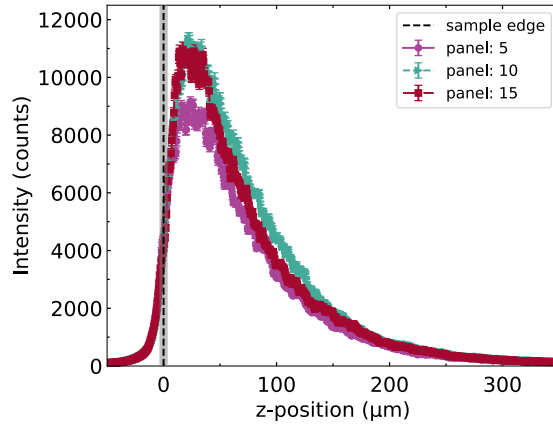
Figure 6.9: Intensity as a function of z-position, measured at three non-overlapping panels on the sample with pillar radius $r = 2$ μm, and packing fraction $p = 0.09$. The edge of the sample is shown as the black dashed line at $z = 0$ μm, and the gray area around it represents the error of the estimated edge position.
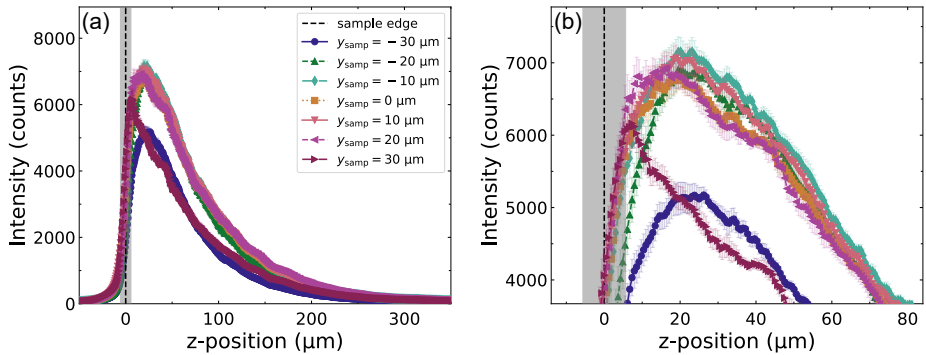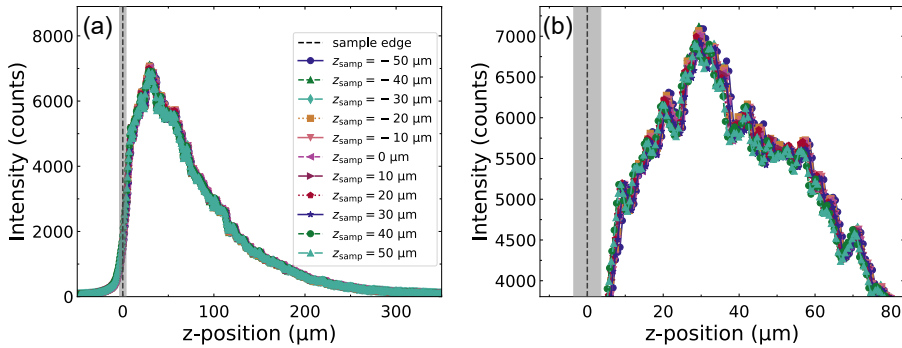

Figure 6.10: (a) Measured intensity as a function of z-position *on the sample*, for a sample placed in various y-positions. $y_{\mathrm{samp}} = 0$ is the standard sample position, where the focus spot is within pillar length. (b) Magnified view of the intensity peaks to highlight the differences between measurements. The pillars on the sample have radius $r = 3$ μm, and the packing fraction is $p = 0.12$. The edge of the sample is shown as black dashed line at $z = 0$ μm, and the gray area around it represents the error of the estimated edge position.

Ensuring precise placement of the sample at the focus spot requires careful alignment, and any deviation from this position leads to systematic measurement errors. Figure 6.10 shows the effect of wrong sample positioning in the y-direction, on the measurement results. The sample reported in Fig. 6.10 has randomly positioned pillars with radius $r = 3$ μm, and a packing fraction $p = 0.12$. The sample is placed in different y-positions, denoted as y_{samp}, around the focus spot

of the IR laser. The IR beam hits the bulk Si substrate at the bottom of the pillars for $y_{samp} = 20$ μm to $y_{samp} = 30$ μm. The light then reflects from the substrate and introduces a sharp peak around 5 μm $< z < 10$ μm to the detected intensity, close to the left edge of the sample as observed in Fig. 6.10(b). For sample placed at $y_{samp} = -30$ μm, it is observed that part of the IR beam misses the pillars and travels in z without interacting with the sample. This part of the light is not detected, thus, for $y_{samp} = -30$ μm the measured intensity is reduced. For the range -20 μm $\leq y_{samp} \leq 10$ μm, the variations in intensity are small, as the majority of the incoming light scatters from the intended parts of the sample.

On the other hand, Fig. 6.11 shows the effect of sample positioning in the z-direction on the measured intensities. The sample is positioned as far as $z_{samp} = \pm 50$ μm and no significant difference is observed in measured intensity. The results shown in Fig. 6.11 agree with our beamwidth measurements, since the tested distances from the standard position $z_{samp} = 0$ μm are much less than the Rayleigh length z_R.

Figure 6.11: (a) Measured intensity as a function of z-position *on the sample*, for a sample placed in various z-positions. $z_{samp} = 0$ is the standard sample position, where the focus spot is at the sample front face. (b) Magnified view of the peaks to highlight the small differences between measurements. The pillars on the sample have radius $r = 3$ μm, and the packing fraction of the sample is $p = 0.12$. The edge of the sample is shown as black dashed line at $z = 0$ μm, and the gray area around it represents the error of the estimated edge position.

6.3.1 Density dependence

Fig. 6.12 shows the measured position-dependent intensity for samples with pillar radius (a) $r = 2$ μm and (b) $r = 3$ μm, with a range of packing fractions up to $p = 0.12$. In both Fig. 6.12(a) and (b), an increase in peak intensity is observed as the packing fraction increases. Furthermore, the intensity distribution is broader for the samples with less scatterers, as the light can penetrate those samples deeper than the denser ones (see Fig. 6.14). Both of these observations agree with the expectations from multiple-scattering samples, as for denser samples the diffuse energy density would be concentrated at $z \approx \ell_{tr}$ which results in

a higher and sharper peak, while for less dense ones, it will spread more in z and reach deeper in the sample. Defect regions that contain either dust particles on the sample or broken pillars, present themselves in measurements as small peaks in intensity. The most visible one in Fig. 6.12(a) is around $z = 200$ μm for sample with $p = 0.12$, and it is caused by a dust particle. It is hard to distinguish the peaks caused by defect regions for samples with low packing fraction, as clustered regions of scatterers also result in similar profiles in the measured intensity. For these samples, we used captured images with white light illumination as shown in Fig. 6.3(a). No defect region was observed within the analysed panels of samples presented Fig. 6.12, except for the one mentioned above for the sample with $r = 2$ μm and $p = 0.12$.
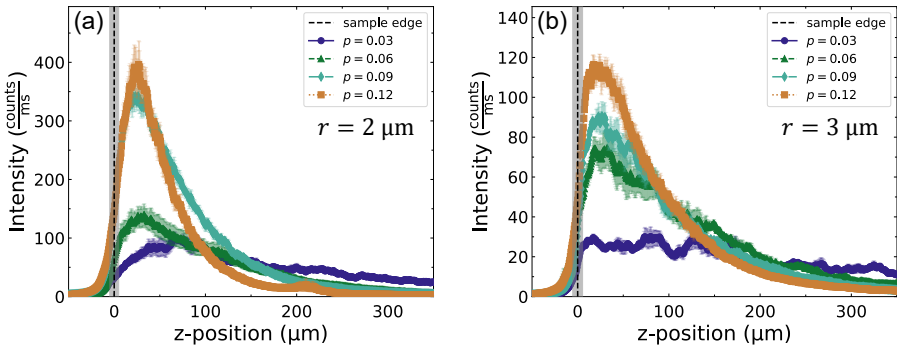
Figure 6.12: Measured intensity as a function of z-position. (a) Measurements of samples that have a pillar radius $r = 2$ μm, and various packing fractions. (b) Measurements of samples that have a pillar radius $r = 3$ μm, and various packing fractions. The edge of the sample is shown as black dashed line at $z = 0$ μm, and the gray area around it represents the error of the estimated edge position. Intensities shown here are divided to the exposure time of each corresponding measurement.

Following references [2, 11], we estimate the transport mean free path ℓ_{tr} of the samples to be on the same order of the distance between the measured $U_{\text{diff}}(z)$ peak and the front surface of the sample. Fig. 6.13 shows the extracted ℓ_{tr} from measurements and approximated ones from Mie calculations, for samples with a range of p. The Mie calculations for a single cylinder with incident unpolarized IR light provide the scattering cross section σ_{scat} and anisotropy g of cylinders with $r = 2$ μm and $r = 3$ μm, which we use to calculate the mean free paths. Fig. 6.13 shows our extracted ℓ_{tr} values agree well with the approximated ones, as they are in the same order of magnitude and show similar trend. The differences are attributed to the systematic errors in our experimental setup and to the fact that our pillars are not perfect cylinders due to the fabrication defects. However, the measured ℓ_{tr} for both sample types are very similar, which is not expected for samples with different pillar radii. This result can also be attributed to the fabrication defects. Moreover, we only present a rough extraction of ℓ_{tr} by considering the maximum point of the intensity peaks, for averaged results over

only three panels on the samples. The low number of panels are due to the limitation of the sample size, as we could only get 3 non-overlapping panels. Consideration of overlapping panels cause enhancement of overlapped regions in the figures, which gives false results.
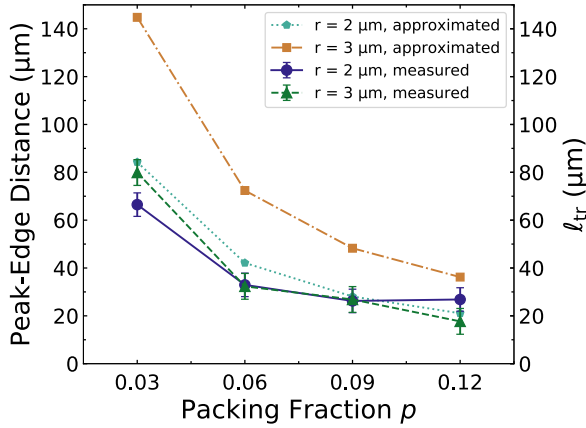
Figure 6.13: Transport mean free path ℓ_{tr} as a function of the sample packing fraction p. Measured ℓ_{tr} are estimated from measurements of samples with pillar radius $r = 2\ \mu m$ and $r = 3\ \mu m$. Approximated ℓ_{tr} are obtained by using the single scatterer properties estimated from Mie calculations for single cylinders with incident unpolarized light. The uncertainties of the extracted results are the variance of the edge position for their respective samples.
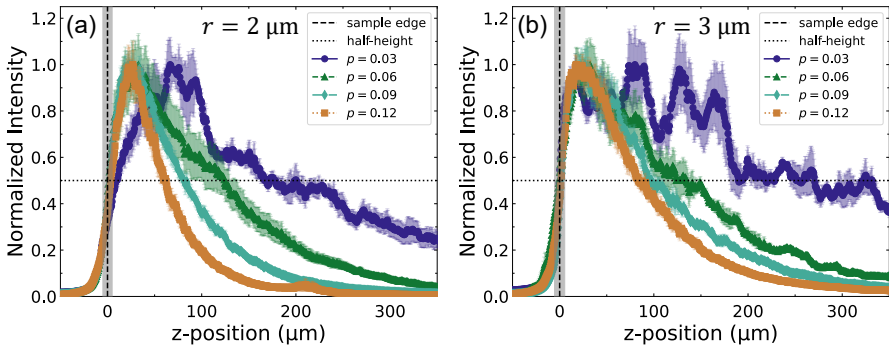
Figure 6.14: Normalized intensity as a function of z-position of samples with (a) pillar radius $r = 2\ \mu m$ and (b) $r = 3\ \mu m$, and various packing fractions. In (a,b) the edge of the sample is shown as black dashed line at $z = 0\ \mu m$, and the gray area around it represents the error of the estimated edge position. The black dotted line is at the half point of the curves.

To better understand the effect of packing fraction on the depth of travel inside

the samples, we normalize the measured intensity to 1, and look at the width of the normalized curves. Fig. 6.14(a) and (b) present the normalized position-dependent intensity of the same measurements shown in Fig. 6.12. Fig. 6.14 highlights the broadening of the intensity distributions with decreasing packing fraction. The full width at half maximum of the measured intensity curves as a function of packing fraction are given in Fig. 6.15, which shows the sample with larger pillar radius have wider peaks in general. This observation agrees with our expectations, since larger pillar radius would mean a larger scattering cross section. In addition, considering that the scatterers are anisotropic, this leads to more diffuse light to be detected deeper inside our sample.
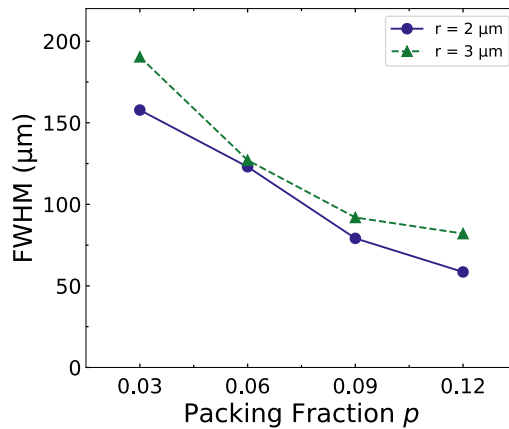
Figure 6.15: Full width half maximum (FWHM) as a function of packing fraction p, of the measured position dependent average intensity curves presented in Fig. 6.14. Measurements for samples with radii $r = 2$ μm and $r = 3$ μm are shown, following Fig. 6.14.

6.4 Summary

In this chapter, we present an experiment to probe the position-dependent energy density inside slabs with randomly positioned silicon (Si) pillars. The pillars are oriented parallel to each other, and are illuminated by IR laser that has a direction perpendicular to the long axis of the pillars. Fabrication defects that cause non-perfect pillars, allow us to monitor the energy distribution inside the samples by measuring the out-of-plane scattering. We infer the position-dependent average intensity, hence, the energy density inside the samples, from the measured intensities that are proportional to both quantities. We explain the fabrication of the samples, the experimental procedures, and present the initial results. These results agree with expectations of such anisotropic, multiple scattering samples, and provide a good initial understanding of our samples.

7 Summary and outlook

In this thesis, we study the light transport through photonic scattering media, that consists of anisotropically scattering and absorbing scatterers. We explore the regions where the common approximations of the transport theory fail to the point of giving unphysical results, and we perform experiments to measure the position-dependent energy density inside samples that are in these regions.

In Chapter 1 we introduce the topic of light scattering, from single- to multiple-scattering, and describe the industrial scattering regime. We also introduce the transport theory, that we use to describe the light transport theoretically. This chapter ends by giving the outline of the thesis.

Chapter 2 reviews the theory of integrating spheres, discusses the substitution error and how it can be solved using double-beam measurements. Experimental measurements are presented, with a 2% error found between single-beam and double-beam measurements. This error is small enough to neglect and the subsequent integrating sphere experiments in this thesis proceeded with single-beam measurements.

Chapter 3 studies the P_1, P_3, and $P_3 + \delta E(4)$ approximations to the radiative transfer equation to model the light transport in photonic scattering media. The unphysical ranges of these approximations are defined in terms of four key parameters; the albedo a, the anisotropy g, the optical thickness b, and the refractive index contrast Δn^2. Relative error maps are provided by comparing the approximations to Monte Carlo simulations. The results show that the P_1 approximation is not suitable to extract the transport parameters or the position-dependent energy density unless the sample only scatters isotropically and elastically. The P_3 and $P_3 + \delta E(4)$ approximations are generally more reliable, except for samples with strong absorption or extreme anisotropy. In the forward scattering range, the $P_3 + \delta E(4)$ approximation showed the best agreement with the Monte Carlo simulations. The results provide a guideline for the applicability of these approximations to interpret experiments on light transport in photonic scattering slabs.

Unphysical ranges and relative error maps of alternative methods to solve the radiative transfer equation, be it by higher order P_N approximations, or by other numerical methods, could be interesting to research. The adequacy of the complexity and the computation time of solutions can differ for each application, and knowing the validity ranges of the methods is crucial. Furthermore, it is also interesting to investigate these methods for different light sources than plane waves with perpendicular incidence to the sample surface. Different angle of incidences and emitters inside the samples are examples to this.

In Chapter 4 we provide the theoretical background for Chapters 3 and 5. The key parameters in transport theory are explained, and the derivations and

solutions of the P_1, P_3, and $P_3+\delta E(4)$ approximations are provided. The effect of internal reflections, which are present in the experiments, and alternative phase functions to the Henyey-Greenstein function are discussed.

Chapter 5 presents a detailed analysis of experimental measurements of the position-dependent energy fluence rate Φ in 3D samples containing anisotropically scattering and absorbing spherical scatterers. A thin capillary filled with quantum dots is used as probe, to detect the position-dependent Φ, and the experimental observations are compared to analytical approximations and Monte Carlo simulations. A comprehensive account of the experimental limitations that prevent an absolute measurement, and an exact match with the models, is provided. Notably, the P_1 and P_3 approximations fail to match the observed trends in Φ, whereas the Monte Carlo simulations and the $P_3 + \delta E(4)$ approximation, exhibit a relatively good agreement with the measured trends of Φ. Continuation of the research conducted in this chapter should start with improving the instabilities and limitations of the measurements,that are listed in Chapter 5. Utilization of a larger integrating sphere with a smaller port fraction, but larger port area to capture all the transmitted and reflected light, will decrease the errors in the extraction of the (a,g) parameters of the samples. Moreover, using well-known samples in experiments allows the extraction of the (a,g) parameters and the phase function for the models from Mie calculations, provided the refractive index and the size of the scatterers are known. A more stable design for the probe holder, that makes sure the capillary stays vertical and efficiently couples the emission from the quantum dots to the fiber of the detector, would decrease the scaling value K in eqn. 5.4. The effect of the probe inside the sample should be further characterized to determine how the light scattered by the probe alters $\Phi(z)$ inside the sample, especially since the sample is finite and internal reflections play a significant role. Possible ways to characterize this effect are measurements and simulations of the angular dependency of the scattered intensity by the probe.

Finally, Chapter 6 reports the preliminary results of position-dependent quasi-2D energy density measurements on quasi-2D samples of randomly positioned pillars etched on a silicon wafer. The energy density is probed by measuring out-of-plane scattering from the top of the samples, when the illumination is done by an IR laser with direction perpendicular to the long axes of the pillars. The laser is focused at the sample surface using a cylindrical lens, to make sure the illumination is only done on the pillars and not the end points of the pillars. These initial results agree with expectations of such anisotropic and multiple scattering samples, however, the experiments need to be improved to draw better conclusions. A specialized sample holder needs to be designed to precisely position the samples at the desired focus spot, to prevent the positioning errors discussed in Chapter 6. Furthermore, an objective with a larger NA would allow more of the scattered light to be collected. A comprehensive investigation is needed to decrease the defects of the samples. Especially, the formation of shallow tunnels in the middle of pillars should be prevented. These tunnels are likely caused by the etching mask alignment. Moreover, larger samples that allow more measurements of non-overlapping panels should be fabricated. After the experiments are im-

proved, the new results should be compared to theoretical expectations, similar to Chapter 5 but for samples with cylindrical scatterers. Reflection measurements from the front surface of the samples can help characterize the samples better, and can be used to further compare the experimental results with theoretical models. These type of samples are also extremely interesting for backscattering cone measurements and localization studies.

In this thesis we studied the light transport inside anisotropically scattering and absorbing samples, specifically the position-dependent energy density in such samples. Our results provide a better understanding of these samples, which common approximations fail to describe the light transport, and provide a guideline to the applicability of analytical models as an alternative to Monte Carlo simulations.

Bibliography

[1] A. Ishimaru. *Wave propagation and scattering in random media*. Vol. I & II. Academic, New York, 1978 (cit. on pp. 11, 15, 17, 31, 33, 47, 48, 50, 55, 57).

[2] M. C. W. van Rossum and T. M. Nieuwenhuizen. "Multiple scattering of classical waves: microscopy, mesoscopy, and diffusion". In: *Rev. Mod. Phys.* **71**.1 (1999), pp. 313–371 (cit. on pp. 11, 12, 13, 14, 17, 105).

[3] E. Akkermans and G. Montambaux. *Mesoscopic Physics of Electrons and Photons*. Cambridge University Press, Cambridge, 2007 (cit. on pp. 11, 13, 84).

[4] D. Wiersma. "Disordered Photonics". In: *Nat. Photonics* **7** (2013), pp. 188–196 (cit. on p. 11).

[5] W. L. Vos, A. Lagendijk, and A. P. Mosk. "Light propagation and emission in complex photonic media". In: *Light Localisation and Lasing: Random and Quasi-random Photonic Structures*. Ed. by M. Ghulinyan and L. Pavesi. Cambridge University Press, Cambridge, 2015, pp. 1–12 (cit. on p. 11).

[6] R. Carminati and J. C. Schotland. *Principles of Scattering and Transport of Light*. Cambridge University Press, Cambridge, 2021 (cit. on pp. 11, 84).

[7] H. C. van de Hulst. *Light Scattering by Small Particles*. Dover Publications, New York, 1981 (cit. on pp. 11, 12, 13, 69).

[8] C. Bohren and D. R. Huffman. *Absorption and Scattering of Light by Small Particles*. Wiley, Weinheim, 1998 (cit. on pp. 11, 12, 32).

[9] A. Lagendijk and B. A. van Tiggelen. "Resonant multiple scattering of light". In: *Phys. Rep.* **270**.3 (1996), pp. 143–215 (cit. on pp. 12, 13, 15, 42).

[10] J. Strutt. "XV. On the light from the sky, its polarization and colour". In: *London Edinburgh Dublin Philos. Mag. J. Sci.* **41**.271 (1871), pp. 107–120 (cit. on pp. 12, 69).

[11] B. Bret. "Multiple light scattering in porous gallium phosphide". PhD thesis. University of Twente, 2005 (cit. on pp. 13, 84, 105).

[12] G. Mie. "Beiträge zur Optik trüber Medien, speziell kolloidaler Metallösungen". In: *Ann. Phys.* **330**.3 (1908), pp. 377–445 (cit. on pp. 13, 69).

[13] J. G. Rivas, R. Sprik, C. M. Soukoulis, K. Busch, and A. Lagendijk. "Optical transmission through strong scattering and highly polydisperse media". In: *EPL* **48**.1 (1999), p. 22 (cit. on p. 13).

[14] R. H. J. Kop, P. de Vries, R. Sprik, and A. Lagendijk. "Observation of Anomalous Transport of Strongly Multiple Scattered Light in Thin Disordered Slabs". In: *Phys. Rev. Lett.* **79**.22 (1997), pp. 4369–4372 (cit. on p. 14).

[15] O. L. Muskens and A. Lagendijk. "Method for broadband spectroscopy of light transport through opaque scattering media". In: *Opt. Lett.* **34**.4 (2009), pp. 395–397 (cit. on p. 14).

[16] T. van der Beek, P. Barthelemy, P. M. Johnson, D. Wiersma, and A. Lagendijk. "Light transport through disordered layers of dense gallium arsenide submicron particles". In: *Phys. Rev. B* **85**.11 (2012) (cit. on pp. 14, 15).

[17] W. L. Vos, T. W. Tukker, A. P. Mosk, A. Lagendijk, and W. L. IJzerman. "Broadband mean free path of diffuse light in polydisperse ensembles of scatterers for white light-emitting diode lighting". In: *Appl. Opt.* **52**.12 (2013), pp. 2602–2609 (cit. on pp. 14, 21, 26, 29).

[18] D. S. Wiersma, P. Bartolini, A. Lagendijk, and R. Righini. "Localization of light in a disordered medium". In: *Nature* **390**.6661 (1997), pp. 671–673 (cit. on p. 14).

[19] P. W. Anderson. "Absence of Diffusion in Certain Random Lattices". In: *Phys. Rev.* **109**.5 (1958), pp. 1492–1505 (cit. on p. 14).

[20] P. Sheng. *Introduction to Wave Scattering, Localization, and Mesoscopic Phenomena.* Academic, San Diego, 1995 (cit. on p. 14).

[21] A. Lagendijk, B. van Tiggelen, and D. S. Wiersma. "Fifty years of Anderson localization". In: *Physics Today* **62**.8 (2009), pp. 24–29 (cit. on p. 14).

[22] W. M. Star, H. P. A. Marijnissen, H. Jansen, M. Keijzer, and M. J. C. van Gemert. "Ligh dosimetry for photodynamic therapy by whole bladder wall irradiation". In: *Photochem. Photobiol.* **46**.5 (1987), pp. 619–624 (cit. on pp. 15, 71).

[23] E. Henderson, B. Lai, and L. Lilge. "Data Acquisition for Interstitial Photodynamic Therapy". In: *Data Acquisition.* Ed. by M. Vadursi. Rijeka: IntechOpen, 2010. Chap. 14 (cit. on pp. 15, 49, 88).

[24] T. C. Zhu, M. M. Kim, J. Padawer, A. Dimofte, M. Potasek, K. Beeson, and E. Parilov. "Light fluence dosimetry in lung-simulating cavities". In: *Optical Methods for Tumor Treatment and Detection: Mechanisms and Techniques in Photodynamic Therapy XXVII.* Ed. by D. H. Kessel and T. Hasan. Vol. 10476. International Society for Optics and Photonics. SPIE, 2018, 104760F (cit. on pp. 15, 71).

[25] S. Kwiatkowski, B. Knap, D. Przystupski, J. Saczko, E. Kędzierska, K. Knap-Czop, J. Kotlińska, O. Michel, K. Kotowski, and J. Kulbacka. "Photodynamic therapy – mechanisms, photosensitizers and combinations". In: *Biomed. Pharmacother.* **106** (2018), pp. 1098–1107 (cit. on p. 15).

[26] F. Shen, Y.-X. Zhou, D.-J. Li, W.-J. Zhu, and M. S. Salama. "Medium resolution imaging spectrometer (MERIS) estimation of chlorophyll-a concentration in the turbid sediment-laden waters of the Changjiang (Yangtze) Estuary". In: *Int. J. Remote Sens.* **31**.17-18 (2010), pp. 4635–4650 (cit. on p. 15).

[27] M. S. Salama and W. Verhoef. "Two-stream remote sensing model for water quality mapping: 2SeaColor". In: *Remote Sens. Environ.* **157** (2015). Special Issue: Remote Sensing of Inland Waters, pp. 111–122 (cit. on p. 15).

[28] F. Shen, W. Verhoef, Y. Zhou, M. S. Salama, and X. Liu. "Satellite Estimates of Wide-Range Suspended Sediment Concentrations in Changjiang (Yangtze) Estuary Using MERIS Data". In: *Estuaries Coasts* **33**.6 (2010), pp. 1420–1429 (cit. on p. 15).

[29] N. P. Majozi, M. S. Salama, S. Bernard, D. M. Harper, and M. G. Habte. "Remote sensing of euphotic depth in shallow tropical inland waters of Lake Naivasha using MERIS data". In: *Remote Sens. Environ.* **148** (2014), pp. 178–189 (cit. on p. 15).

[30] A. de Liz Arcari, J. Tavora, D. van der Wal, and M. S. Salama. "The Wastewater Contamination Index: A methodology to assess the risk of wastewater contamination from satellite-derived water quality indicators". In: *Front. Environ. Sci.* **11** (2023) (cit. on p. 15).

[31] G. R. Fournier and J. L. Forand. "Analytic phase function for ocean water". In: *Ocean Optics XII* **2258** (1994), pp. 194–201 (cit. on pp. 15, 69, 71).

[32] F. Fell and J. Fischer. "Numerical simulation of the light field in the atmosphere–ocean system using the matrix-operator method". In: *J. Quant. Spectrosc. Radiat. Transfer* **69** (2001), pp. 351–388 (cit. on pp. 15, 71).

[33] D. Stramski, E. Boss, D. Bogucki, and K. J. Voss. "The role of seawater constituents in light backscattering in the ocean". In: *Prog. Oceanogr.* **61** (2004), pp. 27–56 (cit. on pp. 15, 71).

[34] T. Nousiainen and K. Kandler. "Light scattering by atmospheric mineral dust particles". In: *Light Scattering Reviews 9: Light Scattering and Radiative Transfer.* Berlin, Heidelberg: Springer Berlin, Heidelberg, 2015, pp. 3–52 (cit. on pp. 15, 71).

[35] C. J. Funk. "Multiple Scattering Calculations of Light Propagation in Ocean Water". In: *Appl. Opt.* **12** (1973), pp. 301–313 (cit. on pp. 15, 71).

[36] N. J. McCormick. "Transport Theory for Optical Oceanography". In: *Computational Methods in Transport.* Ed. by F. Graziani. Berlin, Heidelberg: Springer Berlin, Heidelberg, 2006, pp. 151–163 (cit. on pp. 15, 71).

[37] W. M. Star. "Comparing the P3-approximation with diffusion theory and with Monte Carlo calculations of light propagation in a slab geometry". In: *Dosimetry of Laser Radiation in Medicine and Biology*. Vol. **10305**. SPIE, 1989, pp. 147–155 (cit. on pp. 15, 32, 33, 42, 58, 60, 65, 71, 88).

[38] B. C. Wilson and S. L. Jacques. "Optical reflectance and transmittance of tissues: principles and applications". In: *IEEE J. Quantum Electron.* **26**.12 (1990), pp. 2186–2199 (cit. on pp. 15, 71).

[39] W. F. Cheong, S. A. Prahl, and A. J. Welch. "A review of the optical properties of biological tissues". In: *IEEE J. Quantum Electron.* **26** (1990), pp. 2166–2185 (cit. on pp. 15, 71).

[40] A. Kienle and R. Hibst. "Light Guiding in Biological Tissue due to Scattering". In: *Phys. Rev. Lett.* **97**.1 (2006), p. 018104 (cit. on pp. 15, 71).

[41] S. S. Sekulic, H. W. Ward, D. R. Brannegan, E. D. Stanley, C. L. Evans, S. T. Sciavolino, P. A. Hailey, and P. K. Aldridge. "On-Line Monitoring of Powder Blend Homogeneity by Near-Infrared Spectroscopy". In: *Anal. Chem.* **68** (1996), pp. 509–513 (cit. on p. 15).

[42] T. Burger, J. Kuhn, R. Caps, and J. Fricke. "Quantitative determination of the scattering and absorption coefficients from diffuse reflectance and transmittance measurements: Application to pharmaceutical powders". In: *Appl. Spectrosc.* **51** (1997), pp. 309–317 (cit. on p. 15).

[43] I. Jurič, I. Karlović, I. Tomić, and D. Novaković. "PRINTING: Optical paper properties and their influence on colour reproduction and perceived print quality". In: *Nord. Pulp Pap. Res. J.* **28**.2 (2013), pp. 264–273 (cit. on p. 15).

[44] E. F. Schubert. *Light-Emitting Diodes*. 2nd ed. Cambridge University Press, Cambridge, 2006 (cit. on pp. 15, 16, 71).

[45] M. R. Krames, O. B. Shchekin, R. Mueller-Mach, G. O. Mueller, L. Zhou, G. Harbers, and M. G. Craford. "Status and Future of High-Power Light-Emitting Diodes for Solid-State Lighting". In: *J. Display Technol.* **3**.2 (2007), pp. 160–175 (cit. on pp. 15, 16, 71).

[46] H. Bechtel, P. Schmidt, W. Busselt, and B. S. Schreinemacher. "Lumiramic: a new phosphor technology for high performance solid state light sources". In: *Eighth International Conference on Solid State Lighting*. Ed. by I. T. Ferguson, T. Taguchi, I. E. Ashdown, and S. Park. Vol. 7058. International Society for Optics and Photonics. SPIE, 2008, pp. 64–73 (cit. on pp. 15, 16, 71).

[47] M. L. Meretska, G. Vissenberg, A. Lagendijk, W. L. IJzerman, and W. L. Vos. "Systematic Design of the Color Point of a White LED". In: *ACS Photon.* **6** (2019), pp. 3070–3075 (cit. on pp. 15, 21, 26, 32, 58, 71).

[48] O. S. Ojambati, H. Yılmaz, A. Lagendijk, A. P. Mosk, and W. L. Vos. "Coupling of energy into the fundamental diffusion mode of a complex nanophotonic medium". In: *New J. Phys.* **18**.4 (2016), p. 043032 (cit. on p. 15).

[49] I. M. Vellekoop and A. P. Mosk. "Universal Optimal Transmission of Light Through Disordered Materials". In: *Phys. Rev. Lett.* **101** (2008), 120601: 1–4 (cit. on p. 15).

[50] O. S. Ojambati, A. P. Mosk, I. M. Vellekoop, A. Lagendijk, and W. L. Vos. "Mapping the energy density of shaped waves in scattering media onto a complete set of diffusion modes". In: *Opt. Express* **24**.16 (2016), p. 18525 (cit. on pp. 15, 17).

[51] 2014 Physics Nobel Prize to Akasaki, Amano, and Nakamura. (cit. on p. 16).

[52] M. H. Crawford. "LEDs for Solid-State Lighting: Performance Challenges and Recent Advances". In: *IEEE Journal of Selected Topics in Quantum Electronics* **15**.4 (2009), pp. 1028–1040 (cit. on p. 16).

[53] S. Ye, F. Xiao, Y. Pan, Y. Ma, and Q. Zhang. "Phosphors in phosphor-converted white light-emitting diodes: Recent advances in materials, techniques and properties". In: *Mater. Sci. Eng. R Rep.* **71**.1 (2010), pp. 1–34 (cit. on p. 16).

[54] J. Cho, J. H. Park, J. K. Kim, and E. F. Schubert. "White light-emitting diodes: History, progress, and future". In: *Laser Photonics Rev.* **11**.2 (2017), p. 1600147 (cit. on p. 16).

[55] A. Ishimaru. "Theory and application of wave propagation and scattering in random media". In: *Proc. IEEE* **65**.7 (1977), pp. 1030–1061 (cit. on p. 17).

[56] S. Chandrasekhar. *Radiative Transfer.* Dover Publications, New York, 1960 (cit. on p. 17).

[57] J. H. Tait. *An Introduction to Neutron Transport Theory.* Longmans, London, 1964 (cit. on pp. 17, 18).

[58] S. A. Prahl, M. Keijzer, S. L. Jacques, and A. J. Welch. "A Monte Carlo model of light propagation in tissue". In: *Dosimetry of Laser Radiation in Medicine and Biology.* Ed. by G. J. Mueller, D. H. Sliney, and R. F. Potter. Vol. 10305. International Society for Optics and Photonics. SPIE, 1989, pp. 105–114 (cit. on pp. 17, 32, 36, 37, 71).

[59] S. Mujumdar, R. Torre, H. Ramachandran, and D. S. Wiersma. "Monte Carlo calculations of spectral features in random lasing". In: *J. Nanophotonics* **4** (2010), pp. 1–13 (cit. on pp. 17, 71).

[60] S. L. Jacques. "Monte Carlo modeling of light transport in tissue (Steady state and time of flight)". In: *Optical-Thermal Response of Laser-Irradiated Tissue.* Springer Netherlands, 2011, pp. 109–144 (cit. on pp. 17, 36, 37, 71).

[61] M. Atif, A. Khan, and M. Ikram. "Modeling of light propagation in turbid medium using Monte Carlo simulation technique". In: *Opt. Spectrosc.* **111** (2011), pp. 107–112 (cit. on pp. 17, 71).

[62]   R. Uppu and S. Mujumdar. "Dependence of the Gaussian-Lévy transition on the disorder strength in random lasers". In: *Phys. Rev. A* **87**.1 (2013), p. 013822 (cit. on pp. 17, 71).

[63]   A. A. Leino, A. Pulkkinen, and T. Tarvainen. "ValoMC: a Monte Carlo software and MATLAB toolbox for simulating light transport in biological tissue". In: *OSA Contin.* **2**.3 (2019), pp. 957–972 (cit. on pp. 17, 18, 71).

[64]   J. Jönsson and E. Berrocal. "Multi-Scattering software: part I: online accelerated Monte Carlo simulation of light transport through scattering media". In: *Opt. Express* **28** (2020), pp. 37612–37638 (cit. on pp. 17, 18, 71).

[65]   M. G. Cooper, L. C. Smith, A. K. Rennermalm, M. Tedesco, R. Muthyala, S. Z. Leidman, S. E. Moustafa, and J. V. Fayne. "Spectral attenuation coefficients from measurements of light transmission in bare ice on the Greenland Ice Sheet". In: *Cryosphere* **15** (2021), pp. 1931–1953 (cit. on pp. 17, 71).

[66]   A. Krieger and S. Wolf. "The scattering order problem in Monte Carlo radiative transfer". In: *Astron. Astrophys.* **645** (2021), A143 (cit. on pp. 17, 71).

[67]   R. W. Shonkwiler and F. Mendivil. *Explorations in Monte Carlo Methods.* Springer, New York, 2009 (cit. on pp. 17, 71).

[68]   J. H. Joseph, W. L. Wiscombe, and J. A. Weinman. "The delta-Eddington approximation for radiative flux transfer". In: *J. Atmos. Sci.* **33** (1976), pp. 2452–24593 (cit. on p. 18).

[69]   W. M. Star, J. P. A. Marijnissen, and M. J. C. van Gemert. "Light dosimetry in optical phantoms and in tissues: I. Multiple flux and transport theory". In: *Phys. Med. Biol.* **33**.4 (1988) (cit. on pp. 18, 32, 53, 58, 60, 65).

[70]   M. Keijzer, W. M. Star, and P. R. M. Storchi. "Optical diffusion in layered media". In: *Appl. Opt.* **27**.9 (1988), pp. 1820–1824 (cit. on pp. 18, 60).

[71]   D. Dickey, O. Barajas, K. Brown, J. Tulip, and R. B. Moore. "Radiance modelling using the P3 approximation". In: *Phys. Med. Biol.* **43** (1998), pp. 3559–3570 (cit. on pp. 18, 32).

[72]   H. Egger and M. Schlottbom. "An Lp theory for stationary radiative transfer". In: *Appl. Anal.* **93**.6 (2014), pp. 1283–1296 (cit. on p. 18).

[73]   A. Liemert and A. Kienle. "Analytical solution of the radiative transfer equation for infinite-space fluence". In: *Phys. Rev. A* **83**.1 (2011), p. 015804 (cit. on p. 18).

[74]   A. Liemert, S. Geiger, and A. Kienle. "Solutions for single-scattered radiance in the semi-infinite medium based on radiative transport theory". In: *J. Opt. Soc. Am. A* **38**.3 (2021), pp. 405–411 (cit. on pp. 18, 60).

[75]   J. D. Jackson. *Classical electrodynamics.* New York: Wiley, 1998 (cit. on p. 18).

[76] G. B. Arfken and H. J. Weber. *Mathematical Methods for Physicists*. Elsevier, Boston, 2005 (cit. on pp. 18, 52, 53, 54).

[77] K. M. Case and P. F. Zweifel. *Linear Transport Theory*. Addison-Wesley Series in Nuclear Engineering. Addison-Wesley Pub. Co., Reading, Mass., 1967 (cit. on pp. 18, 56).

[78] V. A. Markel. "Modified spherical harmonics method for solving the radiative transport equation". In: *Waves in Random Media* **14**.1 (2003), p. L13 (cit. on p. 18).

[79] A. R. Gardner, A. D. Kim, and V. Venugopalan. "Radiative transport produced by oblique illumination of turbid media with collimated beams." In: *Phys. Rev. E* **87**.6 (2013), p. 063308 (cit. on p. 18).

[80] D. Reitzle, S. Geiger, A. Liemert, and A. Kienle. "Semianalytical solution for the transient temperature in a scattering and absorbing slab consisting of three layers heated by a light source". In: *Sci. Rep.* **11**.1 (2021), p. 8424 (cit. on p. 18).

[81] V. Y. F. Leung, A. Lagendijk, T. W. Tukker, A. P. Mosk, W. L. IJzerman, and W. L. Vos. "Interplay between multiple scattering, emission, and absorption of light in the phosphor of a white light-emitting diode". In: *Opt. Express* **22**.7 (2014), pp. 8190–8204 (cit. on p. 21).

[82] M. L. Meretska, R. Uppu, G. Vissenberg, A. Lagendijk, W. L. IJzerman, and W. L. Vos. "Analytical modeling of light transport in scattering materials with strong absorption". In: *Opt. Express* **25** (2017), A906–A921 (cit. on pp. 21, 32, 37, 43, 57).

[83] K. Suzuki, A. Kobayashi, S. Kaneko, K. Takehira, T. Yoshihara, H. Ishida, Y. Shiina, S. Oishi, and S. Tobita. "Reevaluation of absolute luminescence quantum yields of standard solutions using a spectrometer with an integrating sphere and a back-thinned CCD detector". In: *Phys. Chem. Chem. Phys.* **11**.42 (2009), pp. 9850–9860 (cit. on p. 21).

[84] C. Würth, M. Grabolle, J. Pauli, M. Spieles, and U. Resch-Genger. "Relative and absolute determination of fluorescence quantum yields of transparent samples". In: *Nat. Protoc.* **8** (2013), pp. 1535–1550 (cit. on p. 21).

[85] N. Stambler and Z. Dubinsky. "Corals as light collectors: an integrating sphere approach". In: *Coral Reefs* **24**.1 (2005), pp. 1–9 (cit. on p. 21).

[86] W. L. Vos, M. Donze, and H. Buiteveld. "On the reflectance spectrum of algae in water: The nature of the peak at 700 nm and its shift with varying concentration". In: *Communications on Sanitary Engineering and Water Management* 7 (1986), pp. 86–22 (cit. on p. 21).

[87] R. J. Ritchie and S. Sma-Air. "Using integrating sphere spectrophotometry in unicellular algal research". In: *J. Appl. Phycol.* **32**.5 (2020), pp. 2947–2958 (cit. on p. 21).

[88]   E. Zamora-Rojas, B. Aernouts, A. Garrido-Varo, D. Pérez-Marín, J. E. Guerrero-Ginel, and W. Saeys. "Double integrating sphere measurements for estimating optical properties of pig subcutaneous adipose tissue". In: *Innov. Food Sci. Emerg. Technol.* **19** (2013), pp. 218–226 (cit. on p. 21).

[89]   A. López-Maestresalas, B. Aernouts, R. Van Beers, S. Arazuri, C. Jarén, J. De Baerdemaeker, and W. Saeys. "Bulk Optical Properties of Potato Flesh in the 500–1900 nm Range". In: *Food Bioproc Tech* **9**.3 (2016), pp. 463–470 (cit. on p. 21).

[90]   R. Van Beers, B. Aernouts, R. Watté, A. Schenk, B. Nicolaï, and W. Saeys. "Effect of maturation on the bulk optical properties of apple skin and cortex in the 500–1850 nm wavelength range". In: *J. Food Eng.* **214** (2017), pp. 79–89 (cit. on p. 21).

[91]   R. Lu, R. Van Beers, W. Saeys, C. Li, and H. Cen. "Measurement of optical properties of fruits and vegetables: A review". In: *Postharvest Biol. Technol.* **159** (2020), p. 111003 (cit. on p. 21).

[92]   K. Carr. "Integrating sphere theory and applications Part I: Integrating sphere theory and design". In: *Surf. Coat. Int.* **80**.8 (1997), pp. 380–385 (cit. on pp. 21, 27).

[93]   K. Grandin and A. Roos. "Evaluation of correction factors for transmittance measurements in single-beam integrating spheres". In: *Appl. Opt.* **33**.25 (1994), pp. 6098–6104 (cit. on pp. 26, 27).

[94]   P. Nostell, A. Roos, and D. Rönnow. "Single-beam integrating sphere spectrophotometer for reflectance and transmittance measurements versus angle of incidence in the solar wavelength range on diffuse and specular samples". In: *Rev. Sci. Instrum.* **70**.5 (1999), pp. 2481–2494 (cit. on p. 26).

[95]   F. J. J. Clarke and J. A. Compton. "Correction methods for integrating-sphere measurement of hemispherical reflectance". In: *Color Res. Appl.* **11**.4 (1986), pp. 253–262 (cit. on p. 27).

[96]   A. Springsteen. *A guide to reflectance spectroscopy.* Labsphere (cit. on p. 27).

[97]   L. Vidovič and B. Majaron. "Elimination of single-beam substitution error in diffuse reflectance measurements using an integrating sphere". In: *J. Biomed. Opt.* **19**.2 (2014), p. 027006 (cit. on p. 27).

[98]   O. Akdemir, A. Lagendijk, and W. L. Vos. "Breakdown of light transport models in photonic scattering slabs with strong absorption and anisotropy". In: *Phys. Rev. A* **105**.3 (2022), p. 033517 (cit. on pp. 31, 71, 83, 85, 88).

[99]   Ref. [100] is an early version of chapter 3 and 4. Several differences are that they did not consider internal reflection (thus effectively taking $\Delta n^2 = 0$), nor the $P_3 + \delta E(4)$ approximation. Last but not least there are some inconsistencies in the theoretical derivation and the scaling. (cit. on p. 31).

[100] M. L. Meretska, R. Uppu, A. Lagendijk, and W. L. Vos. "Universal Validity Ranges of Diffusion Theory for Light and Other Electromagnetic Waves". In: *arXiv* (2019) (cit. on pp. 31, 33, 120).

[101] A. Lagendijk, R. Vreeker, and P. de Vries. "Influence of internal reflection on diffusive transport in strongly scattering media". In: *Phys. Lett. A* **136** (1989), pp. 81–88 (cit. on p. 31).

[102] J. X. Zhu, D. J. Pine, and D. A. Weitz. "Internal reflection of diffusive light in random media". In: *Phys. Rev. A* **44**.6 (1991), pp. 3948–3959 (cit. on p. 31).

[103] Y. Bayazitoglu and J. Higenyi. "Higher-Order Differential Equations of Radiative Transfer: P3 Approximation". In: *AIAA J.* **17** (1979), pp. 424–431 (cit. on p. 32).

[104] A. Liemert and A. Kienle. "Explicit solutions of the radiative transport equation in the P3 approximation". In: *Medical Physics* **41**.11 (2014), p. 111916 (cit. on pp. 32, 57, 60).

[105] W. E. Meador and W. R. Weaver. "Diffusion approximation for large absorption in radiative transfer". In: *Appl. Opt.* **18** (1979), pp. 1204–1208 (cit. on pp. 32, 65).

[106] E. Hecht. *Optics.* Pearson Education Limited, Harlow, 2016 (cit. on p. 32).

[107] J. Olmos-Trigo, C. Sanz-Fernández, D. R. Abujetas, J. Lasa-Alonso, N. de Sousa, A. Garcia-Etxarri, J. A. Sánchez-Gil, G. Molina-Terriza, and J. J. Sáenz. "Kerker Conditions upon Lossless, Absorption, and Optical Gain Regimes". In: *Phys. Rev. Lett.* **125**.7 (2020), p. 073205 (cit. on p. 33).

[108] M. Kerker, D.-S. Wang, and C. L. Giles. "Electromagnetic scattering by magnetic spheres". In: *J. Opt. Soc. Am.* **73**.6 (1983), pp. 765–767 (cit. on p. 33).

[109] L. G. Henyey and J. L. Greenstein. "Diffuse radiation in the Galaxy". In: *Astrophys. J.* **93** (1941), pp. 70–83 (cit. on pp. 36, 47, 53, 85).

[110] J. G. Rivas. "Light in strongly scattering semiconductors. Diffuse transport and Anderson localization". PhD thesis. University of Amsterdam, 2002 (cit. on p. 37).

[111] H. C. van de Hulst. *Multiple Light Scattering.* Vol. 2. Academic Press, New York, 1980 (cit. on pp. 37, 45).

[112] J. F. Epperson. *An Introduction to Numerical Methods and Analysis.* 2nd. Wiley, New Jersey, 2013 (cit. on p. 38).

[113] S. L. Jacques, C. A. Alter, and S. A. Prahl. "Angular dependence of HeNe laser light scattering by human dermis". In: *Lasers Life Sci.* **1**.4 (1987), pp. 309–333 (cit. on p. 42).

[114] A. Krasnoshchoka, A. K. Hansen, A. Thorseth, D. Marti, P. M. Petersen, X. Jian, and O. B. Jensen. "Phosphor material dependent spot size limitations in laser lighting". In: *Opt. Express* **28**.4 (2020), pp. 5758–5767 (cit. on p. 43).

[115]   I. Seo, C. K. Hayakawa, and V. Venugopalan. "Radiative transport in the delta-P1 approximation for semi-infinite turbid media". In: *Med Phys* **35**.2 (2008), pp. 681–693 (cit. on p. 57).

[116]   F. Martelli, S. D. Bianco, A. Ismaelli, and G. Zaccanti. *Light Propagation through Biological Tissue and Other Diffusive Media: Theory, Solutions, and Software*. SPIE, Bellingham, Washington, 2010 (cit. on p. 57).

[117]   M. F. Modest. *Radiative Heat Transfer*. Academic, London, 2003 (cit. on p. 60).

[118]   B. W. Fowler. "Expansion of Mie-theory phase functions in series of Legendre polynomials". In: *J. Opt. Soc. Am.* **73**.1 (1983), pp. 19–22 (cit. on p. 69).

[119]   C. Junge. "The size distribution and aging of natural aerosols as determined from electrical and optical data on the atmosphere". In: *J. Atmos. Sci* **12**.1 (1955), pp. 13–25 (cit. on p. 70).

[120]   W. M. Cornette and J. G. Shanks. "Physically reasonable analytic expression for the single-scattering phase function". In: *Appl. Opt.* **31**.16 (1992), pp. 3152–3160 (cit. on p. 70).

[121]   B. T. Draine. "Scattering by Interstellar Dust Grains. I. Optical and Ultraviolet". In: *Astrophys. J.* **598**.2 (2003), p. 1017 (cit. on p. 70).

[122]   P. Liu. "A new phase function approximating to Mie scattering for radiative transport equations". In: *Phys. Med. Biol.* **39**.6 (1994), p. 1025 (cit. on p. 70).

[123]   G. Dolgos and J. V. Martins. "Polarized Imaging Nephelometer for in situ airborne measurements of aerosol light scattering". In: *Opt. Express* **22**.18 (2014), pp. 21972–21990 (cit. on p. 71).

[124]   R. Boiger, R. L. Modini, A. Moallemi, D. Degen, A. Adelmann, and M. Gysel-Beer. "Retrieval of aerosol properties from in situ, multi-angle light scattering measurements using invertible neural networks". In: *J. Aerosol Sci.* **163** (2022), p. 105977 (cit. on p. 71).

[125]   Q. Chen, Q. Chen, S. Liu, and X. Luo. "A Design for In-Situ Measurement of Optical Degradation of High Power Light-Emitting Diodes Under Accelerated Life Test". In: *IEEE Trans. Device Mater.* **14**.2 (2014), pp. 645–650 (cit. on p. 71).

[126]   N. Pomerleau-Dalcourt and L. Lilge. "Development and characterization of multi-sensory fluence rate probes". In: *Phys. Med. Biol.* **51**.7 (2006), p. 1929 (cit. on p. 71).

[127]   X. Li, J. M. Zhao, C. C. Wang, and L. H. Liu. "Improved transmission method for measuring the optical extinction coefficient of micro/nano particle suspensions". In: *Appl. Opt.* **55**.29 (2016), pp. 8171–8179 (cit. on p. 77).

[128] X. Ma, J. Q. Lu, R. S. Brock, K. M. Jacobs, P. Yang, and X.-H. Hu. "Determination of complex refractive index of polystyrene microspheres from 370 to 1610 nm". In: *Phys. Med. Biol.* **48**.24 (2003), p. 4165 (cit. on p. 82).

[129] A. F. Koenderink. "Emission and transport of light in photonic crystals". PhD thesis. University of Amsterdam, 2003 (cit. on p. 84).

[130] S. L. Jacques. "Light Distributions from Point, Line and Plane Sources for Photochemical Reactions and Fluorescence in Turbid Biological Tissues". In: *Photochem. Photobiol.* **67**.1 (1998), pp. 23–32 (cit. on p. 88).

[131] Y. H. Ong and T. C. Zhu. "Analytic function for predicting light fluence rate of circular fields on a semi-infinite turbid medium". In: *Opt. Express* **24**.23 (2016), pp. 26261–26281 (cit. on p. 88).

[132] Y. Guo, N. Zeng, H. He, C. Liu, E. Du, Y. He, and H. Ma. "Retardance of bilayer anisotropic samples consisting of well-aligned cylindrical scatterers and birefringent media". In: *J. Biomed. Opt.* **21**.5 (2016), p. 055002 (cit. on p. 95).

[133] P. Krauter, C. Zoller, and A. Kienle. "Double anisotropic coherent backscattering of light". In: *Opt. Lett.* **43**.8 (2018), pp. 1702–1705 (cit. on p. 95).

[134] T. Sun, T. Liu, H. He, J. Wu, and H. Ma. "Distinguishing anisotropy orientations originated from scattering and birefringence of turbid media using Mueller matrix derived parameters". In: *Opt. Lett.* **43**.17 (2018), pp. 4092–4095 (cit. on p. 95).

[135] K. J. Parker. "Shapes and distributions of soft tissue scatterers". In: *Phys. Med. Biol.* **64**.17 (2019), p. 175022 (cit. on p. 95).

[136] M. Dobson, F. Ulaby, T. LeToan, A. Beaudoin, E. Kasischke, and N. Christensen. "Dependence of radar backscatter on coniferous forest biomass". In: *IEEE Trans. Geosci. Remote Sens.* **30**.2 (1992), pp. 412–415 (cit. on p. 95).

[137] T. Le Toan, A. Beaudoin, J. Riom, and D. Guyon. "Relating forest biomass to SAR data". In: *IEEE Trans. Geosci. Remote Sens.* **30**.2 (1992), pp. 403–411 (cit. on p. 95).

[138] Y. Dong and J. Richards. "Studies of the cylinder-ground double bounce scattering mechanism in forest backscatter models". In: *IEEE Trans. Geosci. Remote Sens.* **33**.1 (1995), pp. 229–231 (cit. on p. 95).

[139] K. Sarabandi and I.-S. Koh. "A complete physics-based channel parameter simulation for wave propagation in a forest environment". In: *EEE Trans. Antennas Propag.* **49**.2 (2001), pp. 260–271 (cit. on p. 95).

[140] H. Huang, L. Tsang, A. Colliander, and S. H. Yueh. "Propagation of Waves in Randomly Distributed Cylinders Using Three-Dimensional Vector Cylindrical Wave Expansions in Foldy–Lax Equations". In: *IEEE J. Multiscale Multiphysics Comput. Tech.* **4** (2019), pp. 214–226 (cit. on p. 95).

[141] M. A. C. Potenza, S. Albani, B. Delmonte, S. Villa, T. Sanvito, B. Paroli, A. Pullia, G. Baccolo, N. Mahowald, and V. Maggi. "Shape and size constraints on dust optical properties from the Dome C ice core, Antarctica". In: *Sci. Rep.* **6**.1 (2016), p. 28162 (cit. on pp. 95, 96).

[142] B. Jaiswal, G. Mahapatra, A. Nandi, M. Sudhakar, K. Sankarasubramanian, and V. Sheel. "Polarization signatures of Mars dust and clouds: Prospects for future spacecraft observations". In: *Planet. Space Sci.* **201** (2021), p. 105193 (cit. on p. 95).

[143] B. A. van Tiggelen, R. Maynard, and A. Heiderich. "Anisotropic Light Diffusion in Oriented Nematic Liquid Crystals". In: *Phys. Rev. Lett.* **77** (4 1996), pp. 639–642 (cit. on p. 95).

[144] H. Stark and T. C. Lubensky. "Multiple Light Scattering in Nematic Liquid Crystals". In: *Phys. Rev. Lett.* **77** (11 1996), pp. 2229–2232 (cit. on p. 95).

[145] B. van Tiggelen and H. Stark. "Nematic liquid crystals as a new challenge for radiative transfer". In: *Rev. Mod. Phys.* **72** (4 2000), pp. 1017–1039 (cit. on pp. 95, 96).

[146] R. Sapienza, S. Mujumdar, C. Cheung, A. G. Yodh, and D. Wiersma. "Anisotropic Weak Localization of Light". In: *Phys. Rev. Lett.* **92** (3 2004), p. 033903 (cit. on p. 95).

[147] D. S. Wiersma, A. Muzzi, M. Colocci, and R. Righini. "Time-Resolved Anisotropic Multiple Light Scattering in Nematic Liquid Crystals". In: *Phys. Rev. Lett.* **83** (21 1999), pp. 4321–4324 (cit. on p. 95).

[148] P. M. Johnson, B. P. J. Bret, J. G. Rivas, J. J. Kelly, and A. Lagendijk. "Anisotropic Diffusion of Light in a Strongly Scattering Material". In: *Phys. Rev. Lett.* **89** (24 2002), p. 243901 (cit. on pp. 95, 96).

[149] O. K. Dudko, G. H. Weiss, V. Chernomordik, and A. H. Gandjbakhche. "Photon migration in turbid media with anisotropic optical properties". In: *Phys. Med. Biol.* **49**.17 (2004), p. 3979 (cit. on p. 95).

[150] S. Nickell, M. Hermann, M. Essenpreis, T. J. Farrell, U. Krämer, and M. S. Patterson. "Anisotropy of light propagation in human skin". In: *Phys. Med. Biol.* **45**.10 (2000), p. 2873 (cit. on p. 95).

[151] A. Kienle, F. K. Forster, and R. Hibst. "Anisotropy of light propagation in biological tissue". In: *Opt. Lett.* **29**.22 (2004), pp. 2617–2619 (cit. on p. 95).

[152] A. Kienle, F. Foschum, and A. Hohmann. "Light propagation in structural anisotropic media in the steady-state and time domains". In: *Phys. Med. Biol.* **58**.17 (2013), p. 6205 (cit. on p. 95).

[153] M. B. van der Mark. "Propagation of light in disordered media: A search for Anderson localization". PhD thesis. University of Amsterdam, 1990 (cit. on p. 95).

[154] A. Kienle, C. D'Andrea, F. Foschum, P. Taroni, and A. Pifferi. "Light propagation in dry and wet softwood". In: *Opt. Express* **16**.13 (2008), pp. 9895–9906 (cit. on p. 96).

[155] A. Kienle, C. Wetzel, A. L. Bassi, D. Comelli, P. Taroni, and A. Pifferi. "Determination of the optical properties of anisotropic biological media using an isotropic diffusion model". In: *J. Biomed. Opt.* **12**.1 (2007), p. 014026 (cit. on p. 96).

[156] M. P. van Albada and A. Lagendijk. "Observation of Weak Localization of Light in a Random Medium". In: *Phys. Rev. Lett.* **55**.24 (1985), pp. 2692–2695 (cit. on p. 97).

[157] M. B. van der Mark, M. P. van Albada, and A. Lagendijk. "Light scattering in strongly scattering media: Multiple scattering and weak localization". In: *Phys. Rev. B* **37**.7 (1988), pp. 3575–3592 (cit. on p. 97).

[158] O. L. Muskens and A. Lagendijk. "Broadband enhanced backscattering spectroscopy of strongly scattering media". In: *Opt. Express* **16**.2 (2008), pp. 1222–1231 (cit. on p. 97).

[159] O. L. Muskens, A. F. Koenderink, and W. L. Vos. "Broadband coherent backscattering spectroscopy of the interplay between order and disorder in three-dimensional opal photonic crystals". In: *Phys. Rev. B* **83**.15 (2011), p. 155101 (cit. on p. 97).

[160] O. L. Muskens, T. van der Beek, and A. Lagendijk. "Angle dependence of the frequency correlation in random photonic media: Diffusive regime and its breakdown near localization". In: *Phys. Rev. B* **84**.3 (2011), p. 035106 (cit. on p. 97).

[161] P. M. Johnson, S. Faez, and A. Lagendijk. "Full characterization of anisotropic diffuse light". In: *Opt. Express* **16**.10 (2008), pp. 7435–7446 (cit. on p. 97).

[162] R. Uppu, M. Adhikary, C. A. M. Harteveld, and W. L. Vos. "Spatially Shaping Waves to Penetrate Deep inside a Forbidden Gap". In: *Phys. Rev. Lett.* **126**.17 (2021), p. 177402 (cit. on p. 97).

[163] M. J. Goodwin, C. A. M. Harteveld, M. J. de Boer, and W. L. Vos. "Deep reactive ion etching of cylindrical nanopores in silicon for photonic crystals". In: *Nanotechnology* **34**.22 (2023), p. 225301 (cit. on p. 97).

Nederlandse samenvatting

In dit proefschrift bestuderen we het lichttransport in fotonische verstrooiingsmedia, bestaande uit anisotrope verstrooiende en absorberende deeltjes. We onderzoeken de gebieden waar de gangbare benaderingen van de transporttheorie falen en onfysische resultaten opleveren. Daarnaast voeren we experimenten uit om de positieafhankelijke energiedichtheid binnen monsters in deze gebieden te meten.

In Hoofdstuk 1 hebben we het onderwerp lichtverstrooiing geïntroduceerd, van enkele- tot meervoudige verstrooiing, en hebben we het industriële verstrooiingsregime beschreven. We hebben ook de transporttheorie geïntroduceerd, die we theoretisch gebruiken om het lichttransport te beschrijven. Dit hoofdstuk eindigt met een overzicht van het proefschrift.

Hoofdstuk 2 behandelt de theorie van integrerende bollen, bespreekt de substitutiefout en hoe deze kan worden opgelost met dubbelstraalmetingen. Experimentele metingen worden gepresenteerd, waarbij een fout van 2% wordt gevonden tussen enkelstraal- en dubbelstraalmetingen. Deze fout is klein genoeg om te verwaarlozen, en de daaropvolgende experimenten met integrerende bollen in dit proefschrift werden uitgevoerd met enkelstraalmetingen.

Hoofdstuk 3 bestudeert de P_1, P_3 en $P_3 + \delta E(4)$ benaderingen van de stralingsoverdrachtvergelijking om het lichttransport in fotonische verstrooiingsmedia te modelleren. De onfysische bereiken van deze benaderingen worden gedefinieerd in termen van vier belangrijke parameters: de albedo a, de anisotropie g, de optische dikte b en het brekingsindexcontrast Δn^2. Relatieve foutenkaarten worden gegeven door de benaderingen te vergelijken met Monte Carlo-simulaties. De resultaten tonen aan dat de P_1-benadering niet geschikt is om de transportparameters of de positie-afhankelijke energiedichtheid te bepalen, tenzij het monster alleen isotroop en elastisch verstrooit. De P_3 en $P_3 + \delta E(4)$ benaderingen zijn over het algemeen betrouwbaarder, behalve voor monsters met sterke absorptie of extreme anisotropie. In het voorwaartse verstrooiingsbereik vertoont de $P_3 + \delta E(4)$ benadering de beste overeenkomst met de Monte Carlo-simulaties. De resultaten geven een richtlijn voor de toepasbaarheid van deze benaderingen bij het interpreteren van experimenten over lichttransport in fotonische verstrooiingsslabben.

Het kan interessant zijn om onfysische bereiken en relatieve foutenkaarten van alternatieve methoden om de stralingsoverdrachtvergelijking op te lossen te onderzoeken, of het nu gaat om hogere orde P_N-benaderingen of andere numerieke methoden. De geschiktheid van de complexiteit en de rekentijd van de oplossingen kan verschillen voor elke toepassing, en het kennen van de geldigheidsgebieden van de methoden is cruciaal. Bovendien is het interessant om deze methoden te onderzoeken voor andere lichtbronnen dan vlakke golven met loodrechte inval op

het monsteroppervlak. Voorbeelden hiervan zijn verschillende invalshoeken en emitters binnenin de monsters.

In Hoofdstuk 4 geven we de theoretische achtergrond voor Hoofdstukken 3 en 5. De belangrijkste parameters in de transporttheorie worden uitgelegd, en de afleidingen en oplossingen van de P_1, P_3 en $P_3 + \delta E(4)$ benaderingen worden gegeven. Het effect van interne reflecties, die aanwezig zijn in de experimenten, en alternatieve fasefuncties voor de Henyey-Greenstein-functie worden besproken.

Hoofdstuk 5 presenteert een gedetailleerde analyse van experimentele metingen van de positie-afhankelijke energiefluëntie Φ in 3D-monsters met anisotrope verstrooiende en absorberende bolvormige deeltjes. Een dunne capillair gevuld met quantumdots wordt gebruikt als sonde om de positieafhankelijke Φ te detecteren, en de experimentele waarnemingen worden vergeleken met analytische benaderingen en Monte Carlo-simulaties. Een uitgebreide uitleg van de experimentele beperkingen die een absolute meting en een exacte overeenkomst met de modellen voorkomen, wordt gegeven. Met name de P_1 en P_3 benaderingen slagen er niet in om overeen te komen met de waargenomen trends in Φ, terwijl de Monte Carlo-simulaties en de $P_3 + \delta E(4)$ benadering een relatief goede overeenkomst vertonen met de gemeten trends van Φ. Voortzetting van het onderzoek dat in dit hoofdstuk is uitgevoerd, moet beginnen met het verbeteren van de instabiliteiten en beperkingen van de metingen, zoals vermeld in Hoofdstuk 5. Het gebruik van een grotere integrerende bol met een kleiner poortfractie maar een groter poortoppervlak om al het doorgelaten en gereflecteerde licht te vangen, zal de fouten bij de bepaling van de (a, g)-parameters van de monsters verminderen. Bovendien maakt het gebruik van bekende monsters in experimenten de bepaling van de (a, g)-parameters en de fasefunctie voor de modellen mogelijk via Mie-berekeningen, op voorwaarde dat de brekingsindex en de grootte van de deeltjes bekend zijn. Een meer stabiel ontwerp voor de houder van de sonde, dat ervoor zorgt dat de capillair verticaal blijft en het uitgezonden licht van de quantumdots efficiënt koppelt aan de vezel van de detector, zou de schalingswaarde K in vergelijking 5.4 verminderen. Het effect van de sonde binnenin het monster moet verder worden gekarakteriseerd om te bepalen hoe het door de sonde verstrooide licht $\Phi(z)$ binnenin het monster verandert, vooral omdat het monster eindig is en interne reflecties een belangrijke rol spelen. Mogelijke manieren om dit effect te karakteriseren, zijn metingen en simulaties van de hoekafhankelijkheid van de verstrooide intensiteit door de sonde.

Ten slotte rapporteert Hoofdstuk 6 de voorlopige resultaten van positie-afhankelijke quasi-2D-energiedichtheidsmetingen op quasi-2D-monsters van willekeurig gepositioneerde pilaren die geëtst zijn op een siliciumwafer. De energiedichtheid wordt onderzocht door het meten van uit-plane verstrooiing vanaf de bovenkant van de monsters, wanneer de verlichting wordt gedaan door een IR-laser met richting loodrecht op de lange assen van de pilaren. De laser wordt gefocust op het monsteroppervlak met behulp van een cilindrische lens om ervoor te zorgen dat de verlichting alleen op de pilaren en niet op de eindpunten van de pilaren plaatsvindt. Deze eerste resultaten komen overeen met de verwachtingen van dergelijke anisotrope en meervoudig verstrooiende monsters, maar de experimenten moeten worden verbeterd om betere conclusies te kunnen trekken. Een

gespecialiseerde monsterhouder moet worden ontworpen om de monsters nauw-keurig te positioneren op de gewenste focusplek en om de positioneringsfouten besproken in Hoofdstuk 6 te voorkomen. Bovendien zou een objectief met een grotere NA meer van het verstrooide licht kunnen verzamelen. Een uitgebreid onderzoek is nodig om de gebreken van de monsters te verminderen. Met name de vorming van ondiepe tunnels in het midden van de pilaren moet worden voor-komen. Deze tunnels worden waarschijnlijk veroorzaakt door de uitlijning van het etsmasker. Bovendien moeten grotere monsters worden gefabriceerd die meer metingen van niet-overlappende panelen mogelijk maken. Nadat de experimenten zijn verbeterd, moeten de nieuwe resultaten worden vergeleken met theoretische verwachtingen, vergelijkbaar met Hoofdstuk 5, maar voor monsters met cilindri-sche deeltjes. Reflectiemetingen van het vooroppervlak van de monsters kunnen helpen om de monsters beter te karakteriseren en kunnen worden gebruikt om de experimentele resultaten verder te vergelijken met theoretische modellen. Der-gelijke monsters zijn ook uiterst interessant voor metingen van terugverstrooiing en lokaliseringsstudies.

In dit proefschrift hebben we het lichttransport bestudeerd binnenin monsters met anisotrope verstrooiing en absorptie, specifiek de positie-afhankelijke ener-giedichtheid in dergelijke monsters. Onze resultaten bieden een beter begrip van deze monsters, waar gangbare benaderingen falen om het lichttransport te be-schrijven, en geven een richtlijn voor de toepasbaarheid van analytische modellen als alternatief voor Monte Carlo-simulaties.

Acknowledgments

"It will be tough, but you will emerge stronger." were the words I heard four years ago from both Emre Yüce, who informed me about the PhD opportunity at COPS, and from Willem, who accepted me for the position. They couldn't have been more accurate. Indeed, it was tough to step out of my comfort zones; leaving my hometown, country, and family, changing the research topic, and adapting to an entirely different work culture. Looking back, I believe that I have grown both personally and professionally in these last years. I have learned so much! I know that I wouldn't have been able to survive the hardships and complete this thesis without the support of my friends, colleagues, and family. This final chapter is where I offer my sincere gratitude to each person who contributed to this journey.

I would like to start by thanking my supervisor **Willem** and co-supervisor **Ad**. **Willem**, thank you for giving me the opportunity to be a part of COPS, even though I came from a different background at the time. I am grateful for all the lessons I learned from you about science and life in general. I find it inspiring that every time I got stuck, through our discussions (whether we agreed or heavily disagreed!), you managed to point me in a useful direction. Even when you were busy with a million other things, you found time for discussions (although I did have to bribe you with a cup of coffee sometimes :)). You were always eager to have these discussions in the lab instead of the office, which showed your genuine interest and was very motivating for me. I would also like to thank you for all your effort to get us back in the lab in corona times. **Ad**, I am grateful to have had the opportunity to work with a prestigious scientist like you. Your passion for science and your profound knowledge of physics are truly fascinating. I always knew I could count on you to point out mistakes and guide me in the right direction. I find it inspiring that you never give up and constantly pursue your curiosity. Thank you for teaching me how to defend my research professionally, for constantly pushing me to deliver clear presentations and for carefully reviewing all the manuscripts we prepared. Thank you both, **Willem** and **Ad**, for being such supportive mentors.

I would also like to express my gratitude to the members of the graduation committee: **Alwin Kienle**, **Bernard Geurts**, **Johannes de Boer**, **Suhyb Salama** and **Gilles Vissenberg**, for dedicating their valuable time to read and evaluate my thesis.

During the monthly meetings and various scientific events of the NWO-TTW Free-Form Scattering Optics (FFSO) program, I had the opportunity to meet people from both academia and industry. I extend my gratitude to the group of **Wilbert IJzerman** from TU Eindhoven, the group of **Paul Urbach** and **Aurèle Adam** from TU Delft, and all our industry partners ASML, Signify, Lu-

I would like to thank **Chris** and **Marek** once again for taking on the para-nymph duties, and supporting me on the final stages of my PhD, just as they did since the very beginning.

Now, I'd like to express my gratitude to the wonderful individuals I've met in Enschede outside of research, who have provided me with their support over the years. They, perhaps unknowingly, have helped me a lot during many challenging times. **Jacopo**, **Lucia**, and **Danai**, thank you for making my time in Enschede far more enjoyable than I anticipated. It was a pleasure to feel the warm Mediterranean culture in the Netherlands. **Pooya**, **Neda**, **Dora** and **Andrej**, I'm grateful for the enjoyable outings we've shared and for the delicious dishes you prepared. It was fun to find the similarities in our languages and cultures. Sifu **Edgar Zimmerman**, thank you for teaching me martial arts, even finding ways to do it during the pandemic. I thank my teammates from the ultimate fris-bee team **Disc Devils Twente**: **Stephanie**, **Benoit**, **Fred**, **Max**, **Matthias**, **Jennique**, **Pin** and others. I truly enjoyed the fun and competitive practices, competitions and tournaments. It has been a pleasure to be a part of DDT.

I would also like to thank my lifelong friends from back home. While their contributions may not have been directly related to my research, their unwa-vering support has been crucial to me throughout these years. I could write extensive paragraphs for each and every one of you, but that would require an entirely new chapter. To my former team mates, **Samet**, **Güray**, **Sahra**, **Onur**, **Çağlak**, **Fatih**, **Gamze**, **Orçun**, **Zeynep**, **Mert**, **Ata**, and **Azmi**; my friends and colleagues from the Middle East Technical University, **Deniz**, **Hevi**, **His-ham**, **Mona**, **Gamze K.**, and **Işınsu**; my dear friends from BSc. years, **Melis**, **Baran**, and **Ege**; my lifelong friends since highschool, **Ahmet**, **Berk**, **Uygar**, **Elifnaz**, **Yarkın**, **Selçuk**, **Berat**; and my oldest friends from primary school, **İnanç** and **Sade** — I am amazed by the fact that we have maintained our con-nection over the years despite the physical distance. Your enduring friendships have been a consistent source of support over the years, bringing comfort during challenging moments. I'm truly grateful for this and can't thank you enough.

Certainly, none of my achievements would have been possible without the unconditional and unwavering support of my beloved family. To my mother, **Sevinç**, and my father, **Seyfi**, my eternal gratitude for providing me every edu-cational opportunity, and never hesitating to support me whenever I needed in my life. I am grateful to **Selin** for being the remarkable big sister I've always looked up to. Heartfelt appreciation goes to my aunts **Şahibe** and **Zerrin**, uncles **Se-dat** and **Sezai**, and my grandmother **Yeter** for their consistent encouragement and support throughout this journey.

Finally, I want to express my deepest gratitude to the person who has been my greatest supporter over the past nine years. **Sevgi**, it is hard to put into words how much you have strengthened me during this time. I know that this PhD journey would have been much more challenging without your unwavering support. Thank you for always knowing how to lift my spirits, for being someone I can always count on, for consistently inspiring me, and for your constant love. We have achieved so much together, and I'm excited for the next chapter.

Ozan